Localization spectroscopy of a single ion in an optical lattice

Olivier Legrand

PhD Thesis

Danish National Research Foundation
Center for Quantum Optics – Quantop
Department of Physics and Astronomy
The University of Aarhus

July 2015

Localization spectroscopy of a single ion in an optical lattice

Olivier Legrand

PhD Thesis

Danish National Research Foundation
Center for Quantum Optics – Quantop
Department of Physics and Astronomy
The University of Aarhus

July 2015

This Thesis is submitted to the Faculty of Science at Aarhus University, Denmark, in order to fulfill the requirements for obtaining the PhD degree in Physics. The studies have been carried out under the supervision of Prof. Michael Drewsen in the Ion Trap Group at the Department of Physics and Astronomy at Aarhus University from May 2012 to July 2015.

Localization spectroscopy of a single ion in an optical lattice

Olivier Legrand,
Aarhus, July 2015

Résumé på Dansk

Denne afhandling omhandler primært undersøgelser af dynamikken af en enkelt laserkølet $^{40}Ca^{+}$ ion, som bevæger sig i et potentiale sammensat af et overordnet harmonisk potentiale fra en ionfælde og et hurtigt moduleret periodisk potentiale - et såkaldt lysgitter - frembragt af en stående lysbølge. Ud over at forståbevægelsesdynamik i denne situation under varierende potentialeforhold, danner dette arbejde endvidere udgangspunktet for fremtidige studier af en række kvantefysiske mange-legememodeller, for strukturelle manipulationer af større ion Coulomb-krystaller, og for optimering af vekselvirkning mellem lys og stof til brug i forbindelse med kvanteinformatik.

Med udgangspunkt i en lineær rf ionfælde med et harmonisk potentiale strækkende sig over flere millimeter, påvirkes $^{40}Ca^{+}$ ionen langs en af bevægelsesretningerne desuden af en stående lysbølge med en periodicitet på $\sim 433\ nm$ dannet vha. en optisk kavitet, som resonerer ved $\sim 866\ nm$. Selve lysgitret opstår pga. vekselvirkning af dette lys med $D_{3/2} \rightarrow P_{1/2}$ overgangen i $^{40}Ca^{+}$ ionen, som skaber et potentiale hvis dybde er proportionalt med lysintensiteten og hvor minimum af det inducerede potentiale vil være at finde ved intensitetsminima og -maksima afhængig af om lysets frekvens er højere eller lavere end overgangsfrekvensen. En simpel, men grov metode til at lære noget om en ions bevægelse i lysgitret består i at måle hvor ofte ionen absorberer fotoner fra den stående bølge, da dette vil være proportionalt med lysintensiteten og vil derfor ved lokalisering være hhv. lav/høj omkring intensitetsminima eller -maksima.

I mit ph.d.-projekt har jeg arbejdet på at forbedre informationen om iondynamikken ved direkte målinger af fordelingen af energiskiftet af $D_{3/2} \rightarrow P_{1/2}$ overgangen pga. ionens bevægelse i lysgitret. Den benyttede teknik har i sin nuværende implementering allerede vist yderligere tegn på lokalisering indenfor få hundrede nm i det optiske lysgitter. Dette kan tyde på rigere dynamik af ionen i det optiske gitter end først antaget. Mere detaljerede studier af iondynamikken forventes muliggjort af et mere effektivt detektionsskema baseret på såkaldt "shelvin". Udover det eksperimentelle arbejde, som også har inkluderet et komplekst kalibrerings- og analysearbejde, har jeg foretaget adskillige teoretiske simuleringer af den forventelige iondynamik og tilhørende optiske respons af ionen. Endelig har mit ph.d.-projekt også budt på en mere teknisk udfordring med opbygningen af en ny frekvensfordoblet lyskilde til laserkøling af Ca^{+} ioner, og som et nyt værktøj i forbindelse med en ny generation af optiske kavitetseksperimenter i Ionfældegruppen på AU.

Résumé in English

The work reported in this thesis primarily focuses on studies of the dynamics of a single laser-cooled ion, simultaneously confined in the harmonic potential of a linear Paul trap and a rapidly varying periodic potential - a so-called optical lattice - generated from an optical standing-wave. Besides providing a better understanding of the dynamics of an ion subjected to varying trapping conditions, this work establishes a basis for future studies of various quantum many-body physics models, for manipulations of the structure of large ion Coulomb crystals, and for optimization of the interaction between light and matter in connection with quantum information experiments.

In addition to the deep, three-dimensional harmonic potential of the linear Paul trap which confines the ion in regions of several millimeters, one of the directions of the ion motion is constrained by the application of a one-dimensional optical standing wave with a periodicity of $\sim 433\ nm$ generated in an optical cavity resonating at $\sim 866\ nm$. The interaction between the standing wave and the $D_{3/2} \rightarrow P_{1/2}$ transition in $^{40}Ca^{+}$ results in a rapidly-varying potential (an optical lattice), whose depth is proportional to the standing wave intensity, and which pins the ion at a maximum (an antinode) or at a minimum (a node) of intensity depending on the positive or negative frequency difference between the standing wave and the $D_{3/2} \rightarrow P_{1/2}$ transition. A simple but coarse method to obtain information on the ion dynamic inside the lattice is to measure the rate of absorption of lattice photons by the ion, since this rate is proportional to the standing wave field intensity and thus is high or low depending on whether the ion is localized at an antinode or at a node of the standing wave.

During my PhD project, I have been working on a method improving the knowledge on the ion dynamics by directly measuring the frequency change of the $D_{3/2} \rightarrow P_{1/2}$ transition due to the ion dynamics in the standing wave. This method has provided further evidence of the sub-wavelength localization of the ion inside the optical lattice, and points at richer dynamics of the ion inside the optical lattice than initially assumed. Greater accuracy in the measurements enabling in-depth studies of the ion dynamics is expected through the use of an improved "shelving" detection technique. Aside from the experimental work which has also involved a complex calibration and analysis of the detection system, several theoretical simulations of the expected dynamics and associated optical response of the ion were undertaken. Finally, a new laser source based on second harmonic generation was developed in order to perform laser-cooling of Ca^{+} ions, and to serve as a new tool for future cavity quantum electrodynamics experiments in the Ion trap group at Aarhus University.

Publication

1. O. Legrand, P. Neveu, T. Lauprêtre, A. Dantan, M.Drewsen, *"Localization Spectroscopy of a Single Ion in an Optical Lattice"*, Manuscript in preparation.

Contents

Chapter 1

Introduction

Ion traps constitute an ideal tool to probe, control and manipulate single quantum systems. Their invention, in the middle of the twentieth century [1], allowed experiments on atomic systems trapped in small regions of space and isolated from their surroundings - an ideal starting point for high-precision spectroscopy. Due to the impossibility to trap charged particles using static electric fields only, the trapping relies on the use of Lorentz forces, and is realized through a combination of dc electric and magnetic fields in the case of a Penning trap, or dc and rf electric fields in the case of a Paul trap. In these cases, the confining potential thus created has typical dimensions ranging from a few tens of micrometers to a few millimeters, and typical depth of $\sim 10^5$ K - enough to trap particles with temperatures of a few hundreds of degree celsius. The first high-resolution measurement of the atomic hyperfine structure of trapped $^3He^+$ ions was performed in 1969 [2, 3]. Soon after, the confinement of a single electron in a Penning trap was demonstrated [4] and this eventually led to the measurement of the electron g factor [5]. Following the proposals to cool down atoms using radiation pressure [6, 7], observation of a single ion via its fluorescence was realized in 1980 in the group of P. Toschek [8]. The possibility to confine single particles and observe their fluorescence over extended period of time later led to the observation of quantum jumps [9–12]. In general, the ability to trap a single ion at the center of an rf Paul trap where the electric field essentially vanishes, and to cool it down to a state of near complete rest using the sideband cooling technique [13, 14] opened up new possibilities for manipulations of the ions motion at the quantum level [15].

Trapped ions as a tool for quantum information

In parallel to the experiments aiming at a better control over a single ion, the late 1980's were also the time of the first observations of ion Coulomb crystals (ICC) [16, 17], i.e. crystalline structures obtained by Doppler-cooling gaseous ensembles of trapped ions to the limit where their thermal energy is lower than the energy due to the Coulomb repulsion. Small ICC of a few tens of ions in one-dimensional structures constitute a chain of coupled harmonic oscillators, and retain excellent coherence properties of single ions. This combination makes them ideal candidates to perform quantum computation [18]: the ions can be individually addressed with tightly fo-

cused laser beams; by using optical pumping and shelving techniques [15] their states can be prepared and detected with near-unit efficiency, and their internal states can be quantum correlated owing to the existence of common normal modes of vibration. This excellent control over both the internal and external degrees of freedom of ions has led to numerous breakthroughs in the field of quantum information: demonstrations of quantum gates [19, 20], generation of non-classical states [21, 22] quantum teleportation [23], spectroscopy using quantum logic [24], and the implementation of quantum error correction schemes [25, 26]. In 2011, a 14-qubit entanglement in a string of $^{40}Ca^{+}$ ions confined linear Paul trap was reported in R. Blatt's group [27]. However, despite the great advances in the field of quantum computation during the past decades, building a universal quantum computer remains an extremely challenging task essentially because of the difficulty to scale the already existing systems to larger sizes. Nevertheless, well-controlled systems consisting of chains and two-dimensional structures of a few tens of ions already provide an interesting setting for simulating complex fundamental many-body physics models [28]. For example, such structures were recently used to study a very general model known as the Kibble-Zurek model [29, 30] predicting the occurrence of defects in a second order phase transition [31–34], thus opening up the way to investigate the physics of nonequilibrium dynamics from the classical to the quantum regime.

Following ideas implemented with neutral atoms confined in optical lattices to simulate quantum many-body physics, it has also been recognized that combining state-dependent optical forces and Coulomb trapping could significantly broaden the scope of simulations based on trapped ions. In short, the expected benefits comes from the variety of optical structures that can be obtained by combining laser fields of different directions, frequencies and intensities, and that these optical "lattices" can be applied simultaneously to hundreds of ions. By doing so, complex Ising models can be simulated, and quantum many-body physics can be investigated [35–42]. In simulations of the Frenkel-Kontorova model for friction [43]with trapped ions [44–46], the optical field simulate the substrate onto which a chain of ions slides, or is pinned depending on the structural mismatch between the two. This sliding/pinned transition has recently been observed in a three-ion chain [47]. One-dimensional optical lattices could be used at a profit to study the transport of heat in ion chains [46, 48, 49], the generalized Dicke models [50] and the dynamical localization [51], or to stabilize crystalline structure of large Coulomb crystals [52]. In the context of cavity quantum electrodynamics experiments, the use of cavity-generated optical lattices could be used to enhance the light-ion coupling [53–55], to investigate the dynamics of ions in quantum potentials [56–58], or to study nanofriction in dynamically deformable substrate [59]. Purely optical confinement of the ions could allow for experiments without being affected by the micromotion inherent to rf Paul traps, in particular in cold chemistry experiments involving ions and neutrals [60–63].

Localizing ions in an optical lattice

In this thesis we study the dynamics of a $^{40}Ca^{+}$ ion pinned in a one-dimensional optical lattice. This work builds up on demonstrations of localization of one-dimensional, two-dimensional and three-dimensional structures consisting of 1 to 8 ions in an optical lattice performed in the group [55,64]. In a typical experiment, the ion is trapped

in a linear Paul trap and placed within the mode of an optical cavity which axis coincide with that of the trap. After a sequence of Doppler cooling bringing the ion temperature to mK range, an intracavity one dimensional optical lattice is adiabatically ramped up to a depth of a few tens of mK. The optical lattice induces a position-dependent ac Stark shift on the ion's energy levels which can be measured by applying a probe field from the side of the optical cavity. By measuring the spectrum of the pinned ion, we obtain information on its position distribution inside the optical lattice, on the lattice depth and, provided the ion possess a thermal distribution, on its temperature inside the optical lattice. The experiments presented here constitute a proof of principle of methods that could be applied in connection with studies on the heat transport in chains of ions, and on the competition between optical and Coulomb forces with a connection to the aforementioned Frenkel-Kontorova model for friction.

Thesis outline

This thesis is organized in three parts. The first part reviews the main concepts and mathematical tools used throughout the thesis:
The working of a linear Paul trap is described in CHAPTER 2.
A description of the atom-light interaction in terms of the semiclassical optical Bloch equations is given in CHAPTER 3.
In CHAPTER 4 we use some of the results of CHAPTER 3 to review the main aspects of Doppler cooling.
In CHAPTER 5 we derive the equations describing the dynamics of the field confined inside an optical cavity, and introduce the dressed-state model which we use to describe the interaction between the ion and the optical lattice.
The second part is dedicated to the experimental setup: the building of a frequency-doubled system intended to be used as a source for Doppler-cooling of Ca^+ in future experiments is presented in (CHAPTER 7).
The experimental setup is described in (CHAPTER 8).
In CHAPTER 9, an analysis of the working of the detection and imaging system which will be used to analyze the experimental results is provided.
Finally, the last part focuses on the localization experiments:
We start by giving some historical context in CHAPTER 10.
The localization spectroscopy experiment and a presentation of the results are presented in CHAPTER 11.
Finally, in CHAPTER 12 we give a brief outlook and conclude.

Part I

Trapping and cooling of ion in a linear Paul trap

Chapter 2

Trapping ions in a linear Paul trap

2.1 Working principles of a rf linear Paul trap

The principle of ion trapping derive from the constraint imposed by Earnshaw's theorem that a charged particle cannot be held in a stable equilibrium by electrostatic forces alone, and thus relies on the creation of a potential well with combinations of multipolar electromagnetic fields. Examples of ion trapping technologies include a combination of magnetic and quadrupolar electrostatic fields in the case of the Penning trap, and a combination of quadrupolar radiofrequency and static electric fields in the case of the Paul trap. Details on these traps and examples of other trapping technologies can be found in, e.g., [1] and references therein. The experiments per-

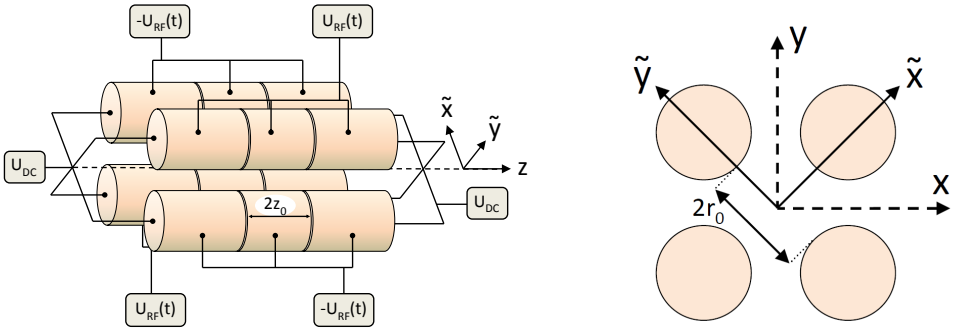

(a) (b)

Figure 2.1: (a) Schematic of the linear Paul trap with the applied voltages U_{DC} and U_{rf}. The length of the center electrode is $2z_0$. The trap axis coincides with the z-axis. (b) End-view of the trap with the definitions of the inter-electrode distance $2r_0$, the $\tilde{x}$ and $\tilde{y}$ axis.

formed in the Ion Trap Group in Aarhus, and more specifically the ones described in this thesis use a variant of the Paul trap generally called the linear Paul trap. Historically, the development of the Paul trap followed the invention of the quadrupole mass filter by W. Paul in the 1950s [65, 66]. However, the development of the linear Paul trap only followed approximately 30 years later and aimed at improving the existing

technologies in relation to high precision spectroscopy experiments [67].
A schematic of the linear Paul trap can be seen on figure 2.1(a). It consists of four rods placed in a quadrupole configuration. Each of the rods is sectioned in three electrodes - two end-caps and a center electrode - such that the trap consists in total of twelve electrodes on which individual voltages can be applied. Applying rapidly-oscillating voltages $U_{RF}(t) = \frac{1}{2}U_{rf}\cos(\Omega_{rf}t)$ on a pair of diagonally opposite rods and simultaneously $-U_{RF}(t)$ on the other pair produces the radial potential:

$$\phi(\tilde{x},\tilde{y},t) = -\frac{1}{2}U_{rf}\cos(\Omega_{rf}t)\frac{\tilde{x}^2-\tilde{y}^2}{r_0^2} \tag{2.1}$$

with r_0 the inter-electrode inscribed radius defined on fig. 2.1(b). Axial confinement is obtained by applying a static voltage U_{DC} on the end-caps, which results in the electrostatic potential along the z-axis and close to the center of the trap:

$$\phi(z) = \eta U_{DC}\frac{z^2}{z_0^2} \tag{2.2}$$

where η is an axial geometry constant defined by the trap geometry [53], $2z_0$ the length of the center electrodes. Laplace equation $\Delta\phi = 0$ implies that the application of static voltages on the end-caps also results in an additional, defocusing radial potential. Therefore the total radial potential is given by:

$$\phi(\tilde{x},\tilde{y},t) = -\frac{1}{2}U_{rf}\cos(\Omega_{rf}t)\frac{\tilde{x}^2-\tilde{y}^2}{r_0^2} - \frac{1}{2}\eta U_{DC}\frac{\tilde{x}^2+\tilde{y}^2}{z_0^2} \tag{2.3}$$

The equations of motion for a charged particle of mass M in such a potential can be found by applying Newton's second law $M\ddot{\mathbf{r}} = -\nabla\phi(\mathbf{r})$. Defining the dimensionless parameters:

$$\tau = \frac{\Omega_{rf}t}{2}, \qquad a = -4\frac{\eta Q U_{DC}}{M z_0^2 \Omega_{rf}^2}, \qquad q = q_x = -q_y = 2\frac{QU_{rf}}{M r_0^2 \Omega_{rf}^2} \tag{2.4}$$

the equations of motions in the radial plane take the following form:

$$\frac{\partial^2 u}{\partial\tau^2} + [a - 2q_u\cos(2\tau)]u = 0, \qquad u = \tilde{x},\tilde{y} \tag{2.5}$$

which are known in the literature as the Mathieu equations (see, e.g. [15, 66]). Depending on the values of a and q, the solutions of the Mathieu equations are either exponentially-diverging, or oscillating functions of time τ. There exists, therefore, regions of the (a,q) plane where bounded motion can take place. These regions are plotted in fig.2.2(a). One can see on eq. 2.4 that trapping a positively charged particle - as is the case in the work presented in this thesis - imposes that a be negative if one wants stable motion along the z-axis. The corresponding stability region is plotted in fig. 2.2(b).

In general the trap is operated such that $|a|, |q| \ll 1$. This allows for the solution of the equation of motion (eq. 2.5) to be approximately written as:

$$u(t) = u_0\left[1 - \frac{q_u}{2}\cos(\Omega_{rf}t)\right]\cos(\omega_r t) \tag{2.6}$$

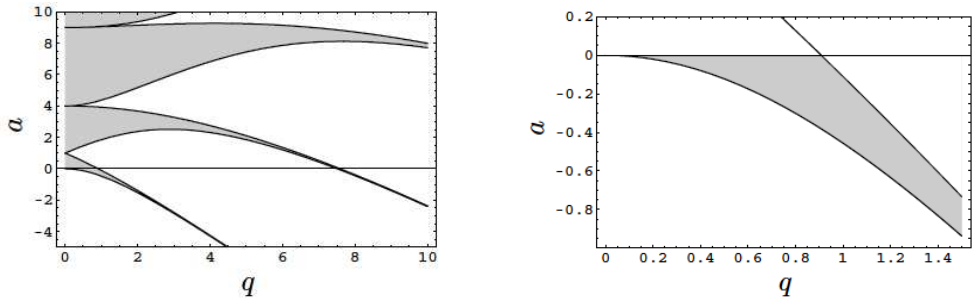

(a) (b)

Figure 2.2: (a) Stability diagram of the Mathieu equation in the (q, a)-space. Regions with stable solutions are marked with grey. (b) Region of stable motion of a positive particle in the linear Paul trap. Both diagrams also apply to negative q-values, i.e. stability regions are mirrored in the a-axis.

by introducing the secular frequency

$$\omega_r = \frac{\sqrt{q^2/2 + a}}{2}\Omega_{rf} \tag{2.7}$$

In this range of parameters, the ion's motion thus possesses two distincts components: a high frequency motion at Ω_{rf} and a low frequency motion at $\omega_r \ll \Omega_{rf}$. The amplitude of the high frequency motion - termed *micromotion* - is given by the q parameter and therefore only acts as a small jitter superimposed on the dominant *secular motion*. Averaging out the fast motion, the ion's motion is then only described by the secular motion which corresponds to the motion in the *pseudo-potential* $\Phi(r, z)$ given by:

$$\Phi_r(r) = \frac{1}{2}M\omega_r^2 r^2 \tag{2.8}$$

Similarly, the axial potential can be rewritten as:

$$\Phi_z(z) = \frac{1}{2}M\omega_z^2 z^2 \tag{2.9}$$

with

$$\omega_z^2 = \frac{2\eta Q U_{DC}}{M z_0^2} \tag{2.10}$$

The final trapping potential for the ions is therefore given by the sum of the radial pseudopotential and the axial potential:

$$\Phi(r, z) = \frac{1}{2}M\omega_r^2 r^2 + \frac{1}{2}M\omega_z^2 z^2 \tag{2.11}$$

It is worth noting that apart from the choices of the voltages and frequency Ω_{rf} applied on the electrodes, the trapping parameters a and q depend solely on the charge to mass ratio Q/M of the trapped particle. This implies that different species can be simultaneously trapped provided the ratios Q/M are not too different. Another

important aspect of this trap is its depth: for a radial secular frequency of $2\pi \times 400$ kHz and an inter-electrode distance of 2.35 mm, the depth of the radial pseudo-potential expressed in Kelvin is $\sim 10^5$ K, and a similar calculation with a secular axial frequency of $\sim 2\pi \times 100$ kHz yields the same order of magnitude for the axial potential. The depth of the trapping potential is thus much deeper than the typical temperature (around 650 K) of the calcium atoms produced in the oven (see section 8.3). Anticipating a little on the following chapters, we also note that these trapping potentials are also many orders of magnitude deeper than typical trapping potentials created with laser fields - a few tens of mK [68]-, but their spatial extent (a few mm in our case) is much larger than that of optical traps - on the order of the wavelength of the trapping light.

Chapter 3

Atom-light interaction

In the experiments presented in this thesis the ion interacts with several light fields, which for the most part are well described classically. The goal of this part is to briefly introduce the framework adapted to the study of such interaction and its main results, which we will use in the next chapters.
The system we consider here is a two-level atom interacting with a classical monochromatic, single mode electromagnetic field. We will start by defining an Hamiltonian for this system, and go on with establishing the equations describing the evolution of the atomic internal degrees of freedom. Finally, steady-state solutions of these equations will be presented.

3.1 Hamiltonian of a two-level atom interacting with a classical electromagnetic field

We consider a system composed of a two-level atom interacting with a classical electromagnetic field. The Hamiltonian of such system can be written:

$$H = H_A + H_{Int} \tag{3.1}$$

The first term, H_A, corresponds to the atomic part and reads:

$$H_A = \hbar\omega_0\hat{\pi}_e \tag{3.2}$$

where $\hat{\pi}_e = |e\rangle\langle e|$ is the excited state population and ω_0 the frequency difference between the ground state $|g\rangle$ and the excited state $|e\rangle$ of the two-level atom. The second term in eq. (3.1), H_{Int}, describes the interaction between a two-level atom and an electromagnetic field and reads, in the dipole approximation:

$$H_{Int} = -\hat{\mathbf{D}} \cdot \mathbf{E}(t) \tag{3.3}$$

where $\mathbf{E}(t)$ is the electric field, and $\hat{\mathbf{D}}$ the atomic dipole. We assume that the field has a frequency ω_L, amplitude $\mathcal{E}_0$ and polarization $\boldsymbol{\epsilon}$:

$$\mathbf{E}(t) = \boldsymbol{\epsilon}\mathcal{E}_0 \cos(\omega_L t) \tag{3.4}$$

The atomic dipole is given by:

$$\hat{\mathbf{D}} = \mathbf{d_{ge}}\hat{\sigma}_{ge} + \mathbf{d_{eg}}\hat{\sigma}_{eg} \tag{3.5}$$

where $\mathbf{d_{ge}} = \mathbf{d_{eg}} \equiv \mathbf{d}$ are the dipole matrix elements for the transition and $\hat{\sigma}_{ij} = |i\rangle\langle j|$ with $i, j = \{g, e\}$ are the lowering and raising atomic operators, which we will refer to as the *coherences* in the following. The Hamiltonian H_{Int} can finally be rewritten:

$$H_{Int} = \hbar g(\hat{\sigma}_{ge} + \hat{\sigma}_{eg})\cos(\omega_L t) \tag{3.6}$$

with

$$\hbar g = -\langle i|\hat{\mathbf{D}} \cdot \boldsymbol{\epsilon}|j\rangle \mathcal{E}_0, \qquad i, j = \{e, g\} \tag{3.7}$$

3.2 The optical Bloch equations (OBE)

As we want to calculate the evolution of the atomic variables in the presence of the field, we introduce the density matrix $\hat{\rho}^A$ and note its elements, in the $\{|e\rangle, |g\rangle\}$ basis:

$$\hat{\rho}^A = \begin{pmatrix} \hat{\rho}^A_{ee} & \hat{\rho}^A_{eg} \\ \\ \hat{\rho}^A_{ge} & \hat{\rho}^A_{gg} \end{pmatrix} \tag{3.8}$$

The time-evolution of $\hat{\rho}^A$ is given by the Heisenberg equation $\frac{d}{dt}\rho^A(t) = \frac{1}{i\hbar}\left[H, \rho^A(t)\right]$. Note that the off-diagonal elements of the density matrix coincide with the mean values of the coherences $\hat{\sigma}_{ge}$, $\hat{\sigma}_{eg}$ introduced above, and similarly $\hat{\rho}^A_{ee}$ is equal to the mean value of the population of the excited state. For an arbitrary operator $\hat{o}$ we note the mean value $o = \langle\hat{o}\rangle$ and define π_g such that $\pi_g = \langle\hat{\pi}_g\rangle = \rho^A_{gg}$. Projecting the Heisenberg equation for $\hat{\rho}^A$ in the $\{|e\rangle, |g\rangle\}$ basis, adding terms describing the effect of a spontaneous decay rate Γ from the excited to the ground state, and the decoherence rate of the atomic dipole $\Gamma/2$, we get:

$$\dot{\pi}_e = ig\cos(\omega_L t)(\sigma_{eg} - \sigma_{ge}) - \Gamma\pi_e \tag{3.9a}$$

$$\dot{\pi}_g = -ig\cos(\omega_L t)(\sigma_{eg} - \sigma_{ge}) + \Gamma\pi_e \tag{3.9b}$$

$$\dot{\sigma}_{ge} = i\omega_0\sigma_{ge} - ig\cos(\omega_L t)(\pi_e - \pi_g) - \frac{\Gamma}{2}\sigma_{ge} \tag{3.9c}$$

$$\dot{\sigma}_{eg} = i\omega_0\sigma_{eg} + ig\cos(\omega_L t)(\pi_e - \pi_g) - \frac{\Gamma}{2}\sigma_{eg} \tag{3.9d}$$

The set of equations [3.9a - 3.9d] are called the optical Bloch equations (OBE). It can be shown [69] that, making the RWA in the above system and subsequently redefining the density matrix elements as $\sigma_{eg} \to \sigma_{eg}e^{i\omega_L t}$ and $\sigma_{ge} \to \sigma_{ge}e^{-i\omega_L t}$ while leaving unchanged the populations suppress all dependence on time in the above set of equations. Making these substitutions amounts to a change of reference frame, from the laboratory frame of reference to the one "rotating" with the laser field at the frequency ω_L. We can therefore rewrite the OBE as:

$$\dot{\pi}_e = i\frac{g}{2}(\sigma_{eg} - \sigma_{ge}) - \Gamma\pi_e \tag{3.10a}$$

$$\dot{\pi}_g = -i\frac{g}{2}(\sigma_{eg} - \sigma_{ge}) + \Gamma\pi_e \tag{3.10b}$$

$$\dot{\sigma}_{ge} = -i\Delta_L\sigma_{ge} - i\frac{g}{2}(\pi_e - \pi_g) - \frac{\Gamma}{2}\sigma_{ge} \tag{3.10c}$$

$$\dot{\sigma}_{eg} = i\Delta_L\sigma_{ge} + i\frac{g}{2}(\pi_e - \pi_g) - \frac{\Gamma}{2}\sigma_{ge} \tag{3.10d}$$

Steady state values of the populations and coherences can be obtained by setting the left-hand side of eqs. (3.10) to 0. By doing so, we get for the coherence σ_{ge}:

$$\sigma_{ge} = -\frac{ig/2}{\frac{\Gamma}{2} + i\Delta_L}(\pi_e - \pi_g) \tag{3.11}$$

and likewise, for σ_{eg}:

$$\sigma_{eg} = \frac{ig/2}{\frac{\Gamma}{2} - i\Delta_L}(\pi_e - \pi_g) \tag{3.12}$$

Using these expressions, we get for the steady-state population in the excited state:

$$\pi_e = \frac{1}{2}\frac{g^2/2}{\Delta_L^2 + \frac{\Gamma^2}{4} + \frac{g^2}{2}} \tag{3.13}$$

$$= \frac{1}{2}\frac{s}{1+s} \tag{3.14}$$

where in the last line we used the saturation parameter defined as:

$$s = \frac{g^2/2}{\Delta_L^2 + \frac{\Gamma^2}{4}} \tag{3.15}$$

We will used these expressions in order to describe the Doppler cooling of ions in the next chapter, and in the last chapter of this thesis, when we will describe the interaction of $^{40}Ca^{+}$ with a near-resonant probe field.

Chapter 4

Laser cooling of a trapped $^{40}Ca^{+}$ ion

4.1 Doppler cooling

As mentioned in chapter 2, the typical temperature of the ions emitted by effusive oven is 650 K, which corresponds to a speed of little less than 400 m/s. In the context of experiments aiming at the measurements and the manipulation of atomic parameters with high precision, the Doppler shifts induced by such speeds are too large, and have to be eliminated. An efficient way to reduce the speed of the atoms is provided with laser cooling, a widely used technique and the detailed treatment of which can be found in, e.g., [70–72]. In this section we will therefore only briefly discuss the basic idea of laser cooling and focus on the aspects relevant for the cooling of $^{40}Ca^{+}$ ions.

Laser cooling depends upon dissipative forces that are velocity-dependent. Its principle relies on the Doppler effect, i.e. the fact that an atom moving along the x-axis with velocity $\mathbf{v} = v\hat{\mathbf{x}}$ in a laser wave of frequency ω_L close to anatomic frequency and wave-vector $\mathbf{k_L}$ "sees" the laser frequency shifted by the Doppler shift $-\mathbf{k_L} \cdot \mathbf{v}$. In the situation of a field counter propagating ($\mathbf{k_L} = -k_L\hat{\mathbf{x}}$), the Doppler effect results in a positive frequency shift $k_L v$, whereas the shift is negative in the case of a field co-propagating. For laser beams slightly detuned to the red of the atomic resonance this leads to a higher absorption probability from the counter propagating beam. The subsequent re-emission of a photon of frequency ω_0 results, in the laboratory frame of reference, in a decrease of the kinetic energy of the atom by an amount $-\hbar k_L v$: the atom is therefore *cooled down* (though only along the direction of absorption) in the process.
In order to gain further insight in the cooling process, we analyze the force exerted by two counter propagating laser fields on a two-level atom moving at velocity v as depicted in fig. 4.1. The force exerted by a laser beam on an atom can be expressed

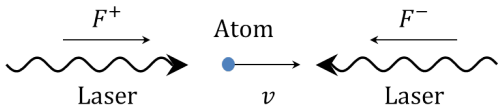

Figure 4.1: Basic principle of Doppler laser cooling.

in terms of the momentum exchange between the light and the atom per photon multiplied by the number of absorbed photons per unit time:

$$\mathbf{F} = \hbar\mathbf{k} \times \left\langle \frac{dN}{dt} \right\rangle_{st} \tag{4.1}$$

where $\left\langle \frac{dN}{dt} \right\rangle_{st}$ is the number of absorbed photons per unit time, in steady state. This number can be re-expressed in terms of steady state population and decay rate of the excited state:

$$\left\langle \frac{dN}{dt} \right\rangle_{st} = \Gamma \pi_e^{st} \tag{4.2}$$

Plugging (4.2) into (4.1) and using eq. (3.14) gives:

$$\mathbf{F} = \hbar\mathbf{k}\frac{\Gamma}{2}\frac{g^2/2}{(\Delta_L - \mathbf{k}\cdot\mathbf{v})^2 + \frac{\Gamma^2}{4} + \frac{g^2}{2}} \tag{4.3}$$

with $\Delta_L = \omega_0 - \omega_L$. In standing-wave field, the total force F^{tot} is the sum of two contributions, from the co- and counter-propagating fields:

$$F^{\pm} = \pm\hbar k\frac{\Gamma}{2}\frac{g^2/2}{(\Delta_L \pm kv)^2 + \frac{\Gamma^2}{4} + \frac{g^2}{2}} \tag{4.4}$$

Expanding the expression for the total force $F^{tot} = F^{+} + F^{-}$ around $v = 0$ to 1^{st} order, the force can be expressed through a friction coefficient β as $F^{tot} = -\beta v$, where

$$\beta = \hbar k^2 \frac{\Gamma\Delta_L}{\Delta_L^2 + \frac{\Gamma^2}{4}} \frac{2s}{(1+s)^2} \tag{4.5}$$

Fig. 4.2(a) shows a plot of this friction coefficient as a function of the detuning. For the force to work as a friction force, β must be positive, which is seen to happen

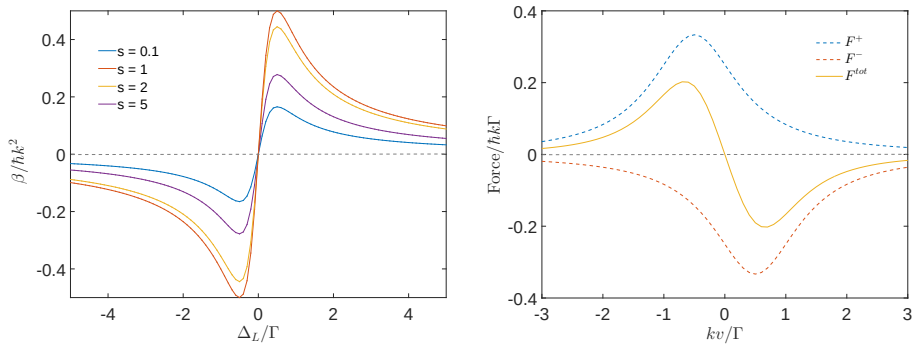

Figure 4.2: (a) Friction coefficient in units of $\hbar k^2$ versus laser detuning Δ_L in units of Γ, for various values of the saturation parameter. (b) Velocity dependence of the laser cooling force on an atom for two counter-propagating lasers (solid line), when the detuning is $\Delta_L = -\Gamma/2$ and the saturation parameter is $s = 1$. Dashed lines represent the forces of individual beams.

for $\Delta_L > 0$. Likewise, β is maximized for a saturation parameter $s = 1$, or in other words for $g = \Gamma$. On fig 4.2(b) we have plotted the total force along with the force resulting from the co- and counter propagating beams, for these values of β and s.

Doppler temperature

So far we have neglected the effect of the spontaneous emission of photons by the atom during the process. Indeed, each emission of a photon imparts a slight change in momentum of the atom. However, because the re-emission of photon is directionally symmetric with respect to the atom, the change in momentum averages out over many scattering events $\langle p \rangle = 0$, and the cooling process does result in a decrease of the atom momentum along the direction of absorption. Nevertheless, the emission of photons by spontaneous decay gives rise to a random walk in momentum space, because $\langle p^2 \rangle \neq 0$. The associated heating rate is independent of the kinetic energy [73], contrary to the cooling rate which can be expressed as $\mathbf{F} \cdot \mathbf{v} \propto v^2$. Therefore, the minimum temperature - termed the Doppler temperature - which can be attained with Doppler cooling is finite, and can be shown to be equal to $T_{lim} = \frac{\hbar\Gamma}{2k_B}$ in the simple free two-level atom scenario considered here [73].

4.2 Doppler cooling of a $^{40}Ca^{+}$ ion

The model derived above provides a satisfying picture of Doppler cooling, but is rather simplistic in that it assumes a free two-level atom. In realistic situations, more levels generally have to be taken into account. We consider in this section the case of the $^{40}Ca^{+}$ ion whose reduced energy level diagram is shown on fig. 4.3. Doppler cooling is performed on the $4s^2S_{1/2} \leftrightarrow 4p^2P_{1/2}$ transition, with a laser slightly red-detuned from the resonant wavelength $\lambda \sim 397$ nm. From the excited state $4p^2P_{1/2}$ the ion can decay to $3d^2D_{3/2}$ with a branching ratio of $\sim 1:12$. Since the lifetime in this metastable state is on the order of the second, the ion needs to be actively pumped back into $4p^2P_{1/2}$ by an additional repumping laser, resonant with the $3d^2D_{3/2} \leftrightarrow 4p^2P_{1/2}$ transition at 866 nm in order to be effectively cooled. The branching ratio implies that the cooling effect is dominated by the scattering of 397 nm photons and from the partial decay rate $\Gamma = 2\pi \times 20.7$ MHz and considering the above, this amounts to a theoretical Doppler temperature of $T_D \approx 0.54$ mK. The total decay rate $\Gamma_{P_{1/2}}$ from the $4p^2P_{1/2}$ state is equal to $2\pi \times 22.4$ MHz, which is much higher than the secular frequencies in Paul trap (a few hundred kHz), and therefore the ion can be considered as "free" during the cooling cycle. More specifically, it can be shown that the effect of the ion's motion in the trap is to add sidebands to the absorption spectrum at the secular frequencies. Since the natural linewidth of the transition is much broader than these secular frequencies, these are not resolved.
In principle, 3 pairs of laser beam need to be used to perform Doppler-cooling along all directions, but in the specific case of a bound ion, only one is needed provided its k-vector has components along the axial and radial components of the trap, and that the secular frequencies $(\omega_x, \omega_y, \omega_z)$ are non-degenerate [77, 78]. However, in the experiments presented in this thesis we use two counter propagating beams aligned with the trap axis, and a third beam directed perpendicularly to it, for practical reasons we detail in the next section. Finally, a bias magnetic of a few Gauss perpendicular

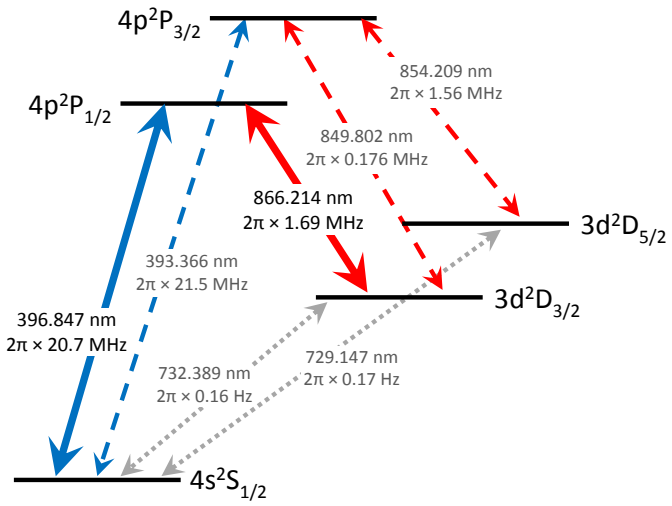

Figure 4.3: Energy level diagram of $^{40}Ca^{+}$, with transition wavelengths in air and transition decay rate Γ taken from [74–76]. The solid lines correspond to the relevant transitions for Doppler cooling in this thesis, i.e. the $4s^2S_{1/2} \leftrightarrow 4p^2P_{1/2}$ Doppler cooling transition (blue) and the $3d^2D_{3/2} \leftrightarrow 4p^2P_{1/2}$ repumping transition (red). Picture taken from [64]

to the polarization of the 866 nm field driving the $3D_{3/2} \leftrightarrow P_{1/2}$ is applied to ensure that all levels are addressed by the repumper.

4.3 Ion Coulomb crystals

So far we have described the trapping and cooling principle in the case of a single ion, but the same principles apply when many particles are being trapped. However, when several ions are confined together they are subjected to the Coulomb repulsion they exert on each other in addition to the trapping potential which tends to attract them toward the center of the trap. When cooled down below a critical temperature - typically 10 mK in our case - corresponding to a regime where the thermal kinetic energy is much lower than the Coulomb energy, the ensemble of ions undergoes a phase transition to a long-range ordered state termed Ion Coulomb crystals.
The simplest type of ion Coulomb crystal is a linear string of ions along the axis of the trap. This configuration arises when the axial confinement is much weaker than the radial confinement. Strings of two and eight ion are shown on fig. 4.4. On the picture showing the eight-ion string, it can be seen that the ion spacing is larger on the sides than in the middle - the last ion feels the repulsion from the other ones. Generally, as the number of ions increases, the separation between adjacent ions at the center of the trap reduces, as can be observed by comparing the two- and eight-ion strings. Raising the axial confinement, or lowering the radial confinement induces a transition to a two-dimensional zig-zag structure. Loading a larger number of ions result in a three-dimensional spheroidal arrangement, the exact form of which depends on the ratio of the axial to radial trapping frequencies.
In a linear rf Paul trap, it is desirable to place the ions along the central axis of trap.

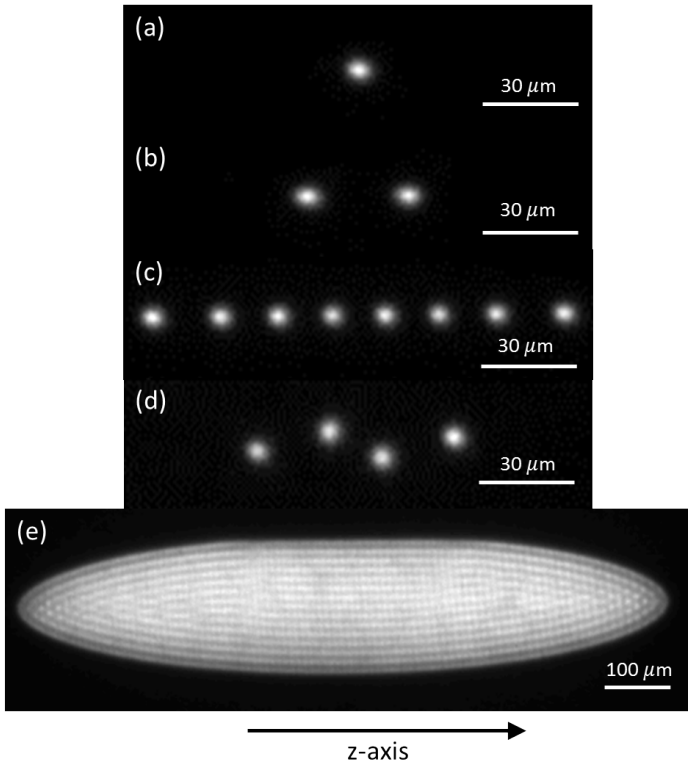

Figure 4.4: Projection images of (a) one, (b) two, (c) eight ions in a string, (d) four ions in a two-dimensional zig-zag structure, and (e) a three-dimensional Coulomb crystal consisting of approximately 6400 ions. The axial and radial trap frequencies are, respectively: 71 kHz and 388 kHz in (a) and (b), 71 kHz and 350 kHz in (c), 87 kHz and 184 kHz in (d). (e) taken from [54].

As a matter of fact, the micromotion amplitude for an ion placed on the axis can be deduced from eq. (2.6) and is given by:

$$A_{micro} = \frac{1}{2} u_0 q \tag{4.6}$$

u_0 being the amplitude of the secular motion. This micromotion is inherent of a linear Paul trap and a consequence of the secular motion carrying the ion back and forth through the nodal line of the rf-field, and is schematically represented on fig. 4.5. It can be minimized by Doppler-cooling the ion which reduces the amplitude of the secular motion. For an ion whose equilibrium position is not located on the nodal line, there is an excess micromotion of the same form but with u_0 replaced with the mean distance to the trap axis [79]. In the case of a single ion, placing the ion on the trap axis is one way to reduce the micromotion, however in the case of a two- or three-dimensional structures there will always be ions placed off-axis.

Laser cooling of large ensembles of trapped ions thus requires some specific considerations. In the case of a string of ions, the Coulomb interaction couples their axial

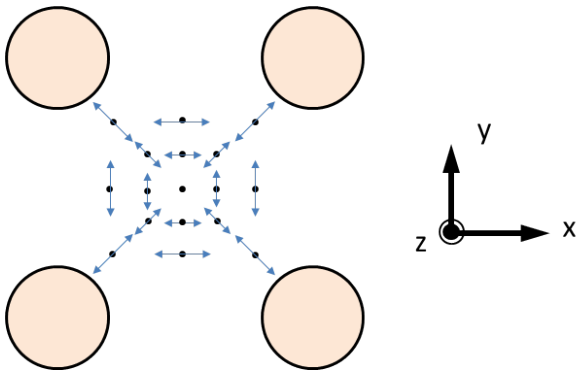

Figure 4.5: Schematic of the micromotion at different locations in the trap. Arrows indicate the direction and amplitude of the micromotion. The dimensions of the electrodes and arrows are not to scale.

vibrational modes, but the radial and axial motion remain uncoupled and Doppler cooling has to be performed along both the axial and radial directions. In the case of three-dimensional structures (corresponding to a less tight radial confinement, as evoked above), the axial and radial motions are coupled and applying Doppler cooling light along the axial direction is sufficient to achieve good three-dimensional cooling. Moreover, for the ions positioned off the trap axis and experiencing excess micromotion, applying a cooling beam along the transverse direction will tend to drive the micromotion and can have a detrimental effect.

Chapter 5

Atom in an optical potential

In chapter 4 we saw that the mechanical effects of the atom-light field can be used to drastically slow down an atomic beam. As we will see in this chapter, the atom-light interaction can also, under certain conditions, lead to non-dissipative forces which can be used to confine the ion in zones of either high or vanishing field intensities. The creation of such *optical potential* necessitates a standing-wave field, which is realized here by confining the field inside an optical cavity. Therefore we will start by introducing the concept of the optical cavity, and try to put emphasis on the benefits one can get by using such a tool. We will, in a second step, derive relevant quantities describing the interaction of an atom with a standing-wave field.

5.1 Optical cavities

5.1.1 Cavity modes

In its simplest design, a cavity consists of two reflecting mirrors M_1 and M_2, separated by a distance L. We consider a monochromatic electromagnetic field traveling along the axis of the cavity. The multiple reflections of the field on the mirrors lead to a situation where the field interfere with itself, and can therefore exist only if the resulting interferences are constructive. This is realized if the phase shift imparted on the field after a round-trip in the cavity is a integer multiple of 2π. This condition is equivalent to impose that the frequency of the light field is an integer multiple of $\frac{c}{2L}$ with c the speed of light in vacuum:

$$\nu_q = q\frac{c}{2L} = \frac{q}{\tau}, \text{qinteger} \tag{5.1}$$

where $\tau = \frac{c}{2L}$ is the round-trip time. The frequencies ν_q are termed the *longitudinal cavity modes*. A field whose frequency ω_L is equal to one of the longitudinal cavity modes is said to be *resonant* with the cavity.
In practice, a cavity made of two plane mirrors is unstable, i.e. a field not propagating perfectly along the axis escapes the cavity after a few round trips. For this reason, cavities used in laboratories are generally made of combinations of spherical and plane mirrors, or spherical mirrors only. In the work presented in this thesis, two types of cavities are used: a linear Fabry-Perot cavity, made of two spherical mirrors facing

each other and which is depicted fig. 5.1. This cavity was used in the past to perform CQED experiments [53, 64, 80], and in our case its main purpose is to generate the optical potential mentioned in the introduction, since the multiple retro-reflections of the field on the mirrors results in the establishment of a standing-wave. The other type of cavity is the ring "bow-tie" Fabry-Perot cavity, made of two plane and two spherical mirrors and is sketched on fig. 5.2. This cavity is used for performing second harmonic generation of light (see chapter 7).

Our goal in the next section is to derive the equations governing the dynamics of an electromagnetic field in an optical cavity close to a resonance, in the case of a cavity whose longitudinal modes are well-separated. As it turns out, these equations are similar for the two types of cavities considered here. Therefore, we will derive them in the case of the linear cavity and adapt them when needed to take into account the additional mirrors in the case of the bow-tie cavity. We will then refer, in the following, to the schematic shown fig.5.1

5.2 Dynamics of the cavity field close to a resonance

The reflection and transmission coefficients for the fields amplitudes are denoted r_1, t_1 and r_2, t_2 for the first and second mirror, respectively. The losses due to absorption and scattering in reflection on either of the mirrors are accounted for by the coefficient α. The incident field is denoted E_{in}, the field inside the cavity E_{cav}, the field transmitted after the cavity E_{trans}, the cavity mode frequency ω_c, the frequency of the incident field ω_L - we assume here the field to be monochromatic - and the round trip time in the cavity $\tau = \frac{2L}{c}$. The amplitude of the intracavity field after one reflection on mirror M_2 reads:

$$E'_{cav}(t) = \alpha r_2 E_{cav}(t-\tau)e^{i\pi}e^{i\phi} \tag{5.2}$$

The phase shift $\phi = (\omega_c - \omega_L)\tau = \Delta_c \tau$ is due to the dephasing of the field with respect to the incident field during the round trip inside the cavity. The additional π phase shift comes from the reflection on any of the dielectric mirrors. For a given input field

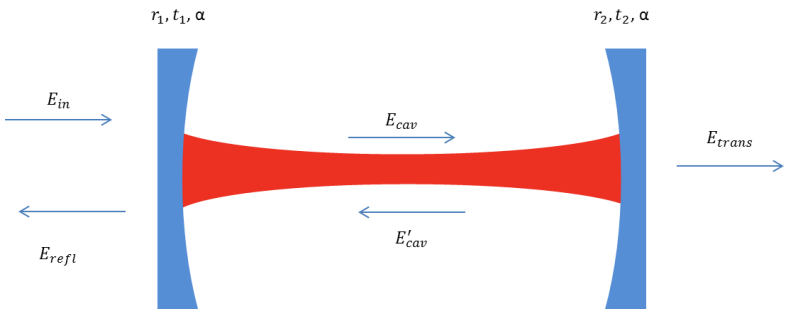

Figure 5.1: Schematic of a Fabry-Perot cavity, with the incident, intracavity and transmitted fields.

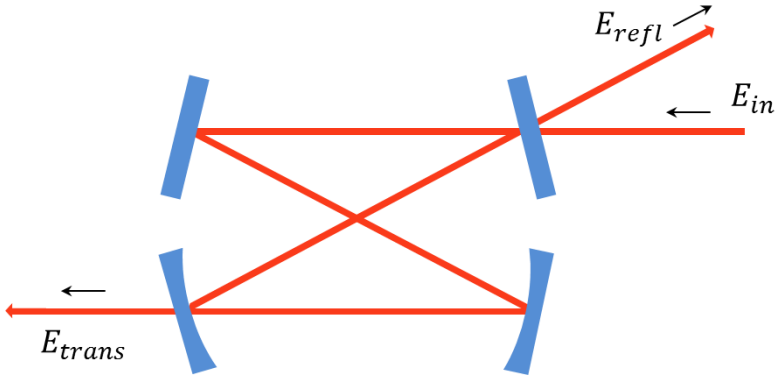

Figure 5.2: Schematic of the bow-tie cavity with the incident, transmitted and reflected fields. In this setup the optical field is never retro-reflected, as opposed to the situation of the linear cavity. As a consequence, the field inside the bow-tie cavity is a running-wave, a property which will be very important for performing second harmonic generation.

E_{in}, the intracavity field at instant t after M_1 must also satisfy:

$$E_{cav}(t) = t_1 E_{in}(t) + \alpha r_1 E'_{cav}(t) e^{i\pi} \tag{5.3}$$

By combining (5.3) and (5.2), we finally get:

$$E_{cav}(t) = \alpha^2 r_1 r_2 E_{cav}(t-\tau) e^{i\phi} + t_1 E_{in}(t) \tag{5.4}$$

In order to find an equation relating the fields inside the cavity at times $t-\tau$ and t, we subtract $E_{cav}(t-\tau)$ to $E_{cav}(t)$ in (5.4), and divide the result by τ:

$$\frac{E_{cav}(t) - E_{cav}(t-\tau)}{\tau} = \frac{(\alpha^2 r_1 r_2 - 1)}{\tau} E_{cav}(t-\tau) e^{i\phi} + \frac{t_1}{\tau} E_{in}(t) \tag{5.5}$$

We can rewrite the above equation in terms of the reflection, transmission and loss coefficients in intensity. Denoting R_i, T_i $(i = 1, 2)$, and $\mathcal{L}$ these coefficients we have $r_i = \sqrt{R_i}$, $t_i = \sqrt{T_i}$ and $\alpha = \sqrt{(1 - \mathcal{L}/2)}$. For each of the mirrors, these coefficients must naturally satisfy $R_i + T_i + \mathcal{L}/2 = 1$. Using the assumption that $T_1, T_2, \mathcal{L}$ and $\phi \ll 1$ and retaining only first order terms in the expansion, we get:

$$\frac{E_{cav}(t) - E_{cav}(t-\tau)}{\tau} = \frac{(1-\mathcal{L}/2)(1-T_1/2)(1-T_2/2)(1+i\phi)}{\tau} E_{cav}(t-\tau) + \frac{\sqrt{T_1}}{\tau} E_{in}(t) \tag{5.6}$$

If the losses due to absorption and scattering and due to the finite mirror transmission per round trip are small, it is convenient to transmission and loss rates defined as:

$$r_i = 1 - \kappa_i \tau, \qquad i = 1, 2 \tag{5.7}$$

and similarly, for the loss coefficient:

$$\alpha = 1 - \kappa_{\mathcal{L}} \tau, \tag{5.8}$$

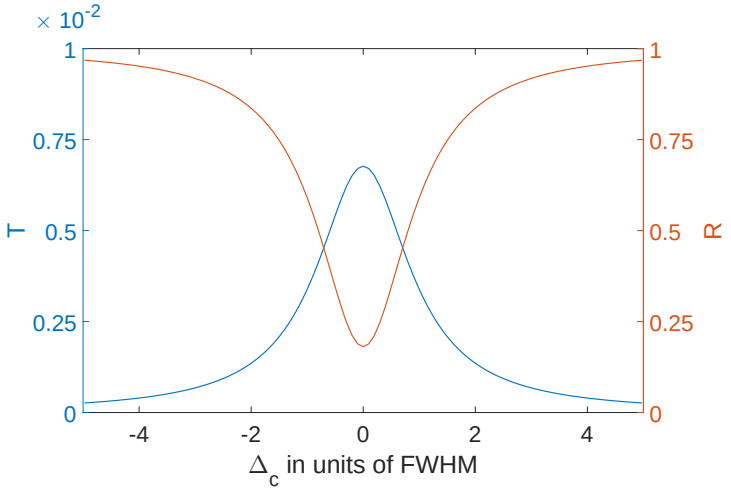

Figure 5.3: transmission (blue) and reflection (red) around one resonance for a cavity with similar parameters as used in our experiment versus the detuning in units of the FWHM. The mirror transmission coefficients are $T_1 = 1500$ ppm, $T_2 = 5ppm$ and the losses are $\mathcal{L}$=600 ppm

The decay rates of the cavity through the mirrors are therefore given by :

$$\kappa_i = \frac{1 - r_i}{\tau} = \frac{1 - \sqrt{1 - T_i}}{\tau} \simeq \frac{T_i}{2\tau}, i = 1, 2 \tag{5.9}$$

And similarly, for the decay rate associated to the losses :

$$\kappa_{\mathcal{L}} \simeq \frac{\mathcal{L}}{2\tau} \tag{5.10}$$

Assuming the cavity decay rates are small compared to $\frac{1}{\tau}$ - which, according to the definitions (5.9) and (5.10) is valid since $T_1, T_2, \mathcal{L} \ll 1$ - we can assume that the round trip time is short compared to the dynamics of the field, and take the limit $\tau \to 0$:

$$\dot{E}_{cav}(t) = \sqrt{\frac{2\kappa_1}{\tau}} E_{in}(t) - (\kappa_{\mathcal{L}} + \kappa_1 + \kappa_2 + i\Delta_c) E_{cav}(t) \tag{5.11}$$

The steady state of the intracavity field amplitude is readily obtained by setting the time derivative in (5.11) to 0 and rearranging the terms in (5.11):

$$E_{cav} = \frac{\sqrt{\frac{2\kappa_1}{\tau}}}{\kappa_{\mathcal{L}} + \kappa_1 + \kappa_2 + i\Delta_c} E_{in} \tag{5.12}$$

The steady state transmitted field amplitude is then :

$$E_{trans} = t_2 E_{cav}(t) = t_2 \frac{\sqrt{\frac{2\kappa_1}{\tau}}}{\kappa_{\mathcal{L}} + \kappa_1 + \kappa_2 + i\Delta_c} E_{in} \tag{5.13}$$

The steady state transmission from the cavity can now be deduced from the above equation, and it reads :

$$T = \left| \frac{E_{trans}}{E_{in}} \right|^2 = \frac{4\kappa_1\kappa_2}{(\kappa_{\mathcal{L}} + \kappa_1 + \kappa_2)^2 + \Delta_c^2} \tag{5.14}$$

Likewise, the reflection from the cavity can be found by writing:

$$E_{refl} = t_1 E'_{cav} + \alpha r_1 E_{in} \tag{5.15}$$

from which the reflection coefficient in steady state can be readily deduced:

$$R = \left| \frac{E_{refl}}{E_{in}} \right|^2 = \frac{(\kappa_{\mathcal{L}} - \kappa_1 + \kappa_2)^2 + \Delta_c^2}{(\kappa_{\mathcal{L}} + \kappa_1 + \kappa_2)^2 + \Delta_c^2} \tag{5.16}$$

The transmission and reflection coefficients are plotted Fig. 5.3. They are Lorentzian functions of the detuning, which Full Width at Half Maximum (FWHM) can be found to be :

$$\delta\omega = 2(\kappa_{\mathcal{L}} + \kappa_1 + \kappa_2) \tag{5.17}$$

The enhancement factor can be read directly from (5.12), as the ratio of the intracavity field over the incident field :

$$\left| \frac{E_{cav}}{E_{in}} \right|^2 = \frac{\frac{2\kappa_1}{\tau}}{|\kappa_{\mathcal{L}} + \kappa_1 + \kappa_2 + i\Delta_c|^2} = \frac{4T_1}{(\mathcal{L} + T_1 + T_2)^2 + \Delta_c^2} \tag{5.18}$$

The finesse of the cavity is defined as:

$$F = \frac{\text{FSR}}{\text{FWHM}} = \frac{2\pi}{T_1 + T_2 + \mathcal{L}} \tag{5.19}$$

where FSR stands for Free Spectral Range, and corresponds to the inverse of the round trip time $\frac{1}{\tau}$. The finesse can be seen as the ratio of the stored energy over the losses during one round trip. While the free spectral range only depends on the distance between the two mirrors, the FWHM depends on the decay rates of the field through the mirrors, and on the losses. Measuring the transmission of the different mirrors is relatively straightforward, but estimating the losses directly by looking at the discrepancy between the measured transmission and reflection for each mirror can be more tricky, especially when they are small - we expect them to be less than or on the order of a percent. Fortunately, the reflectivity spectrum allow for an indirect measurement of the losses. Defining β as the ratio of the reflection from the cavity on and off resonance, we have:

$$\beta = \frac{R(\Delta_c = 0)}{R(\Delta_c \to \infty)} = \frac{(\kappa_{\mathcal{L}} - \kappa_1 + \kappa_2)^2}{(\kappa_{\mathcal{L}} + \kappa_1 + \kappa_2)^2} = \frac{(\mathcal{L} - T_1 + T_2)^2}{(\mathcal{L} + T_1 + T_2)^2} \tag{5.20}$$

We can invert the above equality to find:

$$\mathcal{L} = \frac{1 \pm \sqrt{\beta}}{1 \mp \sqrt{\beta}} T_1 - T_2 \tag{5.21}$$

where the upper sign is used if the sum of the losses and transmission through the output coupler exceed the transmission through the input coupler, i.e. if $\mathcal{L}+T_2 > T_1$, and the lower sign otherwise. As mentioned in the beginning of this section, the equations derived above also apply for a bow-tie cavity, by making the following substitutions: $\kappa_2 \to \kappa_2 + \kappa_3 + \kappa_4$, and by defining α such that $\alpha = \sqrt{1 - \mathcal{L}/4}$. The intracavity field is nonetheless different than that of the linear Fabry Perot cavity, in the sense that the field in a bow-tie cavity is a running-wave while it is a standing -wave in a linear cavity. Therefore, eq. (5.18) gives the appropriate total intracavity field intensity in a bow-tie cavity, but in the case of a linear cavity this expression needs to be replaced by $|E_{cav} + E'_{cav}|^2 = 4|E_{cav}|^2$. Anticipating on the following sections, we note that, associated with the enhancement factor eq. (5.18), this property of the bow-tie cavity is essential for performing efficient SHG, as in this case the energy only flows one way. We will come back to this point in greater detail in the relevant section.

5.3 The Jaynes-Cummings Hamiltonian

We now tackle the problem of the interaction of an atom with a single mode standing-wave electromagnetic field. We start with the Jaynes-Cummings model and then introduce the dressed-state picture which will provide us with a description of the interaction between the ion and the standing-wave cavity field.
The Hamiltonian of a coupled system containing a two-level atom interacting with a single-mode field is very similar to the one given in chapter 3, the only difference residing in the definition of the field which we now assume to be quantized:

$$H = H_A + H_F + H_{Int} \tag{5.22}$$

where H_F is equal to:

$$H_F = \hbar\omega_L \hat{a}^\dagger \hat{a} \tag{5.23}$$

and describes the field part where we have omitted the zero-point energy for convenience. The interaction part, H_{Int}, is defined as before:

$$H_{Int} = -\mathbf{D} \cdot \mathbf{E} \tag{5.24}$$

the only difference is that $\mathbf{E}$ is the single-mode quantized electric field:

$$\mathbf{E}(\mathbf{r}) = \boldsymbol{\epsilon}\mathcal{E}_0 f(\mathbf{r})(\hat{a} + \hat{a}^\dagger) \tag{5.25}$$

with $f(\mathbf{r})$ a form factor which describes the relative amplitude of the field, and $\mathcal{E}_0 = \sqrt{\frac{\hbar\omega_L}{2\epsilon_0 V}}$ is a normalization factor chosen such that $\epsilon_0\mathcal{E}_0^2$ is equal to the zero-point energy density of the electromagnetic field $\frac{\hbar\omega_L}{2V}$, with V the volume of the cavity. $\boldsymbol{\epsilon}$ represents the polarization of the field, $\hat{a}$ and $\hat{a}^\dagger$ are the usual annihilation and creation operators, ω_L is the field frequency.
Recalling the expression of $\mathbf{D}$ defined in (3.5):

$$\hat{\mathbf{D}} = \mathbf{d_{ge}}\hat{\sigma}_{ge} + \mathbf{d_{eg}}\hat{\sigma}_{eg} \tag{5.26}$$

with $\mathbf{d_{ge}} = \mathbf{d_{eg}} \equiv \mathbf{d}$ the dipole matrix elements for the transition and $\hat{\sigma}_{ij} = |i\rangle\langle j|$ with $i, j = \{g, e\}$ the lowering and raising atomic operators, we can re-express the interaction Hamiltonian using (5.25):

$$H_{Int} = -(\hat{\sigma}_{ge} + \hat{\sigma}_{eg})\mathbf{d} \cdot \mathbf{E} = -df(\mathbf{r})\mathcal{E}_0(\hat{\sigma}_{ge} + \hat{\sigma}_{eg})(\hat{a} + \hat{a}^\dagger) \tag{5.27}$$

where we have assumed that the field polarization and the dipole are parallel. The coefficient g introduced in eq. (3.7) is changed to $g_0(\mathbf{r}) = -\frac{d\mathcal{E}_0}{\hbar} f(\mathbf{r})$, and is known in the literature as the "vacuum Rabi splitting". The full Hamiltonian describing the atom, the light field and the coupling between them therefore reads:

$$H = H_A + H_F + H_{Int} = \hbar\omega_0\hat{\pi}_e + \hbar\omega_L\hat{a}^\dagger\hat{a} + \hbar g_0(\mathbf{r})(\hat{\sigma}_{ge} + \hat{\sigma}_{eg})(\hat{a} + \hat{a}^\dagger) \tag{5.28}$$

Applying the rotating-wave approximation (RWA), which consists in neglecting non energy-conserving terms in the equation (5.27), that is, keeping only terms describing the absorption of a photon accompanied with the transfer of the ion from state g to state e, and the transfer from e to g with the emission of a photon allow us to rewrite (5.28) as:

$$H_{Int} = \hbar g_0(\mathbf{r})(\hat{\sigma}_{ge}\hat{a}^\dagger + \hat{\sigma}_{eg}\hat{a}) \tag{5.29}$$

The resulting Hamiltonian:

$$H = \hbar\omega_0\hat{\pi}_e + \hbar\omega_L\hat{a}^\dagger\hat{a} + \hbar g_0(\mathbf{r})(\hat{\sigma}_{ge}\hat{a}^\dagger + \hat{\sigma}_{eg}\hat{a}) \tag{5.30}$$

is usually referred to as the Jaynes-Cummings Hamiltonian.
The "uncoupled" eigenstates of the Hamiltonian $H_A + H_F$ are given by the tensor products of atomic and field energy states $|e, n\rangle$ and $|g, n\rangle$. Their energies are, respectively, given by $\hbar\omega_0 + n\hbar\omega_L$ and $n\hbar\omega_L$. For a detuning Δ_L much smaller than ω_L, the excited states of $H_A + H_F$ are organized in a ladder of doublets $\{|g, n+1\rangle, |e, n\rangle\}$ separated from each other by the energy $\hbar\omega_L$. The atom-field coupling H_{int} only connects states inside each doublet, and is characterized by the Rabi frequency g defined as:

$$g(\mathbf{r}) = \frac{1}{\hbar}\langle e, n|H_{int}|g, n+1\rangle = -\sqrt{n+1}\frac{d\mathcal{E}_0}{\hbar}f(\mathbf{r}) = g_0(\mathbf{r})\sqrt{n+1} \tag{5.31}$$

Thus in principle g depends on n but, following [81], we shall drop this dependence by assuming that the laser is excited in a coherent state with a Poisson distribution for n, the width Δn of which is very small compared with the average number of photons n.

5.4 The dressed-states

The derivation of the eigenstates and eigenenergies of the Jaynes-Cummings Hamiltonian can be found in, e.g. [82, 83], therefore we will only reproduce them here. The eigenenergies read:

$$E_{1n} = (n+1)\hbar\omega_L + \frac{\hbar\Delta_L}{2} + \frac{\hbar\Omega(\mathbf{r})}{2} \tag{5.32}$$

and

$$E_{2n} = (n+1)\hbar\omega_L + \frac{\hbar\Delta_L}{2} - \frac{\hbar\Omega(\mathbf{r})}{2} \tag{5.33}$$

with $\Omega(\mathbf{r}) = \sqrt{g(\mathbf{r})^2 + \Delta_L^2}$, and $\Delta_L = \omega_0 - \omega_L$ is the atom-field detuning. These energies are associated to the eigenstates:

$$|n, 1; \mathbf{r}\rangle = \sin\theta(\mathbf{r})|n+1\rangle|g\rangle + \cos\theta(\mathbf{r})|n\rangle|e\rangle \tag{5.34}$$

$$|n, 2; \mathbf{r}\rangle = \cos\theta(\mathbf{r})|n+1\rangle|g\rangle - \sin\theta(\mathbf{r})|n\rangle|e\rangle \tag{5.35}$$

where $\cos 2\theta(\mathbf{r}) = \Delta_L/\Omega(\mathbf{r})$ and $\sin 2\theta(\mathbf{r}) = g(\mathbf{r})/\Omega(\mathbf{r})$. The states $|n, 1; \mathbf{r}\rangle$ and $|n, 2; \mathbf{r}\rangle$ are termed the dressed states. An important point here is that in an inhomogeneous laser field these energies and eigenstates depend on the position r. Out of the field, the dressed states reduce to the bare ones, and their splitting is given by $\hbar\Delta_L$. In the presence of the field however, the dressed states are a superposition of $|n+1\rangle|g\rangle$ and $|n\rangle|e\rangle$, and their splitting is given by $\hbar\Omega(\mathbf{r})$ which is larger than $\hbar\Delta_L$. Moreover, as can be seen on the dressed-state energy diagram shown on fig. 5.4, an ion prepared in the state g and placed in a red-detuned laser field has a lower energy than outside the field, and we can intuitively understand that in such configuration the ion will tend to seek the regions of high-intensity of the field, and hence can be trapped under certain conditions. On the other hand, in the case of blue-detuned field, the ion will, for similar reasons, seek regions of vanishing intensity.

With our notations, the energy difference between the bare atomic states is simply $\hbar\omega_0$. For an ion placed in e.g. a red-detuned laser field, the ground state $|g, n; \mathbf{r}\rangle$ connects to $|n-1, 2; \mathbf{r}\rangle$ and $|e, n; \mathbf{r}\rangle$ connects to $|n, 1; \mathbf{r}\rangle$. Thus the energy difference between these levels is shifted by an amount given by:

$$(E_{1n} - E_{2n-1}) - \hbar\omega_0 = \hbar\omega_L + \hbar\Omega(\mathbf{r}) - \hbar\omega_0 \tag{5.36}$$

$$= -\hbar\Delta_L + \hbar\Omega(\mathbf{r}) > 0 \tag{5.37}$$

In the case of red-detuned laser field, the frequency of the transition is therefore increased. In the case of a blue-detuned laser field, the state $|g, n; \mathbf{r}\rangle$ connects to $|n-1, 1; \mathbf{r}\rangle$, and $|e, n; \mathbf{r}\rangle$ connects to $|n, 2; \mathbf{r}\rangle$, and the energy difference is given by:

$$(E_{2n} - E_{1n-1}) - \hbar\omega_0 = \hbar\omega_L - \hbar\Omega(\mathbf{r}) - \hbar\omega_0 \tag{5.38}$$

$$= -\hbar\Delta_L - \hbar\Omega(\mathbf{r}) < 0 \tag{5.39}$$

The transition frequency is thus decreased. Finally, to conclude this part, let us mention another very useful result provided by this model. As shown in [81], it is possible to calculate the steady state populations of the dressed states. Since the details of the calculation can be found in the article mentioned above, we will simply recall the notations and main results. First, let us define the atomic populations in the states $|1; \mathbf{r}\rangle$ and $|2; \mathbf{r}\rangle$ as:

$$\hat{\pi}_1 = \sum_n \langle n, 1; \mathbf{r}|\hat{\rho}|n, 1; \mathbf{r}\rangle \tag{5.40}$$

and

$$\hat{\pi}_2 = \sum_n \langle n, 2; \mathbf{r}|\hat{\rho}|n, 2; \mathbf{r}\rangle \tag{5.41}$$

where $\hat{\rho}$ represents the density matrix for the combined ion-laser field system. In the limit of detunings far greater than the natural linewidth Γ of the excite state

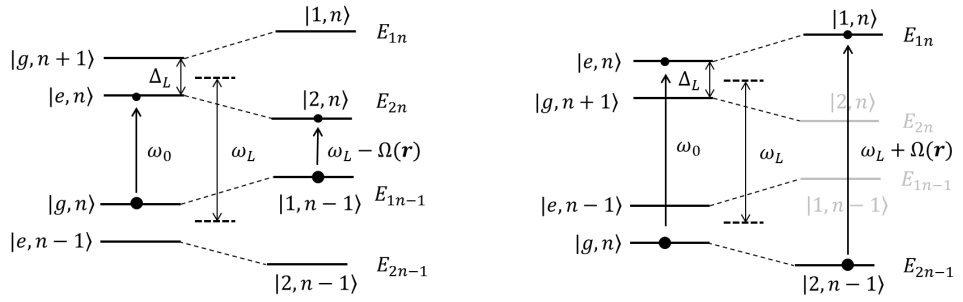

(a) (b)

Figure 5.4: Dressed-atom energy diagram. Each of the schematics shows the states of the combined atom-laser system without coupling (left), and the dressed-states (right). (a) Energy diagram in the case of an atom placed in a blue-detuned field. In the absence of coupling, the energy difference between the states $|e\rangle$ and $|g\rangle$ is equal to $\hbar\omega_0$. Assuming the system is prepared in the $|g, n\rangle$ state, subsequently increasing the coupling transfers the system to the state $|1, n-1\rangle$. The corresponding excited state is then $|2, n\rangle$, and the energy difference between them is $\hbar\omega_L - \hbar\Omega(\mathbf{r}) < \hbar\omega_0$. (b) Energy diagram in the case of an atom placed in a red-detuned field.In the absence of coupling, the energy difference between the states $|e\rangle$ and $|g\rangle$ is equal to $\hbar\omega_0$. Assuming the system is prepared in the $|g, n\rangle$ state, subsequently increasing the coupling transfers the system to the state $|2, n-1\rangle$.The corresponding excited state is then $|1, n\rangle$, and the energy difference between them is $\hbar\omega_L + \hbar\Omega(\mathbf{r}) > \hbar\omega_0$.

($|\Delta_L| \gg \Gamma$), the steady-state values of $\hat{\pi}_1$ and $\hat{\pi}_2$, which we will denote π_1^{st} and π_2^{st}, are given by:

$$\pi_1^{st} = \frac{\sin^4\theta(\mathbf{r})}{\sin^4\theta(\mathbf{r}) + \cos^4\theta(\mathbf{r})} \tag{5.42}$$

and

$$\pi_2^{st} = \frac{\cos^4\theta(\mathbf{r})}{\sin^4\theta(\mathbf{r}) + \cos^4\theta(\mathbf{r})} \tag{5.43}$$

The scattering rates from these states can thus be immediately estimated with knowledge of $g(\mathbf{r})$, $\Omega(\mathbf{r})$ and Δ_L, since they are directly proportional to the steady state populations. This will prove useful when we will have to adjust our experimental parameters in order to minimize the scattering due to the cavity field and maximize that of the probe beam.

The cavity field

So far we have not taken into account the fact that the field described here is an intracavity standing wave. This could be a problem since the dynamics of a field confined inside a cavity obeys the equations derived in section 5.2, and which depend on the cavity parameters - absorption and scattering losses, transmission through the

mirrors - in addition to the dynamics arising from the interaction with the atom, and described by the Hamiltonian (5.29). These equations would describe, in the case of a cavity mode frequency resonant or close to resonance with the atomic transition, the coherent exchange of energy between the atom and the cavity field at the rate g_0, and the decay of the field through the cavity mirrors with the decay rate $\kappa = \kappa_{\mathcal{L}} + \kappa_1 + \kappa_2$, or through spontaneous emission with a rate $\gamma = \frac{\Gamma}{2}$ from the atom into a mode different from the cavity-mode. In the case where the frequency g_0 exceeds both (κ, γ), we understand that the atom-cavity field dynamics will be dominated by the exchange of photons between the atom and the cavity field. In the limit where the ratio $\frac{g_0^2}{\kappa\gamma} > 1$ the system is said to be in the strong coupling regime of cavity QED. In our system, $g_0 = 2\pi \times 0.53$ MHz, $\kappa = 2\pi \times 2.1$ MHz and $\gamma = \Gamma/2 = 2\pi \times 11.2$ MHz [53], and thus a single ion placed at an antinode of the cavity mode is not strongly coupled with the field. However, with these parameters, the so-called collective strong coupling regime can be reached by placing ~ 500 cold ions in the cavity mode, and has been demonstrated in experiments described in [54]. One characteristic feature of this regime is the modification of the cavity decay rate and mode frequency due to the presence of the atoms, an effect termed generally *backaction* of the atoms on light. In particular, if the shift is comparable to the cavity linewidth, the cavity field intensity can be resonantly enhanced or suppressed, and so can the backaction on the atomic motion.

In the dispersive regime of cavity QED where the resonant exchange of energy between the atom and the field is suppressed, the backaction can be used to, e.g., cool down atoms and molecules [84], and has been studied in a wealth of experiments reviewed here [85]. Its effect in our experiment can be quantified through the shift of the cavity mode frequency due to the presence of the atom. This shift is equal to [82]:

$$\delta\omega_c = \frac{g_0^2}{4\Delta_L} \tag{5.44}$$

Using a detuning Δ_L of 760 GHz, we find that $\delta\omega_c = 0.082$ Hz, that is, the presence of an atom shifts the cavity mode frequency by an amount much smaller than the cavity mode linewidth 2κ. We therefore do not expect that the presence of an atom inside the cavity mode has an observable effect on the field dynamics, and we will neglect this aspect in the rest of this thesis.

Part II

Experimental Implementation

Chapter 6

Introduction

The following chapters are devoted to the description of the experimental setup used to perform the experiments described in this thesis. The ion trap and laser systems have been built over the years by a number of people. Only the parts relevant to the experiments will be presented with references to the previous theses when needed. The cavity ion trap was built by former PhD student Peter Herskind, based on the experience gained by PhD Anders Mortensen with the purpose to serve as a quantum memory for light using Ion Coulomb crystals (ICC), and is shown on fig 6.1. It is composed of a linear Fabry-Perot optical cavity integrated into a linear Paul trap similar to the one described in chapter 2. Details on design considerations, and theoretical analysis of a quantum memory using ICC can be found in their theses [53, 86].

Realizing a quantum memory for light requires, among other things, an optically dense medium in order to increase the efficiency of storage. Entering the strong coupling regime of cavity QED by placing an ion inside an optical cavity could therefore be a possible solution, since the optical density of the atomic medium is, in this case, dramatically enhanced [82]. However, entering the strong coupling regime at the single ion level is difficult because the integration of an optical cavity with a small mode volume into a linear Paul trap is not straightforward (see, e.g., section 8.1.2 and [53, 86]), and although a few groups have obtained strong interactions between single ions and a cavity field mode [87–92], entering the single ion strong coupling regime has not been achieved yet. An alternative to working with single ions is to make use of an ion-crystal in order to benefit from the collective enhancement of coupling to an ensemble of two-level systems, and in 2008 the *collective* strong coupling regime of cavity QED was demonstrated in the Ion Trap Group [53, 54]. In this regime an ensemble of two-level atoms interact with a near-resonant single mode of the cavity in the low saturation regime, and the effective coupling rate $g_N = g_0\sqrt{N}$ can be made larger than both γ and κ [82]. In our case, as mentioned in section 5.4, this was achieved in our group with ICCs consisting of $\sim$ a few thousand ions. Besides being technologically less demanding, the use of an ICC placed in the mode of an optical cavity possess the advantage over single ions that it could in principle allow for multimode storage of light, and progress in this direction was made with the demonstration of collective strong coupling regime for different transverse cavity modes [93]. Another step towards the realization of a quantum memory was taken when cavity electromagnetically induced transparency (cavity EIT, see [94, 95]) and

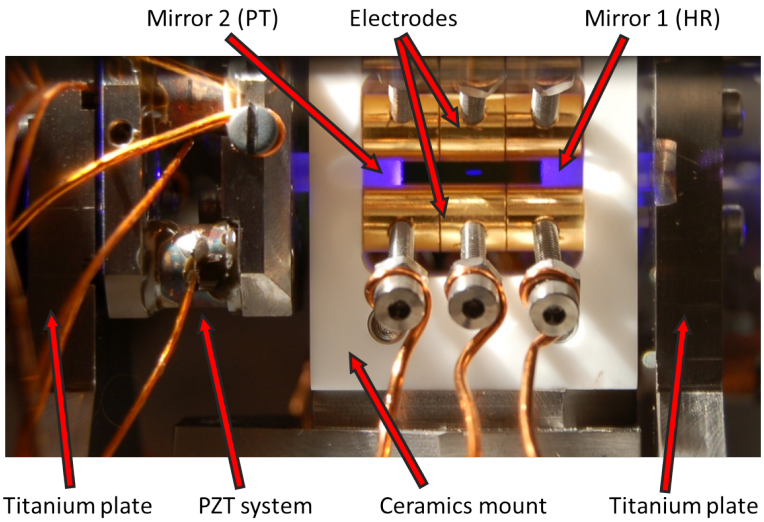

Figure 6.1: Photo of the cavity trap inside the vacuum chambers seen through a view port. The cylindrical electrodes are made from gold coated copper, and are attached to the ceramic mount. The cavity mirrors are embedded in dielectric mirror coats used to minimize the bending of RF-lines due to presence of the mirrors, and mounted on two titanium plates. The high-reflecting (HR) mirror is attached directly on a fixed titanium plate, while the partially transmitting (PT) is mounted on a PZT plate to allow for precise control of the cavity length. On the picture, the mirror coats appear blue because of the scattering of Doppler-cooling light at 397 nm sent through them.

all-optical switching were observed [80, 96].
Nevertheless, using an ICC placed inside an optical cavity to store photons using cavity EIT imposes several constraints, in particular on the configuration of laser beams used to address the ions [80], and on the possibility to keep the ions cold during the process [86]. Studies carried out by A. Mortensen and master student Kasper Zangenberg showed that trapping two components crystals could prove very useful, by using the inner component to store the photonic excitations, while at the same time sympathetically cool it with the outer one [86]. Moreover, the outer component can be used to shape the inner one in order to increase the number of interacting ions inside the cavity mode [97]. Using for two-components crystal a different isotope of $^{40}Ca^{+}$ implies that the cooling transition has a different wavelength, and therefore two Doppler cooling sources for addressing of each isotope are required. Such sources operate in the UV frequency range, and can be built by using an infrared laser source, and doubling its frequency in a process called second harmonic generation (SHG). Building such a source was therefore the first task I was involved in, and this work is presented in the next chapter.
In the case of a one-dimensional intracavity standing wave the single ion-light coupling varies sinusoidally with the position of the ion along the standing wave (see, e.g. chapter 5). In the case of an ICC placed in the cavity mode, the positions of the ions are uncorrelated with the intracavity standing wave antinodes, and the

light-matter coupling is in this case described through an averaged coupling strength $g_{N,av} = g/\sqrt{2}$. Controlling the positions of the ions with respect to the antinodes of the intracavity standing wave can therefore be very valuable, and was the main motivation for demonstrating localization of ions inside an optical trap, achieved by PhD student Rasmus B. Linnet on this same experimental setup [64]. The work presented in this thesis is a continuation of the work on localization, and most elements of the experimental setup were built prior to my arrival in the ion Trap Group. We will, in chapter 8, describe them briefly, but with enough details to give the reader a good overview of the workings and overall functions of the setup. We start with a description of the cavity trap, in section 8.1, and subsequently present the laser sources used in connection with the experiments on $^{40}Ca^{+}$ in section 8.3. Finally, in chapter 9, we look into the details of our detection and imaging system, and provide an analysis of the detection process which we use in the last part of this thesis.

Chapter 7

A frequency-doubled laser source for laser cooling of Ca^+ ions

In this chapter we detail the construction of a frequency-doubled laser system, which is intended to serve in experiments involving ion Coulomb crystals, or two-components Coulomb crystals. This source is composed of a tapered amplifier diode laser TA pro (Toptica) generating light at 794 nm, subsequently frequency doubled in a bow-tie cavity containing a periodically poled KTP (ppKTP) non linear crystal and frequency stabilized to a reference cavity using a Pound Drever Hall (PDH) scheme. We start by recalling the theory of second harmonic generation (SHG) in section 7.1.1, and introduce the Boyd Kleinman theory used to calculate relevant parameters of our setup in section 7.1.2. A characterization of the non linear crystal in which the frequency-doubling process takes place is presented in section 7.1.3. As we will see, the process needs high input power in order to produce frequency doubled light with high efficiency. This will be provided by the use of a cavity since the intracavity signal intensity is enhanced with respect to the input power - as we saw in section 5.1 - and will the topic of section 7.2. The last section (7.3) deals with the active stabilization of the laser frequency.

7.1 Second harmonic generation

7.1.1 Theory

The propagation of an electromagnetic field through a non-magnetic, neutral dielectric medium induces a polarization, which can be, provided the electric field is not too strong, described as:

$$\mathbf{P}(t) = \epsilon_0 \chi \mathbf{E}(t) \tag{7.1}$$

where $\mathbf{E}(t)$ is the total electric field, produced partly by free charges outside the medium, and partly by the polarization itself, ϵ_0 the vacuum permittivity and the linear susceptibility χ is a tensor of rank 2, since the polarization need not be along the same direction as the applied field. Eq. (7.1) implies a linear relationship between the total field and the polarization, and this is the result of an approximation associated with the fact that one in this case assumes the electrons in the medium to be slightly pushed away from their equilibrium position around the nuclei. In order words, the

electrons in such case only "probe" the harmonic part of the potential that binds them to the nuclei. This approximation breaks down when the applied electric field is strong enough. In such a case, the polarization is better described by an expansion in powers of **E**:

$$\mathbf{P}(t) = \epsilon_0 \chi \mathbf{E}(t) + d^{(2)}\mathbf{E}(t) \cdot \mathbf{E}(t) + \cdots \tag{7.2}$$

where d^2 is a tensor of rank 3. Assuming a monochromatic electric field of frequencey ω $\mathbf{E}(t) = \mathbf{E}_0 \cos(\omega t)$, the second order response of the medium manifests itself by a time-varying polarization oscillating at twice the applied field frequency

$$\mathbf{P}^{(2)}(t) = d^{(2)}[\mathbf{E}_0 \cos(\omega t)]^2 = \frac{1}{2} d^{(2)}(\mathbf{E}_0)^2(1 + \cos(2\omega t)] \tag{7.3}$$

The time-varying polarization, in turn, generates an electric field at frequency 2ω, which can be seen from the wave-equation satisfied by the total electric field inside the medium:

$$\nabla^2 \mathbf{E} - \frac{1}{c^2}\frac{\partial^2 \mathbf{E}}{\partial t^2} = \frac{1}{\mu_0 c^2}\frac{\partial^2 \mathbf{P}}{\partial t^2} \tag{7.4}$$

In a simple plane wave model, the second order polarization travels through the medium at a phase velocity $\frac{c}{n_\omega}$ with a wavevector $2k_\omega$, since it is generated by the field oscillating at ω. The newly generated field on the other hand oscillates at twice the frequency and thus possesses a wavevector $k_{2\omega}$ and phase velocity $\frac{c}{n_{2\omega}}$. Due to the dispersive property of the non-linear medium, the phase velocities and wavevectors of these two fields are generally not equal, resulting in destructive interferences between second harmonic waves generated at different points within the crystal (see Fig. 7.1). Denoting $\Delta k = k_{2\omega} - 2k_\omega = \frac{2\omega}{c}(n_\omega - n_{2\omega})$ the so-called phase mismatch, it can be shown that the second harmonic intensity, after propagation over a length z in the crystal and neglecting the depletion of the fundamental field, reads [98]:

$$I_{2\omega}(z) \propto I_\omega^2 z^2 \left(\frac{\sin(\frac{1}{2}\Delta k z)}{\frac{1}{2}\Delta k z}\right)^2 \tag{7.5}$$

For a given phase mismatch Δk one can also define a coherence length $L_{coh} = \left|\frac{\pi}{\Delta k}\right|$, which can be seen as the distance over which the different "waves" interfere constructively, hence producing a finite amount of second harmonic power. Operating at $\Delta k = 0$ thus corresponds to an infinite coherence length. In practice, the fundamental beam is sent through a crystal of a given length l_c, and cross section S. We are interested in the power of second harmonic light at phase matching condition - this is the physical quantity which can be accessed - so in terms of the light power, the previous equation can be rewritten:

$$P_{2\omega}(l_c) = \gamma P_\omega^2 \tag{7.6}$$

The coefficient γ is called the single-pass conversion coefficient. This coefficient depends on the medium in which the SHG process takes place, but also on the volume of interaction between the light beam and the medium. As we will see it in the next chapter, the theory developed by Boyd and Kleinman [99] allows us to explicitly calculate this coefficient, which depends on the effective nonlinear coefficient of the crystal and the beam geometric parameters.

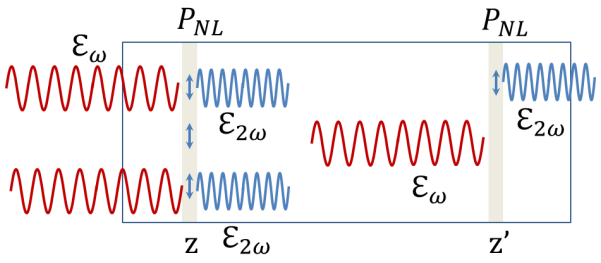

Figure 7.1: The incident field at ω (wavy red lines) generates the nonlinear polarization (small vertical arrows) which in turns gives rise to the second harmonic field (blue wavy lines). Getting an appreciable power at the output of the medium requires having the second harmonic waves generated at every couple (z, z') interfere constructively with each other (phase matching).

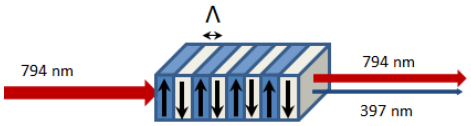

Figure 7.2: Schematic view of the PPKTP crystal, showing the ferroelectrics domains, and the alternating polarization. For the crystal used in the work presented here, $\Lambda = 3.15\ \mu m$.

7.1.1.1 Critical versus non critical phase matching

One of the challenges for efficient SHG is to achieve good phase-matching throughout the medium. Getting to $\Delta k = 0$ requires to be able to tune the refraction index of the material in order to reach a point where $2k_\omega = k_{2\omega}$. Two methods are traditionally used to achieve the phase-matching condition:

- by using a birefringent crystal, and changing its optical axis' orientation with respect to the incident field, one can change the refraction index of the field propagating along the extraordinary axis. This is referred to as critical phase matching.
- one can also change the refraction index by changing the temperature of the medium. This is called noncritical phase matching - as the direction of the incident field is not a critical parameter in this case - and it is this type of phase matching we deal with in this section.

It is worth noting that each of these methods assume a linearly polarized incident field.

7.1.1.2 The ppKTP crystal

ppKTP stands for periodically-poled potassium titanyl phosphate, or $KTIOPO_4$. It is a ferroelectric crystal, meaning that the material is structured into domains which

exhibits permanent polarization, in the very same way that a ferromagnetic material is structured into domains of permanent magnetic field. Furthermore, it is periodically poled: a periodic structure of regularly spaced ferroelectric domains with alternating orientations is artificially induced in the crystal by applying a high voltage electric pulse during the growth process [100].
In practice, the alternating sign of the ferroelectrics domain can be expressed as a periodic change of the sign of the non linear susceptibility (see Fig. 7.2), the effect of which being to induce a π phase shift of the second harmonic field. The natural dephasing between the fundamental and second harmonic fields can then be compensated and set back to 0 after a length corresponding to the width of a layer - denoted Λ thereafter. This additional spatial modulation of the second harmonic field with a period Λ implies that the phase matching condition has to be replaced by a quasi-phase matching condition which reads [101]:

$$\Delta k = 2k_\omega - k_{2\omega} - \frac{2\pi}{\Lambda} = 0 \tag{7.7}$$

This condition can be understood by remarking that the fundamental and second harmonic fields must be in-phase after traveling over a length Λ in the crystal:

$$2k_\omega \Lambda - k_{2\omega}\Lambda = 2\pi \tag{7.8}$$

For the crystal used, manufactured by RAICOL crystals, $\Lambda = 3.15$ μm. The values of $n(\omega)$ and $n(2\omega)$ can be tuned by changing the crystal temperature, which allows to increase the coherence length, and thereby the conversion efficiency. To achieve quasi phase-matching, the crystal therefore needs to be actively stabilized in temperature.

7.1.2 Optimization of SHG - the Boyd Kleinman theory

As mentioned in section 7.1.1 it is crucial to optimize the single-pass conversion coefficient γ in order to generate a substantial amount of frequency double light. Such an optimization is realized thanks to the theory developed by Boyd and Kleinman, which allows one to calculate this coefficient. It assumes a purely Gaussian TEM_{00} mode for the fundamental light, which is an idealized situation, although fairly close to the reality as the use of a high-finesse cavity will, in addition to the frequency filtering mentioned earlier, act as a mode filtering and hence enable the experimentalist to inject in the crystal an almost "perfect" TEM_{00} mode. We will first briefly introduce the Gaussian beam formalism, before presenting the Boyd-Kleinman theory.

7.1.2.1 Gaussian beam - waist - Rayleigh range

A Gaussian beam has an intensity profile of the form :

$$I(x,y,z) \sim |\mathcal{E}(\mathbf{r})|^2 = |\mathcal{E}_0(\mathbf{r})|^2 \exp\left[\frac{-2(x^2+y^2)}{w(z)^2}\right] \tag{7.9}$$

i.e., the transverse intensity profile has a Gaussian shape. The quantity $w(z)$ characterizes the transverse extent of the beam is therefore called the spot size. It can be shown [98] that the quantity $\mathcal{E}(\mathbf{r})$ can be written as:

$$\mathcal{E}(\mathbf{r}) = \frac{A}{1+iz/z_0} \exp\left[\frac{ik(x^2+y^2)}{2R(z)}\right] \exp\left[\frac{-(x^2+y^2)}{w^2(z)}\right] \tag{7.10}$$

where:

- The spot size $w(z)$ depends on z and z_0 through $w(z) = \sqrt{1 + z^2/z_0^2}$. It takes its minimal value for $z = z_0$, and $w(z = z_0) = w_0$ is referred to as the waist of the beam.
- $z_0 = \frac{\pi w_0^2}{\lambda}$ where λ is the wavelength of the field $\mathcal{E}(\mathbf{r})$, is the Rayleigh range. It is the length over which the spot size changes from w_0 to $\sqrt{2}w_0$, so it is a measure of the length of the waist region. The smaller the waist, the smaller the Rayleigh range, and conversely.
- $R(z) = z + \frac{z_0^2}{z}$ is the radius of curvature of the beam at the position z.

It is common to define a parameter $q(z)$ as:

$$\frac{1}{q(z)} = \frac{1}{R(z)} + \frac{i\lambda}{\pi w^2(z)} \tag{7.11}$$

since, as we will see later, this parameter is sufficient to describe the propagation of a Gaussian beam through different optics like lenses, mirrors etc...

7.1.2.2 The Boyd Kleinman theory

The Boyd Kleinman theory describes explicitly what efficiency for the production of second harmonic light one should ideally expect when sending a Gaussian beam of a giving spot size through a crystal of given length, absorption, and effective nonlinear

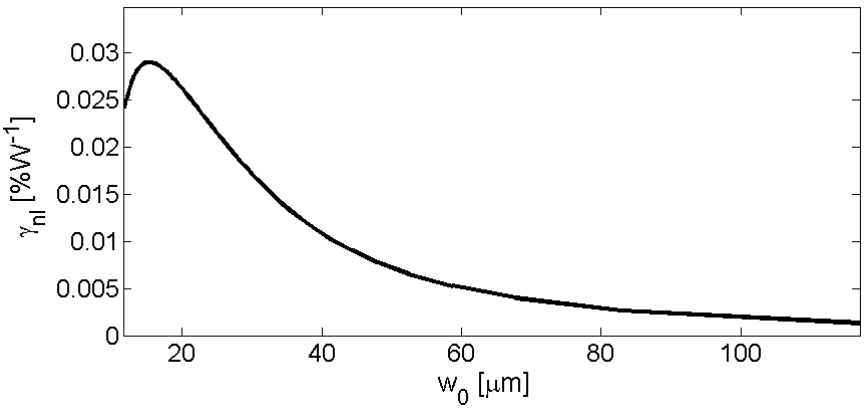

Figure 7.3: Numerical calculation of the single pass conversion coefficient versus the waist size. The effective nonlinear coefficient used here is 9.50 pm/V [101]. The Boyd-Kleinman theory predicts an optimal waist of 15μm but we use in practice a substantially larger waist to reduce thermal effects. The crystal length is 10 mm, the refraction indices at the fundamental and second harmonic frequencies (corresponding to wavelengths of 794 nm and 397 nm) are $n_\omega = 1.8461$ and $n_{2\omega} = 1.9711$, respectively.

conversion coefficient d_{eff}. The single-pass conversion efficiency γ is given by [99]:

$$\gamma = \frac{P_{2\omega}}{P_\omega^2} = \left(\frac{2\omega^2 d_{eff}^2 k_\omega}{\pi n_\omega^2 n_{2\omega} \epsilon_0 c^3} \right) l_c h(\sigma, \xi) \tag{7.12}$$

where $P_{2\omega}$, P_ω represent the second harmonic and fundamental power respectively,and $h(\sigma, \xi)$ is the Boyd Kleinman focusing factor, it contains all the dependence of $P_{2\omega}$ upon the optimizable parameters, σ and ξ representing respectively the phase mismatch and strength of focusing. The above formula is given in the case of standard phase matching, but it can be shown - see [99] for example - that the formula (7.12) is formally the same in the case of quasi phase-matching, provided that the values of the non linear coefficient d_{eff} and of the phase mismatch σ take into account the modifications due to the use of a periodically poled crystal. In particular, this involves replacing the phase mismatch with the quasi phase-mismatch in formula (7.12).

As can be seen on the Fig.7.3, the efficiency depends on the waist in a non trivial way : the optimal theoretical value corresponds to a trade-off between the intensity and the divergence of the fundamental beam, as strong focusing inside the crystal is obtained at the expense of a shorter Rayleigh range. Seeing a gaussian beam as a pencil of diverging plane waves, we can understand this trade-off in terms of the spread of wave-vectors represented in the field versus the ratio of the wave vectors effectively contributing to the second harmonic generation.

In practice, the use of very intense laser beams also leads to nonuniform heating of the crystal, and hence nonuniform phase matching condition throughout the section of the crystal. This, in practice, will cause the crystal to expand, thus changing the phase matching condition. This effect can be compensated up to a certain point by lowering the temperature of the crystal, but at very high intensity it will not be possible to maintain a homogeneous temperature locally. This sets an upper bound on the intensities we may use, for a given waist, to get a stable output. The practical choice of waist will result from a trade-off, which takes these effects into account in addition to the theoretical ones mentioned above (see for example, [102]).

7.1.3 Characterization of the PPKTP crystal

Before inserting the nonlinear crystal in the cavity, it is important to characterize its single pass properties. This characterization principally amounts to measuring the single pass conversion coefficient, and the losses through the crystal, through measurements of the transmission. The nonlinear crystal has a length $l_c = 10$ mm, is anti-reflexion coated at 794 nm and 397 nm on both facets, and has absorption coefficients of $\alpha_{794} = 0.5\%\text{cm}^{-1}$ for light at 794 nm and $\alpha_{397} = 15.1\%\text{cm}^{-1}$ for ligth at 397 nm.

7.1.3.1 Transmission measurement

We chose to perform measurements of the transmission through the crystal at different points, in order to detect possible position-dependent defects in the crystal structure or in the anti-reflection coating applied on the surfaces. These defects could, indeed, have a non negligible impact on the conversion efficiency. The idea is also to determine the possible good "spots" on the crystal for the production of UV light. To prevent

any misleading absorption effect due to the production of UV light, the temperature at which these measurements have been performed has been carefully chosen far away from the phase-matching temperature. The results we obtained are shown on Fig. 7.4(a). The results clearly displays some features, which can be explained by, for example, a non uniform anti-reflection coating, or impurities in the crystal structure, resulting in inhomogeneous absorption of the fundamental light. A possible way to investigate these possibilities further would be to perform reflectivity measurements. We did not perform these measurements because of practical technical difficulties, as these numbers depend on the orientation of the incident beam with respect to the crystal surface, and also because we were mainly interested in the losses, not in the detailed crystal structure at that point.

7.1.3.2 Single-pass conversion coefficient

We then went on measuring the infrared to ultraviolet conversion coefficient. This coefficient depending on the focusing, we chose to perform the measurements using a waist of 35 μm, as this is the size we intended to use to perform the intracavity SHG. Recalling that this coefficient is defined as $\gamma = P_{2\omega}/P_{\omega}^2$, we got the results displayed on Fig. 7.4(b). Once again, the results show some non uniformity over the crystal surface. Because it seems that there is no correlation between these measurements and the transmission measurements, this indicates that the poling might not be homogeneous through the crystal volume [103]. Another striking feature is the low values obtained for this coefficient when compared with the theoretical ones calculated using the Boyd Kleinman theory. Indeed, we expect γ to be around 1%, whereas it can be seen from Fig. 7.4(b) that its values range from ~ 0.5 % to ~ 0.7 %. We investigated whether this discrepancy could come from some deviation of the laser beam with respect to the perfect Gaussian TEM_{00} mode assumed in Boyd Kleinman calculations. This non-perfect Gaussian character can be observed on Fig. 7.5(a) where a measurement of the waist of the laser beam is displayed by noticing the different values for the waists sizes and positions in horizontal and vertical directions. This astigmatism can also be accounted for by the value of the beam quality coefficient M^2 which is specified by Toptica to be <1.5 in our case - and equals 1 for a perfect Gaussian beam. To test our hypothesis, we coupled the incoming beam to a single-mode optical fiber, since it acts

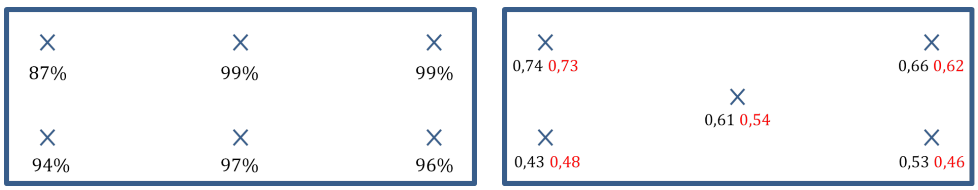

(a) (b)

Figure 7.4: (a) Measurement of the transmission of 794 nm light through the crystal at different points. (b) Measurement of the single-pass conversion coefficient at different points, before (black) and after (red) spatially filtering the beam with the optical fiber. The units are $\%W^{-1}$. All the results come with a fractional uncertainty of $\pm 12\%$ due to large fluctuation in the UV power and uncertainty of position of the beam from one measurement to another.

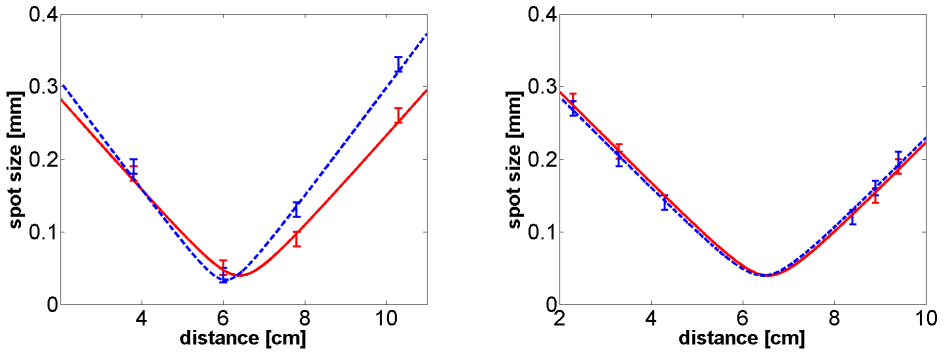

(a) (b)

Figure 7.5: (Both figures) Measurement of the waist size in vertical (blue dotted line) and horizontal (red solid line) directions. (a) The beam is assumed to be Gaussian in each direction, but with different focusing parameters. waist value from fit: (34 ± 3) μm (vertical) and (40 ± 3) μm (horizontal). (b) After filtering through the fiber. The beam is assumed to be Gaussian in each direction, but with different focusing parameters. Here the waist sizes are the same, up to the experimental precision of ± 5 μm on every data points. Waist values from the fit: (40 ± 2) μm.

as a mode-filter. Comparison of the waist measurements before and after coupling to the fiber shows the sought-after filtering effect (see Fig.7.5(a) and Fig.7.5(b)).

As can be seen on Fig. 7.4(b), filtering the beam has no noticeable effect on the efficiency, when taking into account the uncertainty on the different measurements. However, one could still argue that the values obtained in the second case are slightly lower than in the first case, but this could probably be explained by the fact that the beam size after filtering was a bit larger than before filtering.

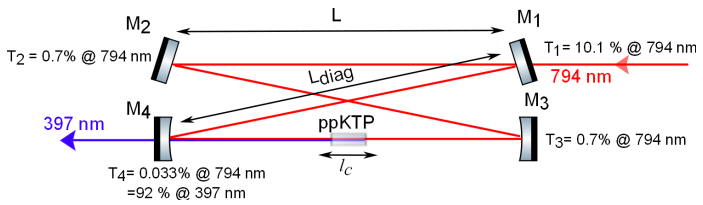

Figure 7.6: Schematic of the cavity used for SHG of light at 397nm. Relevant lengths are L=12 cm L_{diag}=12.07cm and l_c = 1 cm.

.

7.2 Intracavity SHG

7.2.1 The bow-tie cavity. Modematching.

The cavity used is a bow-tie cavity, and is sketched Fig.7.6. It is made of two plane mirrors (M_1, M_2) and two curved mirrors (M_3 and M_4). The transmissivity of the input coupler M_1 is $T_1 = 10.1\%$, whereas $T_2 = T_3 = 0.7\%$ and the output coupler M_4 is high reflexion coated for ligth at 794 nm, and highly transmissive for light at 397 nm: T_4=0.033% at 794 nm and 92% for light at 397 nm. The distance between the pair of mirrors being the same, the cavity is said to be symmetrical. The steady state of field corresponds to the beam being focused twice inside the cavity, first halfway between the two plane mirrors -the waist at this position is referred to as the secondary waist-, and a second time halfway between the two curved mirrors. The latter being smaller than the former, we will refer to it as the small waist in the following.
As mentioned previously, the field in such a bow-tie cavity is a running wave, with benefits in connection to SHG already evoked in section 5.1.1. Another benefit from using a bow-tie cavity is the low level of optical feedback to the laser, thanks to the small angle between the incident and the reflected field. This comes at a price though, as it implies a non axis-symmetric design, which causes astigmatism in the resonator mode - the waists along vertical and horizontal directions are not exactly located exactly at the same point. This can be minimized by placing the two pairs of mirrors as close to each other as possible, with the limitation that there need to be enough room for the oven.
During normal operation, the cavity is locked to the laser to achieve stable UV power output. This is achieved by mounting the mirror M_2 on a piezoelectric element, and by applying a voltage to allow for active control of the mirror position. The locking scheme is of the Hänsch-Couillaud type [104], and the whole setup is depicted on Fig.7.7. In the original proposal from Hänsch and Couillaud a linear polarizer is placed inside the cavity. In our case two - half- and quarter- - wave plates are placed outside the resonator. We take advantage of the natural birefringence of the dielectric mirrors to perform the desired rotation of the polarization axis of the incoming field, and use the $\lambda/2$ wave plate to rotate the polarization axis with respect to the fast axis of the $\lambda/4$ wave plate. The latter is then used in combination with the polarization beam splitter to analyze the ellipticity of the beam, following the Hänsch-Couillaud scheme.

In the context of frequency doubling, the property which we are mostly interested in is the enhancement of the field intensity inside the cavity. Inserting a nonlinear crystal inside an optical cavity is not completely straightforward though, as several parameters have to match together. The following section is dedicated to the design of such a cavity.

7.2.1.1 The ray-matrix method

The size of the small waist depends on the radius of curvature and distance between the two curved mirrors - which automatically sets the distance between the plane mirrors in the case of a symmetrical cavity.
The former PhD student who initially designed this cavity used a different laser system

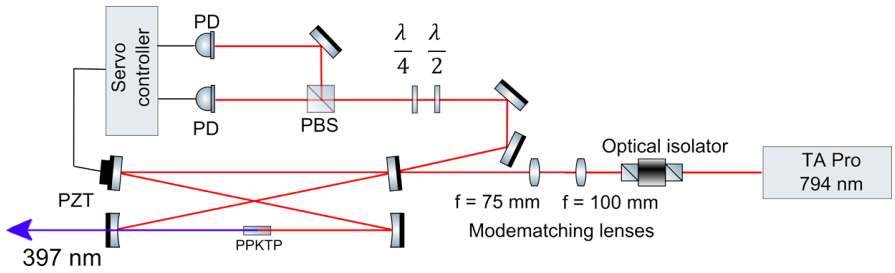

Figure 7.7: Schematic of the setup used for SHG. A tapered-amplifier diode laser (Toptica TA Pro) generates light at 794 nm. The laser beam is sent through an optical isolator in order to avoid backreflections to the diode laser, and is coupled to the bow tie cavity containing the non-linear ppKTP crystal in which the frequency-doubling process takes place (blue output after the crystal). The reflected field is used to stabilize the length of the cavity with a Hänsch-Couillaud scheme.

- a home-built external cavity laser diode, whereas we use a tapered amplifier laser (Toptica TA PRO) at the same wavelength, but with a different output profile. In order to mode match the new laser beam to the existing cavity, we use the so-called ABCD-matrix formalism [105], which allows us to very simply compute the size and direction of a laser beam, given a specific input, after it has traveled through different optics. For example, if the q parameter of a Gaussian beam has a value q_i at some position in space, then after propagating over a distance d, and then through a lens of focal length f, the final q parameter q_f reads:

$$q_f = \frac{q_i + d}{-\frac{q_i}{f} + 1 - \frac{d}{f}} \tag{7.13}$$

More generally,

$$q_f = \frac{Aq_i + B}{Cq_i + D} \tag{7.14}$$

The coefficients A, B, C, D in (7.13) can be read-off from the matrix

$$\begin{bmatrix} A & B \\ C & D \end{bmatrix} = \begin{bmatrix} 1 & d \\ -\frac{1}{f} & 1 - \frac{d}{f} \end{bmatrix} \tag{7.15}$$

7.2.1.2 Modematching

We start by calculating the matrix coefficients over a round trip of the cavity, and imposing that the beam should be the same after a round trip. Starting at the

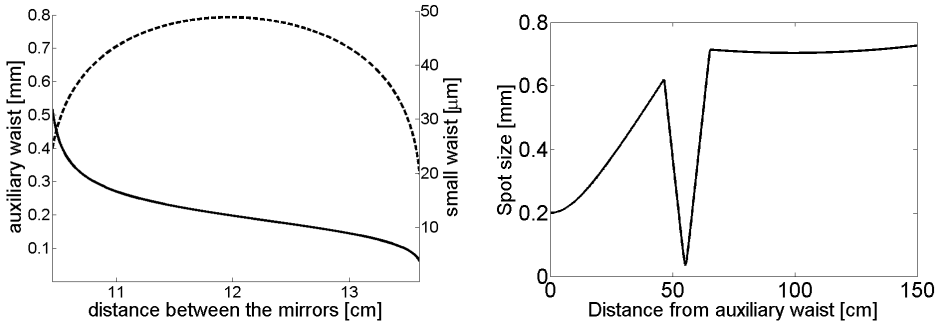

(a) (b)

Figure 7.8: (a) Solid and dashed lines: respectively auxiliary and small waists versus the distance between the cavity-mirrors, in the case of a symmetric cavity. The radius of curvature of the mirrors is R = 100 mm, the spacing between each pair of mirrors is 1.3 cm. (b) Numerical calculation of the laser's spot size versus the distance from the auxiliary waist. The first lens is located 46.5 cm after the auxiliary waist and has a focal length of 75 mm. The second lens is located 65.5 cm after the auxiliary waist, and has a focal length of 100 mm

secondary waist:

The A, B, C, D coefficients over a round trip of the cavity :

$$\begin{bmatrix} A & B \\ C & D \end{bmatrix} = \overbrace{\begin{bmatrix} 1 & L/2+L_{diag} \\ 0 & 1 \end{bmatrix}}^{\text{to secondary waist}} \overbrace{\begin{bmatrix} 1 & 0 \\ -\frac{2}{R} & 1 \end{bmatrix}}^{\text{refl. on } M_3} \overbrace{\begin{bmatrix} 1 & (L-l_c)/2 \\ 0 & 1 \end{bmatrix}}^{\text{to } M_3} \overbrace{\begin{bmatrix} 1 & 0 \\ 0 & n \end{bmatrix}}^{\text{cr. surf.}} \overbrace{\begin{bmatrix} 1 & l_c/2 \\ 0 & 1 \end{bmatrix}}^{\text{to cr. surf.}} \times$$
$$\underbrace{\begin{bmatrix} 1 & l_c/2 \\ 0 & 1 \end{bmatrix}}_{\text{to cr. center}} \underbrace{\begin{bmatrix} 1 & 0 \\ 0 & 1/n \end{bmatrix}}_{\text{cr. surf.}} \underbrace{\begin{bmatrix} 1 & (L-l_c)/2 \\ 0 & 1 \end{bmatrix}}_{\text{to cr. surf.}} \underbrace{\begin{bmatrix} 1 & 0 \\ -\frac{2}{R} & 1 \end{bmatrix}}_{\text{refl. } M_3} \underbrace{\begin{bmatrix} 1 & L_{diag}+L/2 \\ 0 & 1 \end{bmatrix}}_{\text{from secondary waist to } M_3} \tag{7.16}$$

Imposing that the beam should be identical after one round trip is equivalent to the following stability condition:

$$-1 \leq \frac{1}{2}(A+D) \leq 1 \tag{7.17}$$

the waist w_0 is given by:

$$w_0 = \left| \left(\frac{\lambda}{\pi}\right)^{1/2} \frac{B^{1/2}}{(1-(1/4)(A+D)^2)^{1/4}} \right| \tag{7.18}$$

On Fig. 7.8(a), are plotted several values of secondary and small waists with respect to the distance between the mirrors. Finally, the laser's output spot size is matched to the desired secondary waist by using a set of two lenses in a telescope configuration, which positions and focal lengths are deduced from a calculation of the same kind as

the one discussed above. The numerical simulation corresponding to the configuration of the current setup is shown Fig. 7.8(b). This configuration results from a choice of a small waist of about 50 μm and auxiliary waist of 200 μm. We chose a small waist larger than the previously chosen value of 35 μm, in order to minimize heating effects in the crystal (see section 7.2.3). It corresponds to a distance between the mirrors L and L_{diag} of respectively 12 cm and 12.07 cm. Once the cavity is modematched, a signal like the one presented on Fig. 5.1.1 can be observed. On Fig. 7.9, pictures of the final setup can be seen.

7.2.2 Characterization of the cavity

As mentioned in the beginning of this chapter, the power available inside the cavity strongly depends on the transmission and reflection coefficients of the mirrors, as well as the losses in the cavity. In an empty cavity, the losses are only due to scattering off and absorption in the the mirrors, but in the case of intracavity SHG, the crystal will also act as a lossy medium. Moreover, we always assumed so far that the incoming beam was perfectly coupled to the cavity, which is not the case in practice since the laser output mode is not purely TEM_{00}. Quantifying the losses, and the proportion of the incident beam effectively coupled to the cavity will allow us to predict the maximal attainable enhancement factor, and hence check whether or not the cavity is well aligned.

7.2.2.1 Quantifying the losses in the case of a non perfect coupling of the beam to the cavity

The losses can be quantify by measuring the reflection signal from the cavity on and off resonance, and by using the results obtained section 5.1.1, and in particular the equations (5.20) and 5.21. To explicitly take into account the non perfect mode matching of the laser field to the cavity, we define $|E_{ref}|^2$ as the sum of two incoherent contributions :

$$|E_{ref}|^2 = R_0|E_{in}|^2 + R'|E'_{in}|^2 \tag{7.19}$$

E'_{in} denoting the amount of light which does not couple to the cavity. Mathematically, this would amount to decompose the field in all the transverse mode components, keeping in the E_{in} term only the TEM_{00} part of the spectrum while putting the other modes in the E'_{in} term. These two terms being orthogonal, they do not interfere with each other and their intensities just add up on the detector. The coefficient R' then simply denotes the input coupler's reflectivity, the coefficient R_0 being the resonant reflection from the cavity:

$$R_0 = \frac{(\mathcal{L} - T_1 + T_2)^2}{(\mathcal{L} + T_1 + T_2)^2} \tag{7.20}$$

To quantify the ratio of coupled over non-coupled light to the cavity we can define a new parameter η as :

$$\eta = \frac{|E_{in}|^2}{|E_{in}|^2 + |E'_{in}|^2} \tag{7.21}$$

It can then be shown that the measured reflection reads :

$$R = R_0\eta + R'(1 - \eta) \tag{7.22}$$

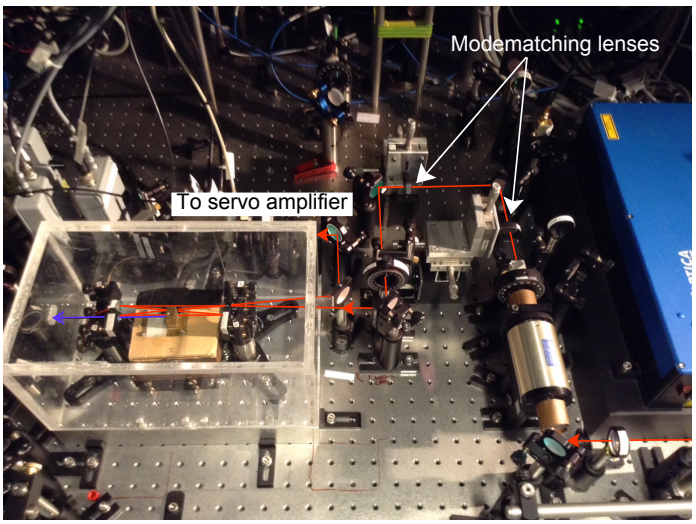

(a)

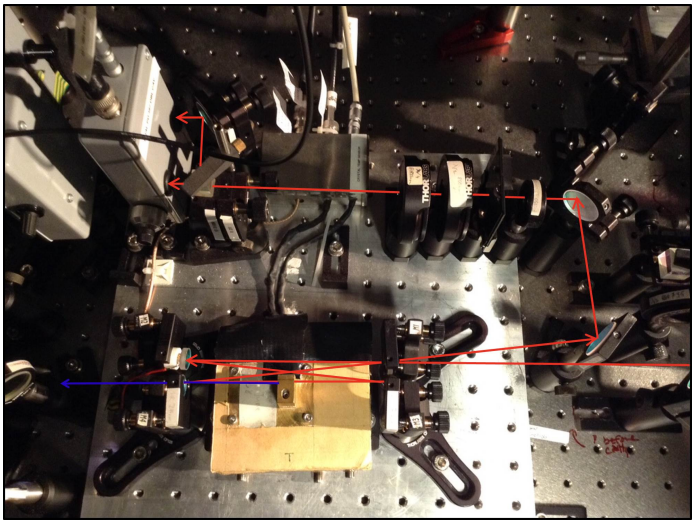

(b)

Figure 7.9: (a) A general view of the setup. Part of the TA Pro is visible on the right. As indicated on Fig. 7.7, the beam goes through an optical isolator and two modematching lenses before entering the cavity. Compared to the Fig. 7.7, an additional polarizing beamsplitter associated with a half-wave plate can be seen, and are used to further purify the input polarization of the beam. The cavity is placed inside a box of plexiglas in order to isolate it from acoustic vibrations and from heat flow. (b) Close-up of the cavity. The part of the setup used to stabilize the length of the cavity and composed of a half- and quarter-wave plates, a polarizing beamsplitter and a detection stage calculating the difference of the input signals can be seen. Here too, additional elements have been inserted as compared to Fig. 7.7: a neutral density (dark plate), and a lense which is used to focus the beam on the detector. The red and blue arrows indicate, respectively, beam paths for the fundamental (794 nm) and frequency doubled (397 nm) light fields.

We get η by inverting the previous equality :

$$\eta = \frac{R - R'}{R_0 - R'} \tag{7.23}$$

Our lack of knowledge of the losses inside the crystal and through the mirrors prevents us from plugging a numerical value for R_0 in the above formula and directly solving for η. Fortunately, there exists a possible work around, which consists in measuring the enhancement factor, and comparing the value for η we can get from these two measurements. The theoretical enhancement factor indeed reads :

$$P_{cav}/P_{in} = \frac{4T_1}{(T_1 + T_2 + \mathcal{L})^2} \tag{7.24}$$

which depends on $\mathcal{L}$, while the measured enhancement factor reads $P_{cav}/(P_{in} + P'_{in})$. Taking the ratio of these two quantities gives precisely η. The procedure to find $\mathcal{L}$ then goes as follows :

- first, measure the reflection from the cavity and the ratio of the intracavity power over the incident power. The latter can be simply estimated by measuring the power of the transmitted field after the cavity and dividing it by the transmission coefficient of the output coupler T_2.

- Choose a value for $\mathcal{L}$ to plug into the formulas for R_0 and the enhancement factor. The measurements on the crystal, though not very precise, gives a value of about 1%, so it seems reasonable to take this as a starting point.

- Vary $\mathcal{L}$ until the two $\eta's$ coincide.

Performing these measurements amounts to measuring the intracavity power, while the temperature of the crystal is set far away from the optimal temperature for phase-matching. The expression for the intracavity power (7.24) also needs to be slightly changed to take into account the non-perfect coupling to the cavity :

$$P_{cav}/P_{in} = \eta \frac{4T_1}{(T_1 + T_2 + \mathcal{L})^2} \tag{7.25}$$

where we just multiplied the numerator by η.

The reflection coefficient has been measured to be $(67.5 \pm 2.5)\%$ and the enhancement factor can be found from the measurement presented Fig. 7.10 to be 29.0 ± 1.3, which gives, following the procedure described above, a value of $(1.1 \pm 0.1)\%$ for $\mathcal{L}$ and about $(80 \pm 5)\%$ for η.

7.2.2.2 The finesse

A way to cross check the previous result is to measure the finesse of the cavity. According to its definition, a basic way to measure it could be to look at the signal obtained when the cavity is scanned across more than 1 FSR, and to measure the ratio of the distance between the two peaks over the width of one pic. Unfortunately, the response of the piezoelectric element to a voltage ramp is nonlinear, i.e. the

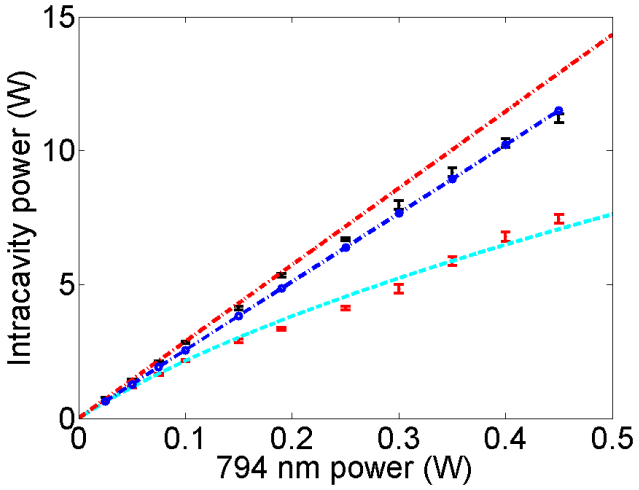

Figure 7.10: Black dots with error bars: Intracavity power in the cavity versus incident power without generation of UV light. Red dotted dashed line : fit to the first four measured data points using the expression (7.25). The free parameters are η and $\mathcal{L}$. Blue dashed dotted line : numerical calculation, using as input parameters for η and $\mathcal{L}$ the values deduced from the analysis of the whole data, including UV generated power (see text for more details). Red dots with error bars: Intracavity power versus incident power, at phase matching. Cyan dotted dashed curve: fit to the first four measured data points. The free parameter is the single-pass conversion coefficient which is found to be $(0.50 \pm 0.03)\%W^{-1}$

width of and distance between the peaks is different for different ramp voltages. To overcome this difficulty, we decided to use a different strategy to measure the finesse: the FSR can be known from the distance between the mirrors, with an acceptable precision - 1 mm over a distance of 13.7 cm, so better than 1% - while the width can be accessed through a time versus frequency calibration of the reading on the oscilloscope. To perform this calibration, we first lock the laser's frequency, and use an Acousto-Optic Modulator (AOM) to shift the laser's frequency by 19.2 MHz. We then measure on the oscilloscope the corresponding shift in time. The signal recorded on the oscilloscope is subject to important fluctuations due to acoustic vibrations, and to a slow drift which probably is a signature of the cavity drifting with time. Repeating the measurements 50 times allows to reduce the uncertainty associated with the first source of error, and yields a value of about 13.1 MHz for the FWHM. From this, the finesse is calculated to be approximately 48.5. Using the formula $F = \frac{2\pi}{T_1+T_2+\mathcal{L}}$, we find the losses the be $\mathcal{L} = 2.6\%$, a value slightly higher than the one got from the previous measurements. However, we can state by considering the sources of errors mentioned above that this is not so surprising, as the observed drift rather acts as a systematic error in our measurement and tends to give an overestimation of the width of the resonance, which in turn will lower the measured finesse. A better way to go would be to modulate the frequency of the laser to produce sidebands in the transmitted signal or to perform ringdown spectroscopy, and hence make our time to frequency calibration more accurate.

7.2.3 SHG results

7.2.3.1 Nonlinear losses

When quasi-phase matching is met, the production of UV light adds an additional nonlinear source of loss for the cavity. This nonlinear loss depends on the intracavity power P_{cav} and the single-pass conversion coefficient γ. This can be accounted for by replacing $\mathcal{L} \to \mathcal{L}+\gamma P_{cav}$ in the expression for the intracavity power (7.24). From this we find an expression for the ratio for the intracavity power the incident power P_{in}. On resonance, this ratio reads :

$$P_{cav}/P_{in} = \frac{4T_1\eta}{(T_1+T_2+\mathcal{L}+\gamma P_{cav})^2} \tag{7.26}$$

As already mentioned, the coefficient γ is on the order of a percent or less. We can thus neglect terms of second order in γ and rewrite (7.26) as :

$$P_{cav} = \frac{-(\mathcal{L}+T_1)^2 + \sqrt{((\mathcal{L}+T_1)^4 + 32(\mathcal{L}+T_1)T_1\gamma\eta P_{in})}}{4(\mathcal{L}+T_1)\gamma} \tag{7.27}$$

7.2.3.2 Generation of second harmonic

We performed measurements of the second harmonic power generated by choosing a waist of about 35 μm, but due to the observed instability of the output UV power

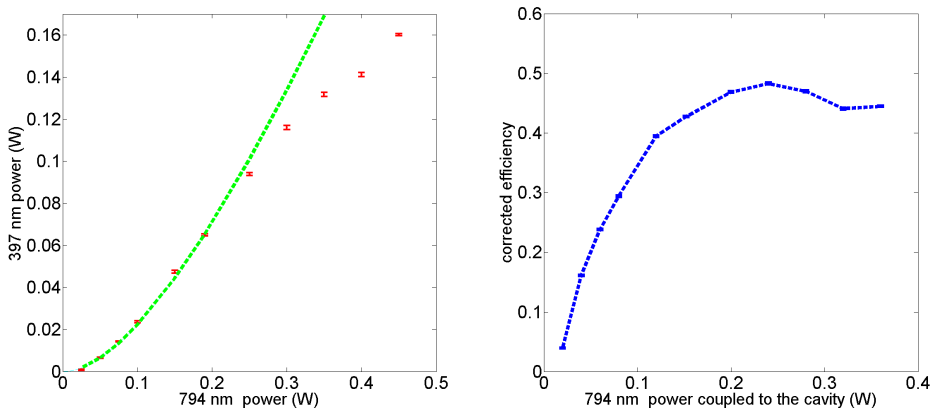

(a) (b)

Figure 7.11: (a) Red dots with error bars: UV power versus incident power Cyan dotted-dashed curve: fit of the first four measured data points. The free parameter is again the single-pass conversion coefficient, which is found to be $(0.48\pm0.05)\%W^{-1}$. (b) SHG efficiency corrected for imperfect coupling to the cavity, and non-unity transmission of cavity's output coupler at 397 nm. For an input power of 190 mW, the effectively coupled power is 152 mW, and the efficiency is 43%. This point correspond to optimal input power with respect to both the efficiency and the output's stability.

at high pump power - which we assumed to be the consequence of thermal effects - we decided to go to a looser focusing configuration and chose a waist of about 50 μm. Because this corresponds to the current configuration, and to avoid redundancy in the presentation, I choose to present only the measurements corresponding to the latter configuration.
The measurements of the intracavity power in the cavity during the SHG process, and the amount of UV light produced versus the power injected power are plotted on Fig. 7.10 and 7.11(a). A fit of these measurements yields of value for η in both cases of about $0.5\%W^{-1}$ with a fractional uncertainty of about 10%, which shows consistency between these two sets of data. The decrease of the intracavity power at higher incident power might be interpreted as a consequence of a process known as Blue Induced Infrared Absorption (BLIIRA) [106] which has been observed with similar SHG setups and wavelengths [107, 108].
The nonlinear response of the crystal can be further checked by plotting the UV power with respect to the temperature of the crystal and the efficiency $P_{2\omega}/P_{\omega}$. In the first case, we expect the output power to follow the behaviour explicited in section 7.1.1 eq. (7.5). The results are plotted in Fig. 7.12, and show relatively nice agreement with the theory. The efficiency is plotted Fig. 7.11(b), and is corrected for the imperfect modematching to the cavity, as well as non-unity transmission of the cavity's output coupler for UV light. The result is comparable to what can be found in the literature [107, 108].

Finally, we checked for the output's stability over time. This last measurement is in practice one of the most important, as it tells us about the possibility of producing usable UV light for experiments. The result can be seen Fig. 7.13, where it is apparent that working at higher power induces unavoidable thermal effects which result in a slight decrease of the output power over time. However, the instability is on the order of a couple of mW per hour over a nominal output power of 63mW, and full power can moreover be recovered by slightly decreasing the temperature of the crystal and/or moving the crystal a little bit.

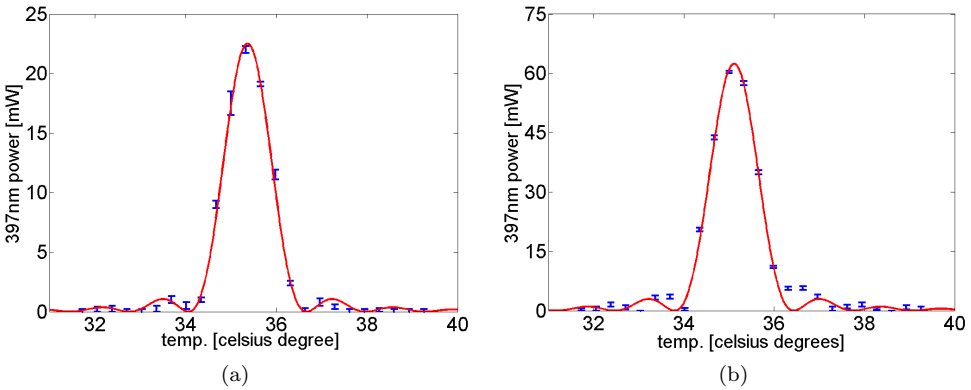

(a) (b)

Figure 7.12: a) UV power versus temperature for an incident power of 100mW. b) UV power versus temperature for an incident power of 190mW.

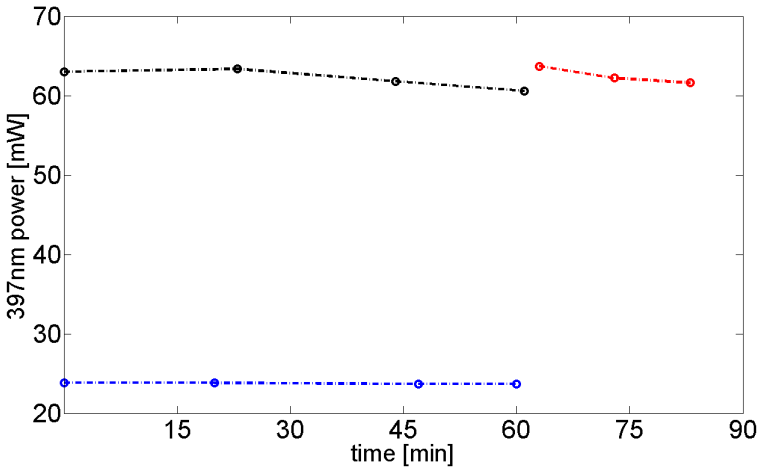

Figure 7.13: Blue dotted line : UV power versus time for an incident power of 100mW. Black and Red dotted lines : UV power versus time for an incident power of 190mW. The output power decreases slightly over time, but full power can be recovered by tuning the crystal and/or decreasing the temperature a little bit. This is indicated by the change of color. Uncertainties are smaller than the circles.

7.3 Stabilization of the laser frequency

To allow for efficient cooling and probing of the Ca^+ ions, the UV light source needs to be stabilized in frequency, which we achieve by locking the tapered amplified laser to a temperature-stabilized reference cavity. Owing to the narrow linewidth of the reference cavity, and provided that the cavity is itself stabilized in temperature, it can be used as an etalon for the laser source, which makes it a natural tool to perform this frequency stabilization. In our case, the reference cavity has a FSR $\sim$ 600 MHz, and is made of a quartz tube about 25cm long, which is temperature stabilized via a PID-circuit that feeds back to a resistive wire wound around the tube and placed inside a vacuum tube also actively stabilized in temperature. [109].
The stabilization scheme is based on the Pound-Drever-Hall (PDH) method [110,111]. Unlike the Hänsch-Couillaud locking scheme, the PDH scheme does not make use of the change in polarization between the incoming and reflected signals, but rather utilizes the fact that the phase of the total reflected field with respect to the incident field is shifted from $-180°$ to $180°$ when the laser frequency is scanned over the cavity resonance. Generally, phase shifts can not be measured directly with devices such as photodiodes which only record the light intensity, but are rather accessed through the interferences one can generate between the signal of interest and a reference signal. In the case of the PDH locking scheme, changes in the phase of the reflected field will be detected by modulating it which will generate sidebands, and by having these sidebands interfering with the carrier - the central main frequency. To make this clearer, we start with a monochromatic incident field:

$$E_{inc} = E_0 e^{i\omega t} \tag{7.28}$$

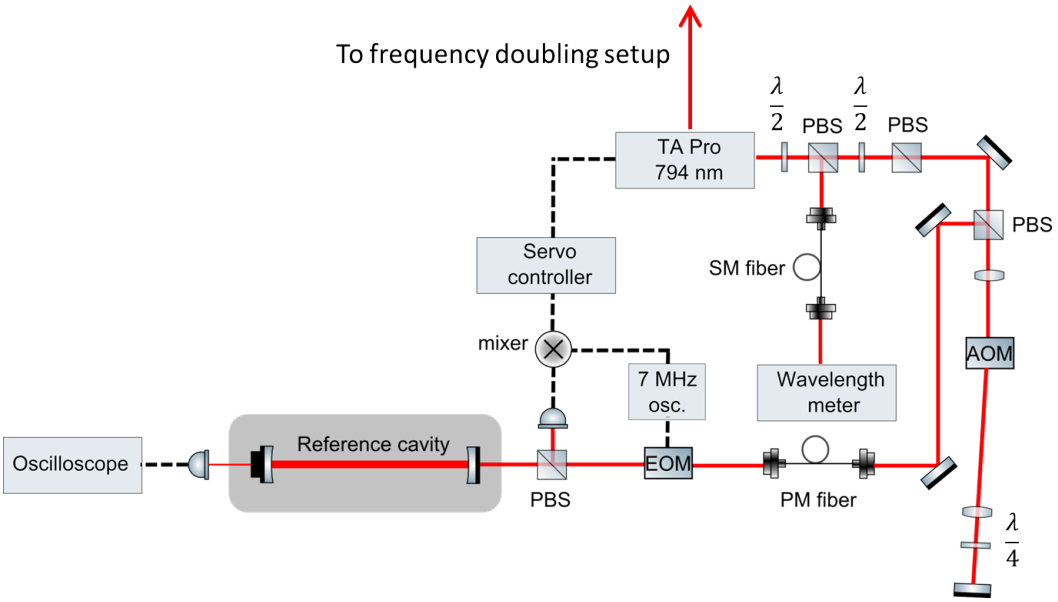

Figure 7.14: Schematic of the frequency stabilization setup. The low pass filter, and phase shifter have not been represented here, in practice they are included in, respectively, the servo control and the mixer.

The incident signal is sent through an Electro-Optic Modulator (EOM), which modulates the electric field, and generates sidebands in the transmitted signal from the cavity. The incident field impinging on the cavity input coupler thus reads:

$$E_{inc} = E_0 e^{i(\omega t + \beta \sin(\Omega t)} \tag{7.29}$$

In practice Ω is much smaller than ω and $\beta \ll 1$. We can then approximate (7.29) by expanding the exponential and be keeping only first order terms. Eq. (7.29) can then be rewritten as:

$$E_{inc} = E_0 e^{i\omega t}(1 + i\beta \sin(\Omega t) = E_0[e^{i\omega t} + \frac{\beta}{2}(e^{i(\omega+\Omega)t} - e^{i(\omega-\Omega)t})] \tag{7.30}$$

The reflection coefficient of the cavity is given by the ratio of the reflected to the incident field, and reads, in the case of a symmetric cavity:

$$F(\omega) = \frac{E_{refl}}{E_{inc}} = \frac{r\left(\exp\left(i\frac{\omega}{\delta\nu_{FSR}}\right) - 1\right)}{1 - r^2\left(\exp\left(i\frac{\omega}{\delta\nu_{FSR}}\right)\right)} \tag{7.31}$$

where $\delta\nu_{FSR}$ is the free spectral range of the cavity, and r the amplitude reflection coefficient of each mirror. In our case, the incident field contains three different frequencies, the carrier and two sidebands. The reflected field will then be given by:

$$E_{refl} = E_0[F(\omega)e^{i\omega t} + F(\omega+\Omega)\frac{\beta}{2}e^{i(\omega+\Omega)t} - F(\omega-\Omega)\frac{\beta}{2}e^{i(\omega-\Omega)t}] \tag{7.32}$$

We measure the intensity of the reflected field, i.e. a quantity proportional to $|E_{refl}|^2$. Applying this to (7.32) gives an intensity which is the sum of the three intensities corresponding to the carrier and sidebands intensities, plus additional cross-terms - the interference terms. Owing to the time varying character of the phase-shift - which is equal to $\pm\Omega t$ - these interference terms will oscillate at the modulation frequency Ω. This is different from the situation encountered when looking at interferences generated in a Michelson or Fabry Perot interferometer, where the phase shift corresponds to a difference in optical path lengths, and is constant. To measure signals which are $\propto (F(\omega)F^*(\omega+\Omega) - F^*(\omega)F(\omega-\Omega)\cos(\Omega t)$ or $\propto (F(\omega)F^*(\omega+\Omega) - F^*(\omega)F(\omega-\Omega)\sin(\Omega t)$ we need to multiply the signal by $\cos(\Omega t)$ or $\sin(\Omega t)$ respectively, to produce a signal which is a sum of a constant and a time varying - at 2Ω - signals, and then filter out the time varying signal.
The setup is sketched Fig. 7.14. Fine tuning of the laser's frequency is made possible by sending the beam through an Acousto Optic Modulator (AOM) in a double pass configuration, before sending it to the reference cavity. In such a configuration, the 1^{st}-order diffraction is reflected back through the AOM with its polarization rotated by 90° , and the 1^{st}-order diffraction of the second pass spatially overlaps the incident beam. Deflection due to tuning of the frequency of the AOM can therefore be avoided. Finally, a half-wave plate ($\frac{\lambda}{2}$) and a Polarizing Beam Splitter (PBS) are positioned immediately after the laser output to pick off part of the light to a wavelength-meter. Modulation of the field at 7MHz is performed by using a mixer - which also filters out the non-d.c. part of the error signal and allows for the correction of the phase delay, while the servo-controller performs the PID stabilization. The whole stabilization scheme requires power in the incident light beam lower than a μW, but for monitoring purposes $\sim$30 μW are typically sent to the cavity. The stabilizing signal from the servo-controller is sent back on the AC and DC current modulation inputs on the rear facet of the laser. Finally, the remaining short-term fluctuations result are typically of the order of $\sim$ 100 kHz, while the reference cavity typically slow drift is $\sim$ 1 MHz per hour.

7.4 Conclusion

In this chapter we have presented a frequency-doubled source for Doppler-cooling of Ca^+ ions. The second harmonic generation process is realized with a non linear ppKTP crystal placed in a bow-tie cavity.
We have presented a characterization of the relevant crystal properties, and observed a non-uniform as well as generally low value of the single-pass conversion coefficient γ ranging from 0.5 $\%W^{-1}$ to 0.7 $\%W^{-1}$, compared to the expected value derived from the Boyd-Kleinman theory ($\gamma \sim 1\%$) for a beamwaist of 35 μm. We have checked that the low value does not stem from the deviation of the laser beam from a pure TEM_{00} mode, and attribute the non-uniformity to defects in the crystal's volume due to inhomogeneous poling. By placing the crystal inside an optical cavity of finesse $\sim$ 48 and corresponding enhancement factor $P_{cav}/P_{in} \sim 30$ about 60 mW of frequency-doubled light can be stably generated with this setup, with an input power of 190 mW of light at the fundamental frequency, and a beam waist inside the crystal of 50 μm, corresponding to an efficiency of 43 % when taking into account the imperfect modematching of the laser beam to the cavity. Instabilities in the generated output

and deviations from the law $P_{2\omega} = \gamma P_{\omega}^2$ at high values of P_ω are attributed to thermal effects in the crystal, due to its high absorption at 397 nm, and possibly to an effect known as Blue Induced Infrared Absorption. Finally, the setup is frequency stabilized using a Pound Drever Hall setup, which results in short term fluctuations of ~ 100 kHz, and a typical slow drift of ~ 1 MHz per hour.

Chapter 8

Experimental setup

8.1 Cavity Trap

The linear Paul trap is described in the next section, while the optical cavity is the subject of section 8.1.2.

8.1.1 The linear Paul trap

The ion trap is a segmented linear trap formed by four rods each divided in three electrodes, see fig. 6.1. A mathematical description of the confinement was given in chapter 2. The trap electrodes have a radius $r_e = 2.6$ mm, and the inter-electrode distance is $2r_0 = 4.7$ mm. The end- and center electrodes length are, respectively $z_e = 5.9$ mm and $2z_0 = 5.0$ mm. The trap is operated with a RF field of frequency $\Omega_{rf} = 2\pi \times 4$ MHz. The axial confinement is achieved by applying a static electric DC potential of 2V on the end-electrodes. With this geometry, the a, q parameters defined in eq. (2.4) are $a = -0.84 \times 10^{-3} V^{-1} \times U_{DC}$ and $q = 1.38 \times 10^{-3} V^{-1} \times U_{rf}$, the axial geometric constant in eq. (2.2) $\eta = 0.342$. The electrodes are made of copper, coated with a thin layer of gold, mounted on ultra low expansion glass rods [1]. The whole structure is held together by a monolithic ceramic mount. For more details on the trap structure, design and assembly, see [53].
The RF trap voltages are produced by a frequency generator and amplified before being transferred to he electrodes through a resonant circuit. A homemade voltage driver is used to supply DC voltages to the electrodes and allows for varying the axial potential by changing the voltage applied on the end-electrodes at the same time, while making it also possible to alter the DC potentials of each individual electrode segment separately. The DC potential minimum can thus be shifted both radially and axially, and the ions positioned at will. The trap acts as the capacitive part of an LRC-circuit itself coupled inductively to the RF-power supply. Variable external capacitors allow for tuning the phases of the different RF-chains and the voltage on individual electrodes. This is crucial for overlapping the trap center with the cavity axis (see 8.1.3) and can be used for minimizing the excess micromotion.

[1] made of Zerodur®, manufactured by Schott

8.1.2 The optical cavity

A sketch of the optical cavity integrated into the trap is shown in fig. 8.1. The optical cavity is made of two mirrors with a diameter of 1.2 mm and a radius of curvature of 10 mm. The mirrors are mounted in a nearly confocal geometry with a spacing of $L = 11.8$ mm and the cavity axis is parallel to the symmetry axis of the linear Paul trap. They are made of fused silica and their presence could in principle cause the RF-lines to bend, hence introducing excess micromotion which would in turn broaden the atomic transition through the Doppler-effect. A way to minimize this effect is to add dielectric mirror coats which extend almost all the way to the electrodes [86]. These coats have a diameter of 4.16 mm, slightly smaller than the inter-electrode distance. The cavity mirrors are coated for 866 nm and 894 nm with one mirror being a high reflector (HR) and the other a partial transmitter (PT), with transmittances of 5 ppm and 1500 ppm at 866 nm, respectively. Two titanium plates hold the cavity together: the HR mirror is fixed on one plate, while the PT mirror is mounted on a PZT-plate allowing for control of the cavity length. The choice of optical frequency-bands in the coatings follows from the requirement to have a high finesse at the wavelengh of 866 nm corresponding to the $3d^2D_{3/2}$ to $4p^2P_{1/2}$ transition in $^{40}Ca^+$ and at the same time resonant a high finesse at 894 nm with the purpose to lock it. The cavity has a free spectral range of $\nu_{FSR} = 12.7$ GHz and the cavity mode waist size equals 37 μm at 866 nm. The cavity decay rate at 866 nm is $\kappa = 2\pi \times (2.1 \pm 0.1)$ MHz giving a finesse $\mathcal{F} = 3000 \pm 200$ whereas the finesse at 894 nm is about 2000. In principle, up to 98% coupling into the fundamental TEM_{00} can be achieved [53], and we typically achieve a coupling of $> 95\%$.

8.1.3 Overlapping the cavity and trap axis

Manufacturing of the trap resulted in offset between cavity and trapis axis of about 80 μm [53]. Nevertheless precise ($\sim 1\mu$m) overlapping of both axis is a requirement for experiments involving an ion or a string of ions coupled with a cavity mode of a few 10μm, since minimization of the excess micromotion as well as maximization of the ion-cavity field coupling need to be fulfilled simultaneously. However, such alignment cannot be done by simply adding DC offsets on the electrodes, as this would simply move the ions to a zone of non-zero micromotion. As mentioned in section 8.1.1, external variable capacitors can be used to fine-tune the voltage on each electrode

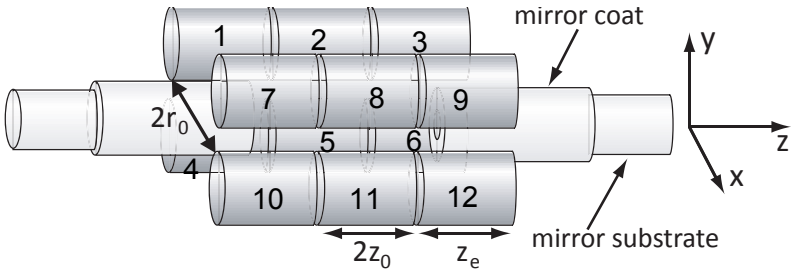

Figure 8.1: Sketch of the linear Paul trap with integrated mirrors.

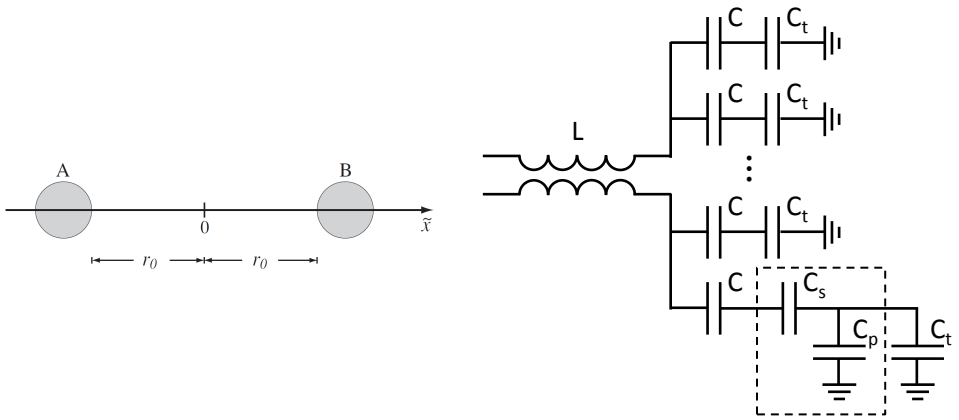

Figure 8.2: (a) Two electrodes model used in the derivation of the location of the shifted potential minimum (b):Schematic of the RF resonant circuit. Each electrode is represented by a capacitance C_t, and is connected to RF power supply through a toroidal transformer of inductance L. Displacement of the RF-potential nodal line can be achieved by adding series and parallel capacitances C_s and C_p (dashed box).

and thereby lead to the desired displacement of the nodal line. Since this is described in details in [53, 112], we will only recall the main ideas here.

8.1.3.1 Attenuating the voltage on electrodes on one side leads to a displacement of minimum of the RF potential

In a simple model used in [112], the authors consider two electrodes A and B separated by a distance $2r_0$ (see fig. 8.2(a)), with RF amplitudes of respectively U^A_{RF} and U^B_{RF} which differ by a small attenuation factor $\delta < 1$ such that $U^B_{RF} = \delta U^A_{RF}$. At $\tilde{x}$, the total potential $U(\tilde{x})$ is equal to:

$$U(\tilde{x}) = \frac{U^B_{RF}}{r_0 - \tilde{x}} + \frac{U^A_{RF}}{r_0 + \tilde{x}} \tag{8.1}$$

and its minimum therefore lies exactly in the middle of the two electrodes in the case $\delta = 1$. In the case $\delta \lesssim 1$, it can be shown that the potential minimum is shifted towards the electrode carrying the attenuated voltage by a quantity $(1 - \delta)r_0$, and the potential remains approximately harmonic.

8.1.3.2 Attenuation of the voltages can be done by adding series and parallel capacitances to the trap electrodes

We consider the schematic depicted in fig. 8.2(b). The capacitances C_t represent the trap electrodes, which act as the capacitive part of a LRC circuit which inductance L is mainly set by the transformer. Denoting U_{in} the input voltage, the voltage on

an electrode is given by:

$$U_e = \frac{U_{in}}{1 + \frac{C_t}{C}} \tag{8.2}$$

without any additional capacitances. The circuit then acts as a voltage divider, and the voltage on the electrode can be attenuated by increasing the capacitance C_t, which in practice can be realized by adding series and parallel capacitances, denoted C_s and C_p on fig. 8.2(b). Considering the schematic of fig. 8.1, the potential minimum can be shifted along the x direction by attenuating voltages on electrodes (7-8-9-10-11-12) by the same amount, while leaving the others unchanged.

In addition to the positioning of ions, having additional variable capacitances parallel to the electrode capacitance can also be useful in order to compensate for any asymmetry in the electrode impedances. Such asymmetries would cause the apparition of unwanted phase shifts between the electric fields produced by different electrodes, which could lead to, e.g. presence of residual micromotion along the trap axis [79]. An example of compensation of micromotion is shown in [64].

8.2 The vacuum chamber

The cavity trap setup is placed inside a vacuum chamber with a diameter of 40 cm, pumped to a pressure of a few 10^{-10} mbar. Outside the vacuum chamber, 2 pairs of Helmholtz coils produce magnetic fields in the $x-$ and $y-$ directions in order to compensate the Earth magnetic field, and a third pair is used for producing the bias magnetic field in the z direction already mentioned in section 4.2, and which creates a well-defined quantization axis parallel to the trap axis. This is necessary in order to efficiently repump the ions during Doppler cooling and to optically pump the ions into specific Zeeman substates of the $3d^2D_{3/2}$ state. The vacuum chamber possesses six view ports, anti-reflexion coated at the appropriate wavelengths, through which the lasers described above are sent to the trap (see fig. 8.3)

8.3 Laser systems

In this section the laser sources used in our experiments are described. A global schematic of the laser sources is depicted in fig. 8.4.

8.3.1 Isotope selective loading laser - 272

The calcium ions are loaded from an effusive oven. The calcium source contains all stable isotopes, the most abundant of which being ^{40}Ca, with a fraction of 96.9%, and is the one used in the experiments. Nevertheless, different stable isotopes can be selectively loaded [53, 113], which makes possible to trap two-components crystals [114, 115].
The oven is usually heated to $\sim 380\,^{\circ}$C, and the emerging thermal beam is collimated by a set of skimmers and set through the center of the trap at a 45° angle relative to the trap axis. There it is crossed perpendicularly by an ionization laser beam at 272 nm which allows for the isotope selective loading of the calcium ions, through a

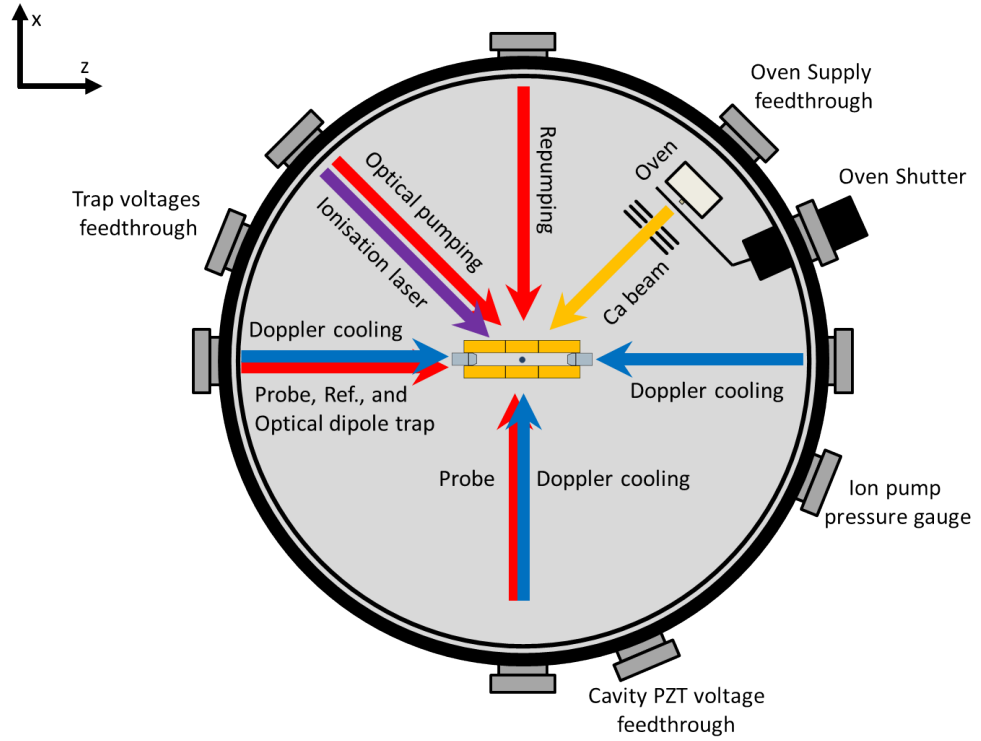

Figure 8.3: Schematic of the vacuum chamber, with the cavity-trap (center), the main laser beams and their direction relative to the trap.

resonantly enhanced two-photon ionization process. In this process, a calcium atom is first resonantly excited to $4s5p^1P_1$ and subsequently transferred to the ionization continuum, either directly from the $4s5p^1P_1$ state, or can be driven, after spontaneous decay, from the $4s3d^1D_2$ state to the ionization continuum by a non-resonant second photon at the same wavelength [116], see fig. 8.5. The isotope selectivity originates from the first resonant transition, which for ^{40}Ca is separated from the next closest isotope ^{42}Ca by ~ 1 GHz [117].

Light at 272 nm is produced from a 1088 nm ytterbium-doped germanosilicate glass distributed-feedback (DFB) fiber laser[2] frequency-quadrupled in two consecutive SHG stages. The fiber laser is tunable over several GHz, making it possible to ionize any of the stable isotopes by tuning the frequency of the 272 nm source to resonance with the $4s^{21}S_0$ to $4s5p^1P_1$ transition, and its frequency is locked to the commercial wavelength meter mentioned above. During loading both Doppler cooling and repumping laser are on [113]. After loading the desired number of ions, the ionizing beam is blocked and the calcium oven closed.

[2]Koheras Boostik

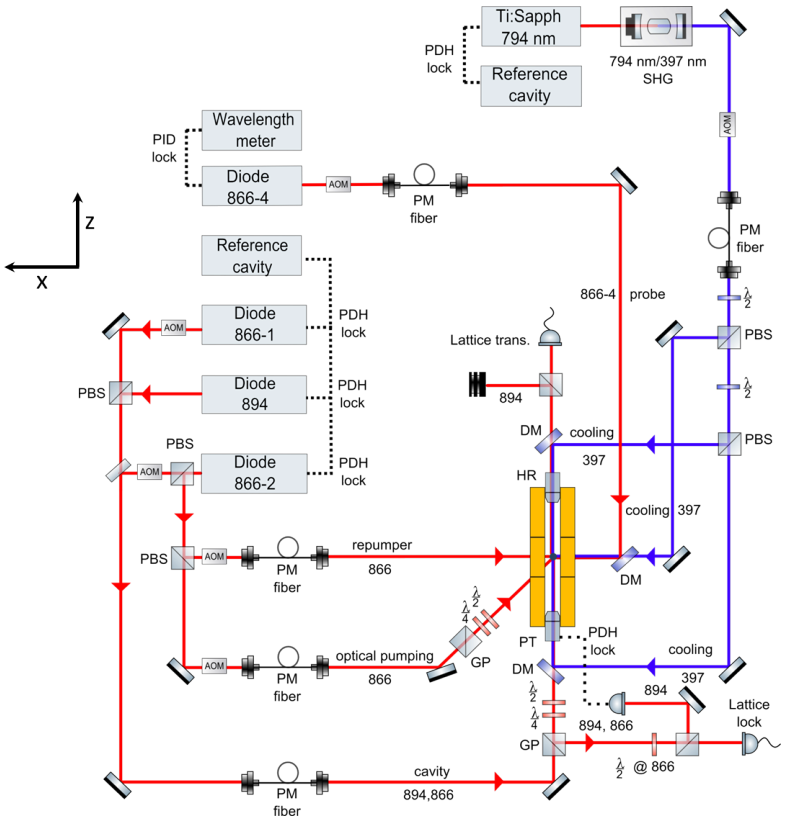

Figure 8.4: Overview of the laser sources used in the experiments. List of abbreviations : PDH: Pound-Drever-Hall, PID: proportional-integral-derivative, PBS: polarizing beam splitter, PM fiber: polarization maintaining fiber, DM: dichroic mirror, GP: glan polarizer, AOM: acousto-optic modulator

8.3.2 Doppler cooling laser- 397

A laser source at 397 nm is used to Doppler cool the trapped ions by driving the $4s^2S_{1/2} \leftrightarrow 4p^2P_{1/2}$ transition. In order to generate light at 397 nm, a Verdi V8 laser generating 5.5W of light at 532 nm pumps a Coherent Ti:Sapph laser producing typically $\sim$ 200 mW of 794 nm light which is subsequently frequency doubled through a SHG process using a bow-tie ring cavity similar as the one described above, although using in this case a type I critical phasematching in a LBO crystal. Part of the 794 nm light is taken out and sent to a temperature stabilized reference cavity to which the Ti:Sapph laser is locked with a PDH scheme. The reference cavity is made of two mirrors on a 25 cm long quartz tube mounted inside a vacuum tube, has a FSR of $\sim$ 600 MHz, as described in section 7.3. For more details on this specific part of the setup, the reader is referred to [109]. Fine tuning of the laser frequency is done using an AOM in double pass configuration allowing for the tuning of the laser by $\pm$ 100 MHz, corresponding to a tuning range of $\pm$ 200 MHz for the frequency doubled light at 397 nm. When locked to the reference cavity, the laser linewidth is $\sim$ 100 kHz,

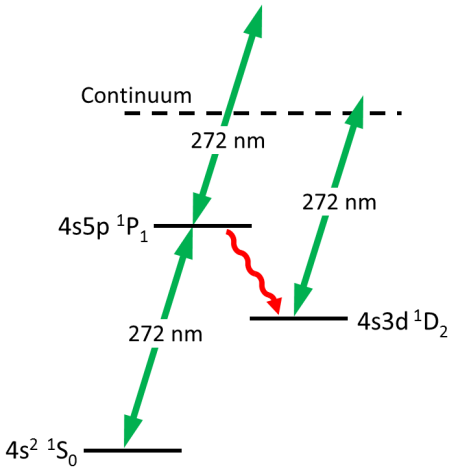

Figure 8.5: Isotope selective two-photon ionization scheme. The lifetime of the $4s5p\,^1P_1$ and $4s3d\,^1D_2$ states are 17-60 ns and 18 ms, respectively.

and much narrower than the natural linewidth of the $4s^2S_{1/2} \leftrightarrow 4p^2P_{1/2}$ transition in $^{40}Ca^+$ which is $\Gamma = 2\pi \times 22.4$ MHz. The frequency doubled light is sent through a second AOM in single-pass and the -1^{st} diffraction order is coupled to a fiber guiding the light to the trap table. This AOM is used to switch the Doppler cooling light on and off, with typical rise times of $\sim$ 100 ns and on-off attenuation $>$ 55 dB after fiber. On the trap table the light beam is split in three beams: two of them, equally intense, are sent in counter propagating directions along the trap axis, with opposite circular polarizations σ^+/σ^-, and the third, linearly polarized along the y-axis is sent perpendicular to the trap axis. The balance of axial to side cooling can be adjusted in order to optimize the cooling of single ions, strings of ions as well as large 3D Coulomb crystals.

8.3.3 Repumping, optical pumping, and cavity probe lasers - 866-2

As mentioned in 4.2, the ions need to be repumped the $3d^2D_{3/2}$ to the the $4p^2P_{1/2}$ states in order to perform Doppler-cooling. In addition, another source resonant with the $3d^2D_{3/2}$ to $4p^2P_{1/2}$ transition is needed to optically pump the population into specific Zeeman substates of the $3d^2D_{3/2}$ state for the purpose of localization experiments described in the last part of the thesis. In order to perform these tasks, we use a home-built external cavity diode laser system in Littrow configuration [118–120] which emits light at 866 nm. Active stabilization of frequency of this laser is achieved by sending light through an AOM in a double-pass configuration with a tuning range of $\sim$ 100 MHz to another, albeit similar reference cavity than the one described above. The diode laser output is split into three beams: two of them are used to repump and optically pump the ions, while the third one is used as a probe of the same transition. Both repumper and optically pumping beams are sent through AOMs in single-pass,

and -1st order coupled to a fiber resulting as before in extinction ratio $>$ 55 dB after the fiber. The repumper is sent to the trap along the x-direction, with a polarization parallel to the y-axis, which corresponds to a superposition of σ^+ and σ^- light. In this way all four Zeeman sub-states are addressed and repumped during the cooling cycle. Optical pumping is achieved by sending he 866-2 beam to the trap at 45° with respect to the z-quantization axis. Polarization after the fiber controlled by a Glan polarizer and successively a $\lambda/4$ and $\lambda/2$ wave plate adjusted in order to only drive π and σ^+ transitions between $3D_{3/2}$ and $4P_{1/2}$ [53], so as to accumulate ions in the $m_J = +3/2$ Zeeman substate of the $D_{3/2}$ state.
Finally, the part of the 866-2 diode laser output used to probe the $3d^2D_{3/2}$ to $4p^2P_{1/2}$ transition is overlapped with 894 and sent through same single-mode, polarization-maintaining fiber to the trap table. This source was used in the past in experiments probing localization using a different scheme which we will explain in greater details in the last section. In our experiments, it is used only to adjust the cavity length such that it is resonant with the $3d^2D_{3/2} \leftrightarrow 4p^2P_{1/2}$ in the $^{40}Ca^+$ ion, as mentioned above.

8.3.4 Cavity reference laser - 894

A diode laser with a wavelength of 894 nm is used to lock the experimental cavity in experiments described in the last part of this thesis. This laser has the same design as 866-2 and locked to the same reference cavity using the PDH technique. As with other lasers, its frequency can be tuned using a double-pass AOM before the reference cavity. It is overlapped with the 866-1 laser and sent to the trap table through the same single-mode fiber. By monitoring the transmitted signal of this laser and comparing its position in a scan with the resonance of the probe laser (see next subsection), the cavity resonance frequency can be finely adjusted and locked to the atomic resonance frequency using PDH. The wavelength of 894 nm is not resonant with any of the transitions in the $^{40}Ca^+$, but despite its narrow-linewidth it still contains non-negligible amount of 866 photons that might drive the $3d^2D_{3/2} \leftrightarrow 4p^2P_{1/2}$ transition and is therefore spectrally filtered with a diffraction grating (1800 lines/mm).

8.3.5 Optical lattice laser - 866-1

A diode laser similar to 866-2 is used in experiments described in last chapter to generate the intracavity optical potential. In localization experiments, the laser is required to follow the cavity vibrations in order to minimize the intensity fluctuations of the optical potential, and is therefore locked to the experimental cavity itself via a PDH scheme, and not to the reference cavity. The laser field is circularly σ^- polarized, in order to address the Zeeman substate $m_j = +3/2$ of the $3D_{3/2}$ state, and is far-detuned from the atomic transition $3d^2D_{3/2} \leftrightarrow 4p^2P_{1/2}$ while at the same time being resonant with a mode of the experimental cavity.

8.3.6 Probing laser - 866-4

A diode laser similar to the one introduced previously is used to near-resonantly probe the ion $3d^2D_{3/2} \leftrightarrow 4p^2P_{1/2}$ transition. The 866-4 laser source is frequency stabilized

through proportional-integral-derivative (PID) feedback to the PZT controlling the angle of the grating to a commercial wavelength meter[3]. The wavelength meter is referenced to a Helium-Neon (He-Ne) laser source, and is therefore not expected to show long term drifts in frequency. The short term frequency stabilization corresponds to fluctuations on the order of a few MHz. The 866-4 beam is sent through an AOM in single-pass, and -1^{st} diffraction order coupled to a fiber before being sent to the trap table. The AOM is used to shut the beam on and off, does so with a typical rise/fall-time of 18/55 ns respectively, and an extinction ratio of -50.6 dB. On the trap table, the beam is sent along the x-axis to the trap, with a linear polarization parallel to the y-axis, in order to drive σ^+ and σ^- transitions only.

[3]HighFinesse Angström WS-U2

Chapter 9

Imaging system and detection analysis

In this chapter we describe the equipment we use to detect and image the ions, and present the analysis we will later use to infer the most probable numbers of emitted photons from the detected signals, as well as the uncertainties on these measures.

9.1 Detection and imaging system

In all the experiments presented in this thesis the ions are detected by collecting the fluorescence they emit at 397 nm when they spontaneously decay from the $P_{1/2}$ to the $S_{1/2}$ state on a charge-coupled device (CCD) camera. The detection and imaging system has two purposes: when light is detected during the cooling cycle, it is used to take pictures of the ions, in order to characterize the quality of the cooling, the crystal shape, the positioning of the ions, and, as we will see in chapter 11, the light collected by the CCD camera can also be used to perform quantitative analysis of the scattering probability in localization experiments. On figure 9.1 a schematic of the detection apparatus is shown. It consists in an achromatic lens with a focal length of 70 mm placed above the trap chamber to collect the fluorescence light. The ions are imaged with a ~ 22 magnification onto an imaging intensifier which consists in a photocathode, from which electrons are emitted from the incident light, two micro-channel plates where the electron number is multiplied before producing an amplified picture of the ions on a phosphore screen. This picture is in turn imaged by a commercial objective on the CCD camera with magnification 1/2, resulting in an overall magnification of ~ 11. The CCD camera is 640×480 pixels resulting in a resolution of $\sim 0.85\mu$m per pixel [64]. Apart from the amplification, the acceleration voltage of the intensifier can be gated with well controlled time resolution as short as 20 ns, which will prove useful in the experiments described in the last part of this thesis where fast gating times are necessary.
The quantum efficiency of the detection system was measured in previous experiments, and found to be $\sim 10^{-4}$ [64]. This indicates that a large number of emitted photons is required in order to record a appreciable signal; since in typical experiments only a few number of photons (typically a few tens, see section 11.3) are detected, large fluctuations in the number of detected photons are to be expected. Therefore, using

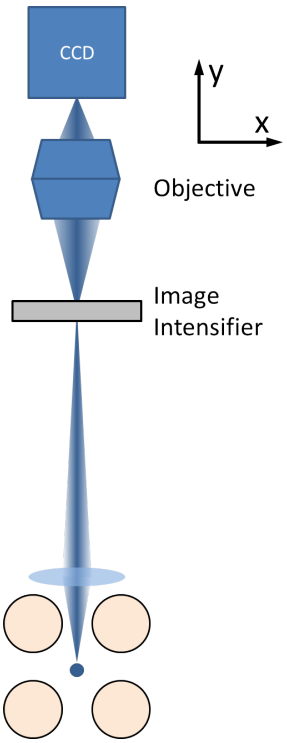

Figure 9.1: (a) Schematics of the imaging setup. A lens placed above the chamber (not represented on the drawing) collects the light emitted by the ions, and produce an image on the imaging intensifer. The imaging intensifier is itself imaged by the commercial objective on the charge-coupled device (CCD) camera, which is used to monitor the fluorescence and position of the ions.

this detection system in order to measure accurately the scattering probability of the ion imposes to quantify as well as possible the sources of uncertainty on the number of detected photons. This is the purpose of the next section.

9.2 Detection analysis

In order to quantify precisely the photon scattering probability given the recorded signal on the CCD camera, we build a model for the detection system taking into account its imperfections: non-unit probability that a photon reaches the imaging intensifier, non-uniqueness of the number of counts on the CCD camera following the detection of a single photon. To do so, we call P_{det} the probability that one photon reaches the imaging intensifier, N_p^D the number of detected photons on the imaging intensifier, N_c the number of counts on the CCD camera and N_p^E the number of emitted photons. With these notations, the probability to detect N_p^D photons given N_p^E emitted photons can be seen as the probability of having N_p^D "successes" in N_p^E trials, the probability of a success being given by P_{det}. It is therefore described by a

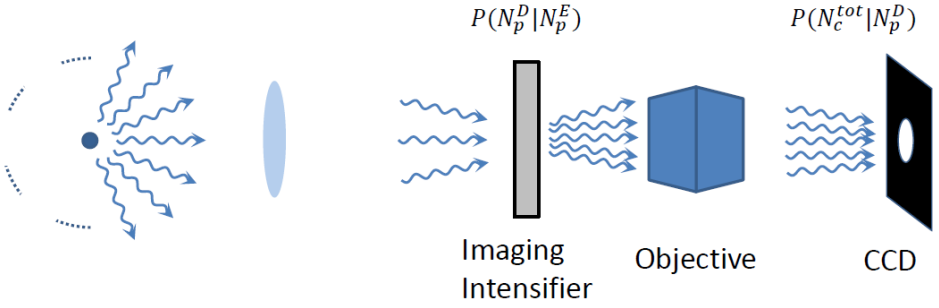

Figure 9.2: Graphical representation of the detection analysis. The ion scatters photons in every directions, and the probability for N_p^D photons to reach the imaging intensifier given that N_p^E photons are emitted is equal to $P(N_p^D|N_p^E)$. The signal is subsequently amplified and focused onto the CCD camera resulting in N_c^{tot} counts, with a probability distribution given by $P(N_p^D|N_c^{tot})$.

binomial distribution:

$$P(N_p^D|N_p^E) = \binom{N_p^E}{N_p^D} P_{det}^{N_p^D} \, (1 - P_{det})^{N_p^E - N_p^D} \tag{9.1}$$

Additionally, the probability $P(N_c|N_p^D = 1)$ that one detected photon leads to N_c counts on the CCD camera follows a distribution we assume to be well-described by a normal distribution, with a mean $\bar{N}_c$ and width σ_c:

$$P(N_c|N_p^D = 1) = \frac{1}{\sigma_c\sqrt{2\pi}} \exp - \frac{(N_c - \bar{N}_c)^2}{2\sigma_c^2} \tag{9.2}$$

from which we deduce the probability $P(N_c^{tot}|N_p^D)$ that N_p^D detected photons lead to N_c^{tot} counts on the CCD camera [121]:

$$P(N_c^{tot}|N_p^D) = \frac{1}{\sigma_c\sqrt{2N_p^D\pi}} \exp - \frac{(N_c^{tot} - N_p^D\bar{N}_c)^2}{2N_p^D\sigma_c^2} \tag{9.3}$$

Finally, we can compute the probability that N_p^E emitted photons result in N_c^{tot} counts on the CCD camera:

$$P(N_c^{tot}|N_p^E) = \sum_{N_p^D=1}^{\infty} P(N_c^{tot}|N_p^D) P(N_p^D|N_p^E) \tag{9.4}$$

$$= \sum_{N_p^D=1}^{\infty} \frac{1}{\sigma_c\sqrt{2N_p^D\pi}} \exp - \frac{(N_c^{tot} - N_p^D\bar{N}_c)^2}{2N_p^D\sigma_c^2} \binom{N_p^E}{N_p^D} P_{det}^{N_p^D} \, (1 - P_{det})^{N_p^E - N_p^D} \tag{9.5}$$

For the purpose described above, what we actually want is the probability $P(N_p^E|N_c^{tot})$ that N_p^E photons were emitted *given* N_c^{tot}. This probability is related to $P(N_c^{tot}|N_p^E)$ through:

$$P(N_p^E|N_c^{tot}) = \frac{P(N_c^{tot}|N_p^E)P(N_p^E)}{P(N_c^{tot})} \tag{9.6}$$

In a typical experiment, we measure N_c^{tot} and in this situation the event "detecting N_c^{tot}" is realized, therefore $P(N_c^{tot}) = 1$. On the other hand, the value of $P(N_p^E)$ is unknown, and we thus need another strategy to access $P(N_p^E|N_c^{tot})$. The strategy we choose amounts to "invert" the distribution $P(N_c^{tot}|N_p^E)$: we calculate $P(N_c^{tot}|N_p^E)$ for several values of N_p^E, and "reconstruct" a new probability distribution $P^{eff}(N_p^E|N_c^{tot})$ by selecting the $P(N_c^{tot}|N_p^E)$ corresponding to a fixed value of N_c^{tot}. By doing this, we assume that the highest value of this selection can be interpreted as "the most probable number of emitted photons given N_c^{tot} CCD counts". That we are allowed to do so is not obvious, and in the following we analyze the properties of both $P(N_c^{tot}|N_p^E)$ and $P^{eff}(N_p^E|N_c^{tot})$ in order to assess the consistency of such approach. To do this, we need to find the values of the parameters P_{det}, $\bar{N}_c$ and σ_c, which can be measured experimentally. In the next subsection, we show how we measure these parameters, and we will come back to the results of this analysis in the final section.

9.2.1 Measurement of P_{det}, $\bar{N}_c$ and σ_c

In order to determine $\bar{N}_c$ and σ_c, we need to access the distribution of CCD counts for one detected photon, and we also need as many detection events as possible in order to increase the statistics and hence the precision of our results. In order to do so, we set up an experimental sequence during which a photon is emitted with a probability close to one, and at the same time set the camera exposure such that approximately one photon is detected per image. One image thus consists of a large number of sequences, and the exposure is chosen in accordance with the timing of a sequence. Such a sequence is 30 μs long and consists in 20 μs of Doppler cooling using the 397nm and 866-2 repumper lasers, followed by 5 μs with the 397nm cooling laser alone in order to pump all the population in the $D_{3/2}$ state. All the lasers are then switched off for $\sim$ 4.7 μs, after which the imaging intensifier is switched on for 1.5 μs. During this window of 1.5 μs, the 866-4 nm probe laser is applied for 1 μs on the $3d^2D_{3/2}$ to $4p^2P_{1/2}$ transition, with a power of $\sim$800 μW. The duration of 4.7 μs between optical pumping and probing ensures that no residual charges present on the intensifier's photocathode and created during the cooling are present when imaging takes place. The power and gating time of the 866-4 probe laser are chosen such that the transition is over-saturated, in order to scatter one photon on the 397nm with a near unit probability[1]. Upon emission of a 397nm photon, the ion decays to the $4s^2S_{1/2}$ state and therefore does not take part in the process anymore. In this situation at most one photon is emitted during each sequence. From a previous estimation of the detection efficiency described in [64] we can infer that setting the exposure of the CCD camera to 200 ms should result in an average number of detected photons slightly higher than one per image.

[1]The fact that with these values of power and gating time a photon at 397 nm is scattered with near-unit probability will be justified in the last part of the thesis

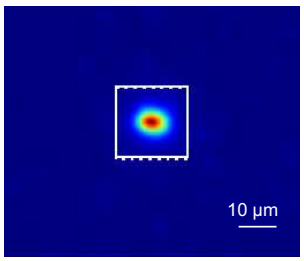

Figure 9.3: Typical image of a single ion from which we obtain the scattering signal used for the measurement of $P(N_c|N_p^D = 1)$, and P_{det}.

An example of such image is shown on figure 9.3. To process the signal we start by defining a box centered on the ion of $\sim 20 \times 20$ pixels (thus corresponding to $\sim 17\mu$m $\times 17\mu$m and shown as the white square on the figure 9.3). The integrated signal inside the box is calculated by summing the signal of each pixel, and the average background signal subtracted to it. The resulting number is saved, and the procedure repeated for a total of 9015 images. Using this data, we draw an histogram of the number of CCD counts per image, which is shown on figure 9.4. The histogram is fitted with a triple-normal distribution, in order to take into account events corresponding to 1, 2 and 3 detected photons and from which we get $\bar{N}_c$ and σ_c, which are in our case respectively equal to (2135 ± 17) and (907 ± 14). In order to calculate P_{det} from

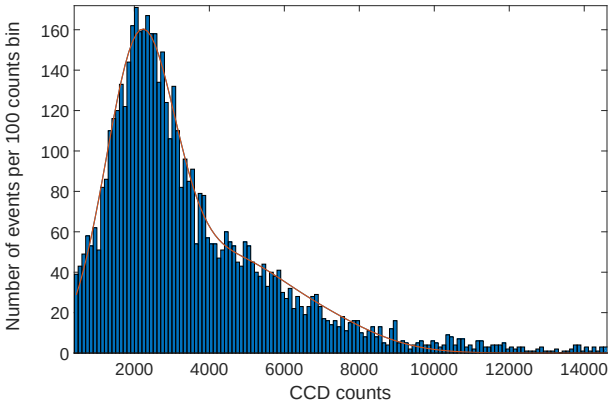

Figure 9.4: Distribution of the number of CCD counts per 200 ms image versus the number of CCD counts. In this figure, the bin size is 100 counts.

the above measurements, we calculate the mean number of detected photons during the whole experiment consisting of all 9015 images, and compare it to the number of emitted photons. The mean number of detected photons can be obtained by dividing the sum of the CCD counts over all images by the mean number of CCD counts per detected photon obtained from the previous analysis, and is found to be ~ 9750. There are 6600 emitted photons per image of 200 ms, and hence the grand total

number of emitted photons for the 9015 images is equal to $6600 \times 9015 \approx 6 \times 10^6$. Finally, we find $P_{det} = (1.67 \pm 0.01) \times 10^{-4}$. We will now discuss what should be expected according to the analysis made above.

9.2.2 Results and discussion

In order to analyze in detail the properties of $P^{eff}(N_p^E|N_c^{tot})$, we will proceed by steps, and start by examining the behavior of the probability distribution $P(N_c^{tot}|N_p^E)$ in three cases: for mean numbers of detected photons $\bar{N}_p^D \gg 1$ (first case), $\bar{N}_p^D < 1$ (second case), and finally for $\bar{N}_p^D \sim 1$ (third case). For each of these distributions, we will determine the most probable number of CCD counts $N_c^{tot,max}$. We will then turn the problem around, and, as mentioned above, we will "build" the probability distribution $P^{eff}(N_p^E|N_c^{tot,max})$ by plotting $P(N_c^{tot,max}|N_p^E)$, for varying N_p^E, and find the maximum and width of this distribution. We will be able to compare:

1. the number of emitted photons that leads to $N_c^{tot,max}$ in the first case
2. the most probable number of emitted photons given $N_c^{tot,max}$ determined with the newly constructed distribution

We will see that these number differ, and try to provide an explanation for it. By doing so, we will get a deeper understanding of the detection mechanism, and as announced in the beginning, we will be able to assess the consistency of the effective probability distribution $P^{eff}(N_p^E|N_c^{tot})$.

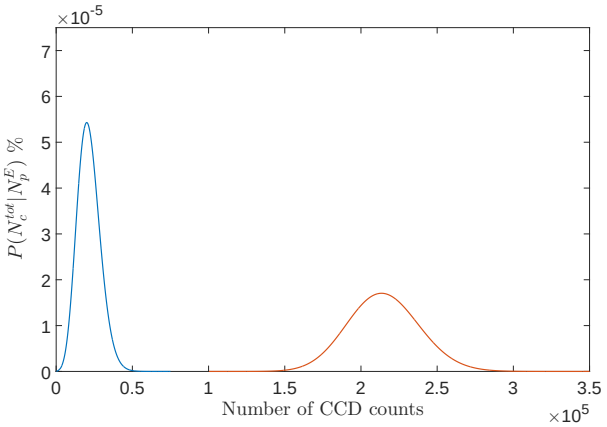

Figure 9.5: blue: probability distribution $P(N_c^{tot}|N_p^E)$ for an average number of detected photons $\bar{N}_p^D = 10$. Red: probability distribution $P(N_c^{tot}|N_p^E)$ for an average number of detected photons $\bar{N}_p^D = 100$. The most probable number of counts $N_c^{tot,max}$ are, respectively, 19770 and 213213.

In fig. 9.5, the distributions $P(N_c^{tot}|N_p^E)$ for $\bar{N}_p^D = 10$ (blue), and $\bar{N}_p^D = 100$ (red) are plotted. They correspond to numbers of emitted photons of, respectively, 59880 and 598800. These distributions have a Gaussian shape, which is expected from the

fact that the binomial distribution used in eq. (9.5) tends to a Gaussian distribution as N_p^E becomes larger [121].
The distributions corresponding to situations such that $\bar{N}_p^D = 0.1, 0.5$ and 1 and corresponding to $N_p^E = 599$, 2994 and 5988 are shown on fig. 9.6. The distributions show almost no shift in the most probable number of CCD counts $N_c^{tot,max}$, but become larger and asymmetrical as $\bar{N}_p^D$ increases. This is consistent with the fact that these distributions correspond to situations where the most probable events are $N_p^D = 0$ or 1, and that it becomes more probable to detect more photons and therefore more counts on the CCD as $\bar{N}_p^D$ gets closer to 1.

Finally, we plot on fig. 9.7 $P(N_c^{tot}|N_p^E)$ for $\bar{N}_p^D = 1$, 2 and 3 ($N_p^E = 5988$, 11976 and 17964). As can be seen on the figure 9.7, the distribution shows a pronounced asymmetry in the three cases. Its behavior as N_p^E becomes larger may be understood by noting that for higher N_p^E, a wider range of CCD counts become comparatively "probable". All the distributions are normalized, therefore an increased probability to detect a higher number of CCD counts accordingly results in a decreased probability to detect 0 counts (not shown on the figures).

We are now ready to look into the "reverse" problem, i.e. inferring the most probable number of emitted photons given a number of CCD counts, but before we do so, we can make the following remarks:

- Our model is such that the CCD camera records a non-zero number of counts *only if* $N_p^D \neq 0$. On the other hand, the smallest number of photons our system can detect is, obviously, *one*. Therefore, detecting one photon leads our model to predict that most probably 6600 photons were emitted, even in the - unlikely, but not impossible - case of the detection of one photon following the emission of much less than 6600 photons. In cases corresponding to N_p^E's such that $\bar{N}_p^D < 1$ this effect leads to a systematic overestimation of $N_p^{E,max}$.

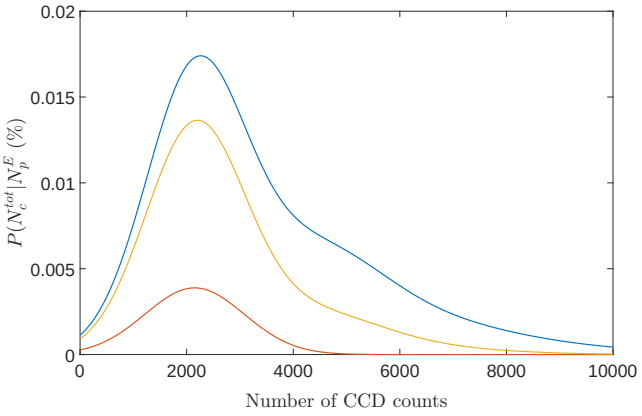

Figure 9.6: Probability distributions $P(N_c^{tot}|N_p^E)$ of measuring N_c^{tot} CCD counts given N_p^E emitted photons. Values of N_p^E are 599 (red), 2994 (yellow) and 5988 (blue), corresponding to, respectively, $\bar{N}_p^D = 0.1$, 0.5 and 1 and $N_c^{tot,max} = 2142$, 2192 and 2252.

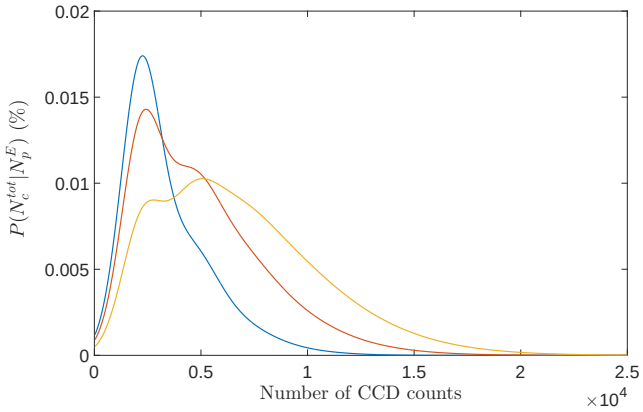

Figure 9.7: Probability distributions $P(N_c^{tot}|N_p^E)$ of measuring N_c^{tot} CCD counts given N_p^E emitted photons. Values of N_p^E are 5988 (blue), 11976 (red) and 17964 (yellwo), corresponding to, respectively, values for $\bar{N}_p^D$ of 1, 2 and 3, and $N_c^{tot,max} = 2252$, 2412 and 5065.

- As long as the most probable event is the detection of one photon, the model will accordingly predict a number of emitted photons ~ 6600. Since this happens in situations where $\bar{N}_p^D > 1$ (see fig. 9.7), we expect in this case to underestimate the number of emitted photons.

These effects can be traced back to the behaviors of the binomial and normal distributions from which $P(N_c^{tot}|N_p^E)$ is calculated. Accordingly, we expect that the relative error we make when inferring the number of emitted photons decreases when N_c^{tot} or N_p^E increases. Because these errors are directly linked to the low detection efficiency of our setup, we can think of it in terms of a "resolution": the relative error we make when guessing N_p^E is large as long as N_p^E is not large compared to 6600, and decreases for an increasing number of emitted photons.

We calculate now the distributions $P^{eff}(N_p^E|N_c^{tot})$ for values of N_c^{tot} corresponding to the values $N_c^{tot,max}$ determined previously. These distributions need to be normalized, so we define $P^{eff}(N_p^E|N_c^{tot})$ as:

$$P^{eff}(N_p^E|N_c^{tot}) = \frac{P(N_c^{tot}|N_p^E)}{\sum_{N_p^E=0}^{\infty} P(N_c^{tot}|N_p^E)} \tag{9.7}$$

where N_c^{tot} is fixed. Examples of this distribution can be seen, for example, on figure 9.8 where the values $N_c^{tot,max}$ are taken from the figure 9.7. As expected, since $N_c^{tot,max}$ differ very little for $\bar{N}_p^D = 1$ and $\bar{N}_p^D = 2$, the distributions show almost no differences between these two cases. The most probable number of emitted photons $N_p^{E,max}$ are 6650 and 6840, respectively, which shows that in the second case the number of emitted photons is underestimated by a factor of almost 2. For a number of CCD counts corresponding to $\bar{N}_p^D = 3$, we find $N_p^{E,max} = 14472$, corresponding to a deviation of about 22% from the "true" number of emitted photons (yellow curve

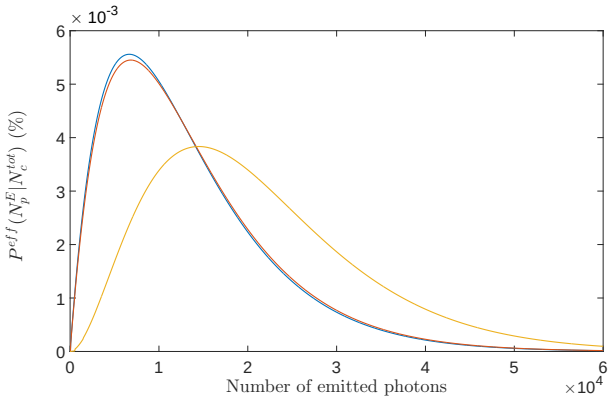

Figure 9.8: Probability distributions $P^{eff}(N_p^E|N_c^{tot})$ for values of N_c^{tot} corresponding to $N_c^{tot,max}$ obtained from the analysis presented in fig. 9.7. The most probable number of emitted photons is noted $N_p^{E,max}$. Blue: $N_c^{tot,max} = 2252$ and $N_p^{E,max} = 6650$, red: $N_c^{tot,max} = 2412$ and $N_p^{E,max} = 6840$, yellow: $N_c^{tot,max} = 5065$ and $N_p^{E,max} = 14472$

on fig. 9.8)
Opposite to this case is the situation where the number of emitted photons is much larger than the "resolution". Examples of these cases are shown on figs. 9.9, where the values $N_c^{tot,max}$ were taken from the figure 9.5. As anticipated, the relative error on the estimation of the number of emitted photons gets smaller, being 7.7 % for the blue curve, and $\sim 0.07\%$ for the red curve. In practice, the error on the estimation of the number of emitted photons is unknown, since the "true" number of emitted photons is unknown. Therefore we need a way to quantify our lack of knowledge on this number, and we choose to define the uncertainty on it in a way similar to that of the standard deviation at 68 % which applies in the case of a normal distribution.

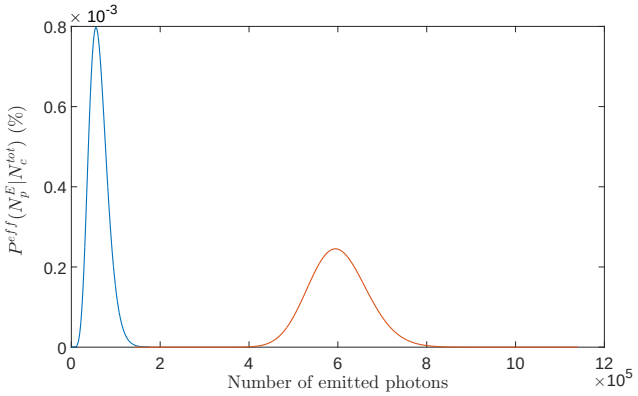

Figure 9.9: Probability distributions $P^{eff}(N_p^E|N_c^{tot})$ for values of N_c^{tot} corresponding to $N_c^{tot,max}$ obtained from the analysis presented in fig. 9.5. Blue: $N_c^{tot,max} = 19770$ and $N_p^{E,max} = 55440$. Red: $N_c^{tot,max} = 213213$ and $N_p^{E,max} = 594520$.

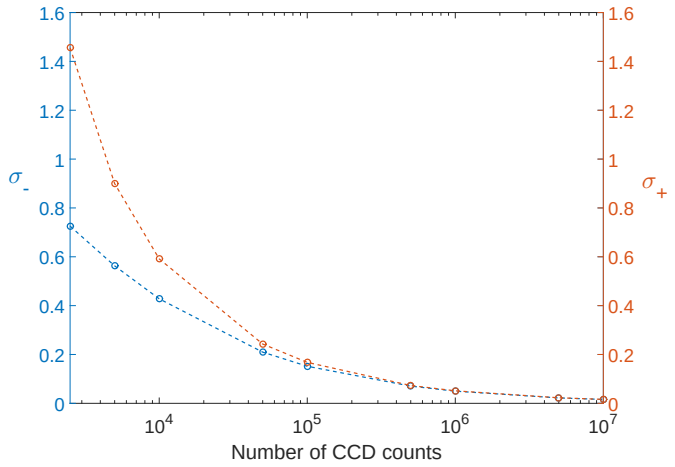

Figure 9.10: Fractional uncertainties σ_- and σ_+ on the most probable number of emitted photons versus the number of CCD counts.

That is, we define Σ_- and Σ_+ such that there is a probability of 68 % that a measurement of N_p^E falls within the interval $[\Sigma_-, \Sigma_+]$. The fractional errors on the most probable number of emitted photons $\sigma_\pm$ are simply given by $|N_p^{E,max} - \Sigma_\pm|/N_p^{E,max}$ and decrease when the number of CCD counts increases, as expected and shown on fig. 9.10, where the values of $\sigma_\pm$ have been calculated for values of N_c^{tot} ranging from 2.5×10^3 to 1.0×10^7, and plotted against the number of CCD counts.

9.2.3 Conclusion

In this section we have presented a model for the detection system, which allows us to infer the most probable number of emitted photons given a number of CCD counts, and to give an uncertainty on this number. This model is based on the knowledge we acquired by measuring key properties of the detection apparatus: the mean number of CCD counts for a single detected photon $\bar{N}_c = 2135 \pm 17$ and its variance $\sigma_c = 907 \pm 14$, from which we could deduce the detection efficiency of the setup: $P_{det} = (1.67 \pm 0.01) \times 10^{-4}$. The behavior of $P^{eff}(N_p^E|N_c^{tot})$ is consistent with what one would expect based on the analysis of $P(N_c^{tot}|N_p^E)$ and sheds light on the detection mechanism, and on its limitations. This model will be used in the next part in order to analyze the experimental data.

Part III

Localization spectroscopy of an ion in an optical lattice

Chapter 10

Introduction

10.0.3.1 General Motivation

Trapping neutral atoms cannot be done by using the techniques described in chapter 2, and instead requires the use of the force arising from the interaction between an electric dipole and the electromagnetic field. The first proposal to channel particles using the so-called optical dipole force was written by Letokhov in 1968 [122]. From then on, demonstrations of an increased control over the atom's motion quickly followed: in 1970 Ashkin demonstrated acceleration and trapping of micrometer-sized particle in counter-propagating laser beams [123], Bjorkholm in 1978 the focusing of neutral atoms with transverse dipole forces in a Gaussian laser beam [124], and finally three-dimensional confinement of atoms was reported in 1986 [125]. The techniques of atom trapping then became increasingly attractive due to the new possibilities they offer [126, 127], in particular to the field of high precision spectroscopy, and the possibility to access, study and manipulate atoms in the ultra-low energy region [68]. Confining cold atoms in tailored optical potentials has opened many possibilities for simulating many-body physics and performing quantum simulations. Because of their versatility, optical lattices have indeed become a widely used tool, as the lattice geometry can and depth can be changed almost at will by superimposing several independent laser sources and tuning their frequencies and intensities, thereby allowing fine control over the simulated Hamiltonian's parameters [128].

In contrast, charged particles can be confined in deep electromagnetic traps which leaves their internal energy levels essentially unperturbed. Their internal and external degrees of freedom can then be manipulated by light fields under well-controlled conditions. Nevertheless, combining optical potentials and electromagnetic trapping has recently received a growing interest in the community of physicists experimenting with trapped ions, because this could allow the study of cold chemistry experiments involving ions and neutral atoms [60, 62, 63, 129], of the Frenkel-Kontorova model for friction [44–46], the transport of heat in ion chains [46, 48, 49], quantum simulations of many-body physics with ion crystals [35, 37–42], study of the generalized Dicke models [50] and of dynamical localization [51]. It also potentially opens for the investigation of ion dynamics in quantum potentials [56–58], or for the control of the crystalline structure of large Coulomb crystals [52]. Moreover, the applica-

tion of cavity-generated optical potentials to trapped ions has natural applications for ion-based cavity quantum electrodynamics (cavity QED), where it could be used to optimize the phase matching of ion crystals to optical modes in cavity QED experiments [54, 96], or the investigation of nanofriction with dynamically deformable substrates [59].
Following an earlier observation in H. Walther's group in the 1990's of anomalous ion diffusion in a standing wave field [130], pure optical trapping of an Mg^+ion in a few micron region of a tightly focused beam [131], and subwavelength localization of ions in optical lattices were subsequently demonstrated in various settings [55, 132, 133]. More recently, studies of the stick-slip friction in a system consisting of a string of three ions placed in an optical lattice, and demonstration of its tunability from maximal to nearly frictionless by controlling the structural mismatch between the arrangement of the ions and the periodicity of the optical lattice have been reported in [47].

10.0.3.2 State of the art in our group

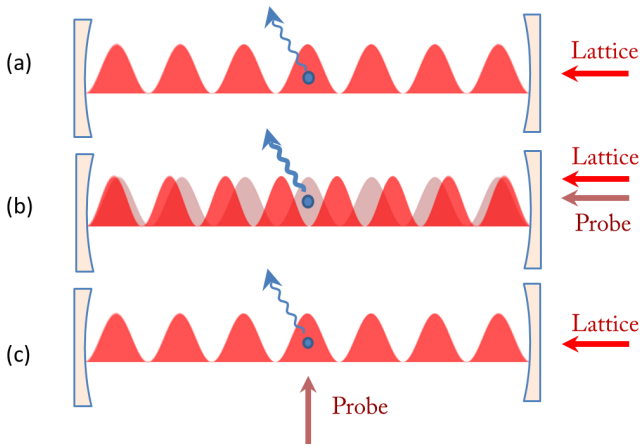

Figure 10.1: Three ways to probe the localization. In (a) the ion is placed in a red-detuned lattice (case illustrated here), or in a blue-detuned lattice, and the resulting fluorescence is monitored. In (b) the ion is localized at the node of a blue-detuned optical lattice, while a near-resonant intracavity probe field detuned from the optical lattice by an even or odd (case illustrated here) number of FSR drives the $D_{3/2}$ to $P_{1/2}$ transition. Observation of increased fluorescence when the ion is localized at a probe antinode signals localization (see text for more details). (c) Scheme presented in this thesis: the ion is localized in a blue or red-detuned intracavity optical lattice and a probe directed orthogonally probes the position-dependent Stark shift of the $D_{3/2}$ and $P_{1/2}$ levels.

In our group, sub-wavelength localization in an intracavity standing wave field of a single and few ion crystals trapped in the linear Paul trap described in section 8.1 has been demonstrated [55, 64]. Since the resolution of our imaging system does not allow for a direct measurement of the position distribution of the ions in the optical lattice, the localization of the ions was observed using the ion's fluorescence in structured driving fields [55, 64]. In a first experiment (see fig. 10.1(a) and fig.

10.2), a $^{40}Ca^{+}$ ion was placed in the field of an intracavity optical lattice blue- or red-detuned with respect to the $D_{3/2}$ to $P_{1/2}$ transition, and inelastic scattering of the lattice light by the ion was observed on a CCD camera by monitoring its decay to the $S_{1/2}$ state. By comparing this signal for red and blue detuned lattices, unambiguous localization signal was obtained, since the effect of a red-detuned lattice is to pin the ion at the antinodes, increasing scattering beyond the delocalized average, while a blue-detuned lattice pins the ion at the nodes, where scattering is suppressed. A difference in scattering between the two scenarios constitutes therefore a signature of ion localization in the lattice potential, and is shown on fig. 10.2(b), where the probability to scatter a lattice photon is measured for various lattice depths. The observed signal is systematically higher in the case of an ion placed in a red-detuned field, indicating that the ion is pinned in the lattice's sites. In this experiment, due to the branching ratio of the $S_{1/2} \rightarrow P_{1/2}$ and $D_{3/2} \rightarrow P_{1/2}$ transitions, the ion decays out of the levels affected by the lattice with a large probability when scattering off the lattice. Therefore the scattering probability was evaluated by repeating a large number of times an experimental cycle starting with Doppler-cooling and optical pumping in the $D_{3/2}$ state, after which the lattice intensity was ramped-up adiabatically and the emission of 397 nm photons by the ion monitored. An analytical model assuming an initial thermal distribution in the axial potential of the Paul trap and adiabatic ramp up of the lattice was developed in order to predict the scattering signals expected in these experiments, and shows very good agreement with the experimental data. The scheme was subsequently extended to various structures consisting of strings of up to 8 ions, 2D "zig-zag" chains and 3D Coulomb crystals of 6 ions, shown on fig. 10.3.

In a second experiment (fig. 10.1b), the ion was pinned in an optical lattice and simultaneously excited with a near-resonant intracavity probe field. The boundary

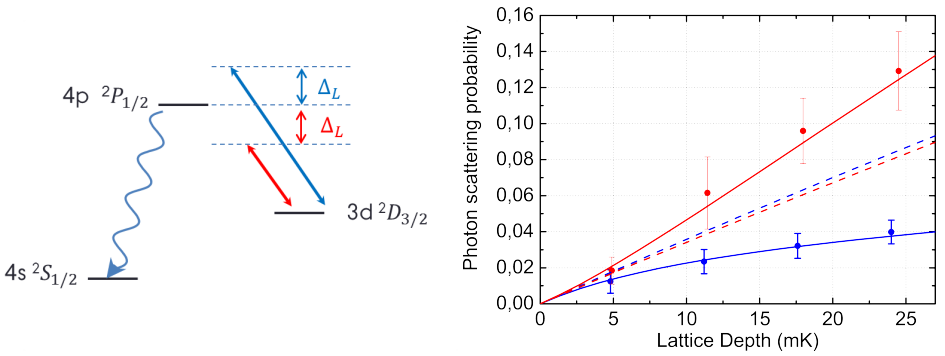

(a) (b)

Figure 10.2: Illustration of the first localization experiment performed in group and described in the text. (a) A blue- or red-detuned (detuning Δ_L) lattice is applied on the $D_{3/2}$ to $P_{1/2}$ transition. The fluorescence emitted on the $P_{1/2}$ to $S_{1/2}$ transition is collected. (b) Results obtained in the case of one ion localized in a blue and red-detuned lattice. Solid symbols: probability to scatter a lattice photon as a function of lattice depth for red and blue detuned lattices (square and circles respectively.) Solid curves: one-free-parameter model fit (see text for details).

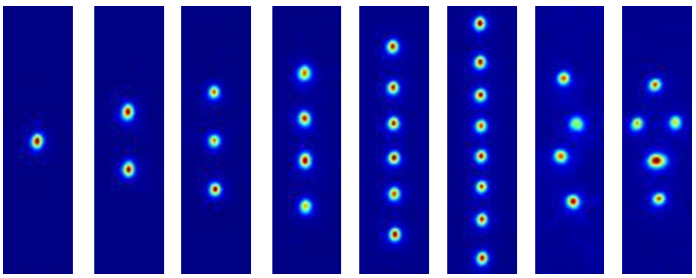

Figure 10.3: Projected images of the ion structures for which pinning in the optical lattice has been demonstrated. From left to right: 1D chains of one to four ions, chains of 6 and 8 ions. Second to last: two dimensional "zig-zag" structure of four ions. Last: three-dimensional octahedron consisting of 6 ions (the redest spot corresponds to two ions placed spatially in the plane perpendicular to the image).

conditions imposed by the cavity mirrors ensure that, at the ion's location in the center of the cavity, the standing wave of the probe field and the lattice are either in phase when they are separated in frequency by an even number of free spectral ranges, or out of phase when they are separated by an odd number of free spectral ranges. Suppression (in the first case) and enhancement (in the second case) of the probe induced scattering could then be observed. In particular, enhancement of the probe scattering probability from 50% of its maximum value in the case of a delocalized ion, to 81% in the case of a pinned ion was reported [55].

In the experiments described in the last part of this thesis, we demonstrate a method allowing the measurement of the motional probability distribution of an ion trapped in a far-detuned optical lattice. In these experiments, an ion is placed in an adiabatically raised optical lattice, and a probe field not coupled to the cavity mode is applied from the side (see fig. 10.1, (c)). The effect of the optical lattice is to induce position-dependent frequency shifts of the $D_{3/2} \rightarrow P_{1/2}$ transition, and measuring the spectrum of the probe field gives information on the energy distribution of the ion in the optical lattice. Measuring directly the energy distribution of a particle trapped in a dipolar potential - an ion in an optical lattice in our case - is interesting in order to gain precise information on the trap and atomic parameters which is necessary in view of precise control and manipulation of quantum states of individual atoms [134]. Furthermore, the energy distribution has been shown to be well-described by a Boltzmann distribution in cases where the lattice potential can be considered harmonic to a good approximation [134, 135], but a qualitatively different result is obtained when this assumption does not hold anymore [55, 64]. Measuring the energy distribution in the latter case could provide direct information on the thermal/non-thermal assumption and provide a means to assess the adiabaticity of the lattice ramp-up, for different ranges of atom and trap parameters. In the context of trapped ions, it could be used to reveal dynamical effects arising from the competition between the Coulomb force and the localizing effect of the lattice potential.
Our goal for the next chapter is threefold:

1. Develop a simple analytical scattering model in order to account for the observations. This model is based on knowledge accumulated in the aforementioned

experiments with ions placed in optical potentials [64].

2. Obtain an independent, absolute and quasi model-free measurement of the optical lattice intensity since the ion acts as a "powermeter" placed in the cavity, and is thus used to measure the effective lattice depth at its position.

3. Assess the usefulness of experimental methods for further spectroscopy experiments, for example the study of non-trivial dynamics of ion structures in optical lattices.

This scheme can be related to the one used in [136], where the channeling of an atom in an optical standing wave is observed by analyzing the absorption spectrum of the atom. This part is organized as follows: in section 11.1 we present the basic concepts of the localization spectroscopy method. In section 11.2, we apply this model to a two-level atom. We then consider a more realistic three-level structure appropriate for the $^{40}Ca^{+}$ ion in our experiments, and include the oscillatory motion of the ion inside a lattice well during the probing. In all models we assume the energy distribution to be thermal. In sections 11.3 and 11.4, details on the setup and experimental results are given. Finally, in chapter 12, we give an outlook and possible applications of the localization spectroscopy method presented here.

Chapter 11

Model and experiments

11.1 Principle of localization spectroscopy

We consider a dressed two-level atom placed in a red- or blue-detuned light field, and note its radiative decay rate Γ (in accordance with the notation used in chapter 3). We recall the expression for the energy of the states $|n, 1; \mathbf{r}\rangle$ and $|n, 2; \mathbf{r}\rangle$ (5.32) and (5.33) here for convenience:

$$E_{2n} = (n+1)\hbar\omega_L + \frac{\hbar\Delta_L}{2} - \frac{\hbar\Omega(\mathbf{r})}{2} \tag{11.1}$$

and

$$E_{1n} = (n+1)\hbar\omega_L + \frac{\hbar\Delta_L}{2} + \frac{\hbar\Omega(\mathbf{r})}{2} \tag{11.2}$$

where $\Omega(\mathbf{r}) = \sqrt{g^2(\mathbf{r}) + \Delta_L^2}$ was defined in section 5.4. E_{2n} is lowered inside the field, while E_{1n} is increased (see fig. 11.1). For a slowly moving atom (i.e. such that it

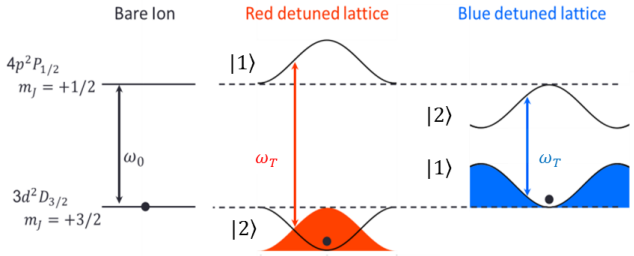

Figure 11.1: Illustration of the shift in energy of the $3d^2D_{3/2}$ and $4p^2P_{1/2}$ levels for an ion interacting with a red or blue-detuned lattice. On the left, the levels of an uncoupled ion. Center: in the case of a red-detuned lattice the ion is attracted to high intensity regions of the field, and the energy difference between the $D_{3/2}$ and $P_{1/2}$ levels is increased- Right: In the case of a blue detuned lattice, the ion seeks regions of vanishing intensity and sees a reduced transition frequency.

travels over a distance small compared to the optical lattice wavelength during the

radiative-relaxation time Γ^{-1}) placed in a far-detuned optical lattice ($\Delta_L \gg \Gamma$), it can be shown [81] that the mean potential energy for the atom in the field reduces to:

$$E_{pot} = -\frac{\hbar\Omega(\mathbf{r})}{2}(\pi_2^{st} - \pi_1^{st}) \tag{11.3}$$

where π_1^{st} and π_2^{st} are defined according to (5.42-5.43). The force exerted on the atom is therefore given by (see eq.()):

$$\mathbf{F} = -\nabla E_{pot} = -\frac{\hbar}{2}\nabla\Omega(\mathbf{r})(\pi_2^{st} - \pi_1^{st}) \tag{11.4}$$

In a far red-detuned field, π_2^{st} is much larger than π_1^{st}. The total force $\mathbf{F}$ then reduces to $\frac{\hbar}{2}\nabla\Omega(\mathbf{r})\pi_2^{st}$ and is directed towards zones of high intensity of the field. Similarly, in the case of a blue-detuned lattice $\mathbf{F} \sim -\frac{\hbar}{2}\nabla\Omega(\mathbf{r})\pi_1^{st}$ and is directed towards zones of vanishing intensity. When $\Delta_L \gg g(\mathbf{r})$, the expressions for E_{1n} and E_{2n} can be approximated by:

$$E_{2n} \approx (n+1)\hbar\omega_L - \frac{\hbar g^2(\mathbf{r})}{4|\Delta_L|} \tag{11.5}$$

and

$$E_{1n} \approx n\hbar\omega_L + \hbar\omega_0 + \frac{\hbar g^2(\mathbf{r})}{4|\Delta_L|} \tag{11.6}$$

In the case of a far blue-detuned field, similar expressions for E_{1n} and E_{2n} are obtained by exchanging the right hand sides in the above equations. Considering for the optical trapping field the case of a one-dimensional standing-wave, the Rabi frequency can be rewritten as[1]:

$$g(z) = g\sin(kz)$$

where $k = \omega_L/c$ is the lattice wave-vector. Finally, by using the results of the section 5.4, we can now write the energy difference between the $|1,n\rangle$ and $|2,n-1\rangle$ levels in the case of a red-detuned lattice:

$$E_{1n} - E_{2n-1} \simeq \hbar\omega_0 + \frac{\hbar g^2(\mathbf{r})}{2|\Delta_L|}\sin^2(kz) = \hbar\omega_0 + 2U_{latt}\sin^2(kz) \tag{11.7}$$

and the energy between $|2,n\rangle$ and $|1,n-1\rangle$ in the case of a blue-detuned lattice:

$$E_{2n} - E_{1n-1} \simeq \hbar\omega_0 - \frac{\hbar g^2(\mathbf{r})}{2|\Delta_L|}\sin^2(kz) = \hbar\omega_0 - 2U_{latt}\sin^2(kz) \tag{11.8}$$

where the depth of the optical lattice U_{latt} is defined such that $U_{latt} = \frac{\hbar g^2(\mathbf{r})}{4|\Delta_L|}$. The lattice depth can also be characterized by a temperature T_{latt} through $U_{latt} = k_B T_{latt}$, with k_B the Boltzmann constant. From the equations 11.7 and 11.8, we see that an ion at the antinode of a red-detuned optical lattice sees its frequency shifted by $2U_{latt}$, which can be much larger than Γ. In terms of temperature, this shift corresponds to

[1] We assume here that the intracavity standing wave can be described as the sum of two plane waves, and neglect the transverse Gaussian profile.

$\frac{2*k_B}{\hbar} \simeq 2\pi \times 41.7$ MHz/mK.

How do these concepts apply in our case? The optical standing wave field is applied on the $3d^2D_{3/2}$ to $4p^2P_{1/2}$ transition, with a detuning of $\Delta_L = \pm 2\pi \times 0.76$ THz (see fig. 10.2(a)). For a ~ 25 mK deep lattice, the Rabi frequency g is found to be approximately equal to $2\pi \times 40$ GHz. The mixing angle θ defined in (5.34-5.35) is then equal to 0.016 in the case of a red-detuned lattice ($\Delta_L > 0$), or $\pi/2 - 0.016$ for a blue-detuned lattice ($\Delta_L < 0$). In the first case, $\cos\theta \sim 1$, and $\sin\theta \sim 0$, and therefore the levels $|1;r\rangle$ and $|2;r\rangle$ can be in very good approximation be taken as the bare atomic levels $4p^2P_{1/2}$ and $3d^2D_{3/2}$, respectively. For a blue detuned lattice, the conclusion is reversed, and $|1;r\rangle$ and $|2;r\rangle$ can be identified to $3d^2D_{3/2}$ and $4p^2P_{1/2}$ respectively. In the following we will thus simply refer to them as the bare atomic levels. The steady state populations π_1^{st} and π_2^{st} can be calculated using eq (5.42-5.43), and for a red-detuned lattice $\pi_1^{st} \sim 10^{-7}$ which justifies that system spends most of its time in the state $|2;r\rangle$ and is therefore trapped at an antinode of the red-detuned field. Again, the conclusion is reversed in the case of a blue-detuned field, and it can be shown that the atom is, in this case, trapped at a node of the field.

Using the results of the above paragraph we can now write the energy difference between the $4p^2P_{1/2}$ and $3d^2D_{3/2}$ levels:

$$E(P_{1/2}) - E(D_{3/2}) = \hbar\omega_T \simeq \hbar\omega_0 \pm \frac{\hbar g^2(\mathbf{r})}{2|\Delta_L|}\sin^2(kz) = \hbar\omega_0 \pm 2U_{latt}\sin^2(kz) \quad (11.9)$$

in the case of a red (+) or blue (−) detuned lattice, where we have defined ω_T as the position-dependent frequency of the $D_{3/2}$ to $P_{1/2}$ transition. These results are summarized in the figure 11.1.

For an ion trapped in a red-detuned optical lattice, we therefore expect to see a shift of the resonance frequency of the $D_{3/2}$ to $P_{1/2}$ transitions which can be calculated from the previous considerations, and can be as large as $2\pi \times 1.04$ GHz for a 25 mK deep red-detuned optical lattice. This shift can be observed by, e.g., measuring the scattering of the ion in the lattice with a probe field applied on the $D_{3/2}$ to $P_{1/2}$ transition, as depicted in fig. 10.1(c). In the case of a blue detuned lattice, the transition frequency is unchanged. Observing the difference in resonant frequencies corresponding to the three different situations (ion trapped in a red-detuned field, ion trapped in a blue detuned field, ion not trapped) should therefore provide a clear signature of the localization. In the following section, we develop a model allowing us to predict the spectrum one should observe in a typical localization spectroscopy experiment. For the sake of pedagogy we will start with a simple two-level model, and go on with a more realistic, three-level model.

11.2 Theoretical models

11.2.1 Two-level atom

Using the steady-state solutions of the OBE derived in chapter 3, we can write the scattering rate from the level $P_{1/2}$ for the effective two-level system depicted on fig. 11.2, when the ion is trapped in a far-detuned optical lattice applied on the $D_{3/2}$ to

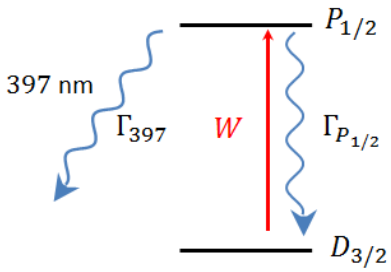

Figure 11.2: Energy levels considered in the fictitious two-level model. In this model, the state $P_{1/2}$ can spontaneously decay to $D_{3/2}$ with a decay rate $\Gamma_{P_{1/2}} = 2\pi\times 22.4$ MHz, such that the model gives the correct width for this transition. The measured scattering rate from the state $P_{1/2}$ is given by $\Gamma_{397} = 2\pi\times$ 20.7 MHz. The $D_{3/2} \leftrightarrow P_{1/2}$ transition is addressed by a probe field of Rabi frequency W.

$P_{1/2}$ transition, and driven by a probe field near-resonant with the same transition. We call W the probe Rabi frequency, and $\Delta_T(\delta_P, kz)$ the position-dependent probe-ion detuning:

$$\Delta_T(\delta_P, kz) = 2\frac{U_{latt}}{\hbar}\sin^2(kz) \pm \delta_P \tag{11.10}$$

with $\delta_P = \omega_P - \omega_0$ the probe detuning with respect to the natural $P_{1/2}$ to $D_{3/2}$ transition where ω_P is the probe frequency and the $\pm$ sign accounts for the case of a red $(-)$ or blue $(+)$ detuned lattice from this transition. For example, the probe field is resonant with an ion trapped at an antinode of the red-detuned lattice, $kz = \pm m\pi/2$ with m integer, when $\delta_P = 2U_{latt}/\hbar$ and $\Delta_T(2U_{latt}/\hbar, \pm m\pi/2) = 0$. With these notations the scattering rate at a given position inside the lattice reads:

$$\Gamma_{scatt}(kz) = \Gamma_{397}\frac{W^2/4}{\left(2\frac{U_{latt}}{\hbar}\sin^2(kz) \pm \delta_P\right)^2 + \frac{W^2}{2} + \frac{\Gamma_{P_{1/2}}^2}{4}} \tag{11.11}$$

where $\Gamma_{P_{1/2}} = 2\pi \times 22.4$ MHz is the total decay rate from the $P_{1/2}$ state, and $\Gamma_{397} = 2\pi \times 20.7$ MHz effectively gives the measured scattering rate of photons at 397 nm. In this simple situation, the effect of the lattice is, as mentioned before, to shift the frequency of the $P_{1/2} \leftrightarrow D_{3/2}$ transition by an amount equal to $2U_{latt}/\hbar$ in the case of a red-detuned lattice, while in the case of a blue detuned lattice this frequency is unchanged.

11.2.1.1 Accounting for the finite temperature of the ion

The theoretical model described in the previous section enables the calculation of useful parameters for the experiment, such as the expected scattering rate from the lattice and the expected frequency shift, but does not account for another important aspect of the experiment related to the non-zero kinetic energy of the ion inside the optical potential. The non-zero kinetic energy of the ion implies that the ion's position inside the trap is not fixed, and must therefore be described through a distribution

$P(kz)$, which needs to be determined. In such a case, the scattering rate Γ_{scatt} reads:

$$\Gamma_{scatt} = \int \Gamma_{scatt}(kz) P(kz) dkz \tag{11.12}$$

In order to choose a mathematical form for $P(kz)$, we consider the following facts:

- the ion is first Doppler cooled and prepared in the $|D_{3/2}, m_J = +3/2\rangle$ state where it is sensitive to the lattice and can be considered as a two-level system. The ion's position distribution after Doppler cooling can be considered thermal, and for the loose axial potential of the Paul trap considered in these experiments, this distribution extends over many lattice sites. It follows that the change in the harmonic trap potential within a single site is small compared to the thermal energy, and hence the potential in each site has approximately the same shape. Therefore, the ion's motion can be adequately described using a single site with periodic boundary conditions.
- The lattice is adiabatically raised - we shall give more details on this specific aspect below. According to the model developed in [55, 64], the ion's final position distribution in the lattice is, stricto-sensu, not thermal within the a lattice site , but for deep lattices can be considered so to a good approximation.

We shall therefore assume that the position distribution of the ion within a lattice site has an extension given by the corresponding Boltzmann factor, which should be reflected on the spectrum due to the position-dependent frequency shift of the $D_{3/2}$ to $P_{1/2}$ transition. Taking into account the position distribution of the ion inside the optical potential simply amounts to write $P(kz)$ as:

$$P(kz) = \frac{1}{Z} \exp\left(-\beta U_{latt} \sin^2(kz)\right) dkz \tag{11.13}$$

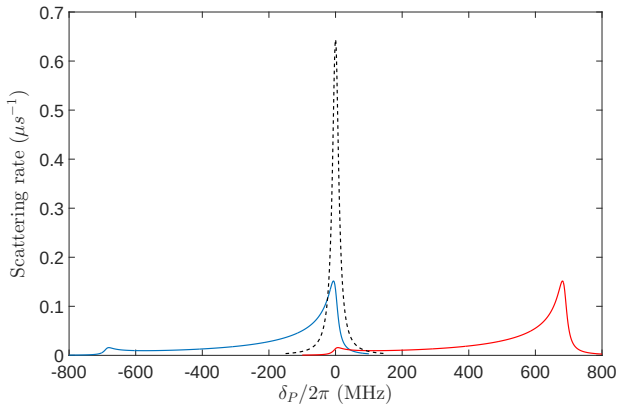

Figure 11.3: Simulations of spectra in the case of an ion localized in a red-detuned lattice (red, right), or a blue detuned lattice (blue, left). In these simulations, $T_{latt} = 16.5$ mK and $T_{ion} = 7$ mK, $\Gamma_{P_{1/2}} = 2\pi \times 22.4$ MHz, $\Gamma_{397} = 2\pi \times 20.7$ MHz, and $W = 0.1\Gamma_{P_{1/2}}/\sqrt{2}$ corresponding to 10% of the saturation intensity in this two-level system. The case of an ion without the lattice is shown in black for reference.

with

$$Z = \int_{-\infty}^{\infty} \int_{-\pi/2}^{\pi/2} \exp\left[-\beta\left(\frac{p^2}{2m} + U_{latt}\sin^2(kz)\right)\right] dkzdp$$

where $\beta = 1/k_B T_{ion}$, T_{ion} the ion's temperature inside the lattice well, p the ion's momentum, and $U_{latt}\sin^2(kz)$ the ion's potential energy inside the lattice. Therefore, in the case of a thermal ion, the scattering rate is given by:

$$\Gamma_{scatt} = \Gamma_{397}\frac{1}{Z}\int_{-\pi/2}^{\pi/2} \frac{W^2/4}{\left(2\frac{U_{latt}}{\hbar}\sin^2(kz) \pm \delta_P\right)^2 + \frac{W^2}{2} + \frac{\Gamma_{P_{1/2}}^2}{4}} \exp\left(-\beta U_{latt}\sin^2(kz)\right) dkz \tag{11.14}$$

An example of spectrum is shown on fig. 11.3 for a probe Rabi frequency $W = 0.1\Gamma_{P_{1/2}}/\sqrt{2}$ corresponding to 10% of the saturation intensity in this two-level system, T_{latt} =16.5 mK and T_{ion} =7 mK. In the case of a red-detuned lattice, the maximum of scattering is frequency-shifted by $2U_{latt}/2\pi$ = 688 MHz, whereas there is no shift in the case of a blue-detuned lattice. The profiles of the spectra, which are identical in these two cases, stem from the position distribution of the ions inside the optical lattice. The maximum of scattering is also identical in the two cases, and smaller than the maximum of scattering rate for an ion not placed in an optical lattice. To examine the effect of the temperature of the ion in the lattice, we plot on fig. 11.4 the probe spectra for T_{ion} = 1, 10 and 100 mK. As the ion gets hotter, the probability to find the

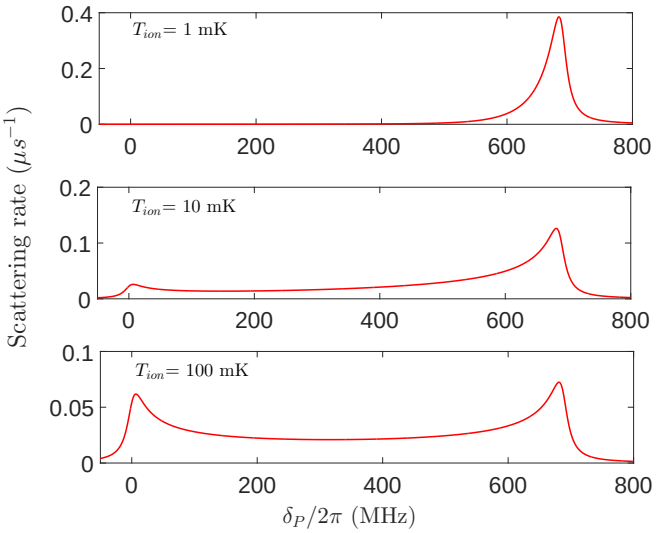

Figure 11.4: Illustration of the change in the spectra for an ion with a temperature of 1 mK (top), 10 mK (middle), or 100 mK (bottom) placed in a 16.5 mK deep lattice. All other parameters are similar as the ones used in fig. 11.3

ion in regions close to the maximum of the potential increases. In the case of a red-detuned lattice (shown on fig. 11.4) regions of maximum of potential corresponds to nodes of the optical lattice, and therefore this corresponds to an increasing scattering rate at probe detunings $\delta_P \simeq 0$. In the case of a blue-detuning, the conclusion is

the same, except that the regions of maximum of potential correspond to frequency detunings $\delta_p \simeq -2U_{latt}/\hbar$. Therefore, by measuring the position of these peaks and the whole profile, one can get in principle information on both the lattice depth and the ion's temperature inside the lattice well.

11.2.2 Three-level atom model

11.2.2.1 Optical Bloch equations

Realistically we have to consider the three-level open system made of the levels $S_{1/2}$, $P_{1/2}$ and $D_{3/2}$ of $^{40}Ca^+$. We will not derive here the OBE describing the internal

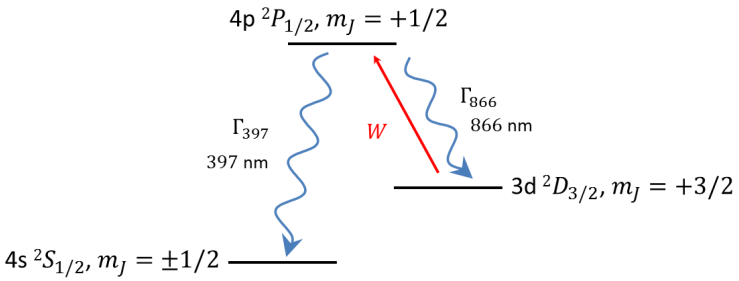

Figure 11.5: Three-level model consisting of the $3d^2D_{3/2}$, $4p^2P_{1/2}$ and $4s^2S_{1/2}$ levels in $^{40}Ca^+$. The $4p^2P_{1/2}$ level can decay to $4s^2S_{1/2}$ with the rate $\Gamma_{397} = 2\pi \times 20.7$ MHz and to $3d^2D_{3/2}$ with the rate $\Gamma_{866} = 2\pi \times 1.69$ MHz. The probe field is applied on the $D_{3/2} \rightarrow P_{1/2}$ transition with a Rabi frequency W.

dynamics of the ion by starting from first principles, but rather adapt the ones found in the case of a two-level atom in chapter 3 to the system shown on fig. 11.5. We consider the set of equations 3.10. The first two (3.10a and 3.10b) describe the variation of populations in ground and excited states due to the application of the driving light field, and the decay through spontaneous emission from the excited state. In (3.10a), the spontaneous decay rate is $\Gamma_{P_{1/2}}$ the decay rate from the $P_{1/2}$ state. In (3.10b), the $D_{3/2}$ state can only be repopulated due to the spontaneous decay from the $P_{1/2}$ state, with a partial decay rate Γ_{866}. The evolution of the coherences between the $D_{3/2}$ and $P_{1/2}$ states also depend on $\Gamma_{P_{1/2}}$. We note $\pi_{P_{1/2}}$, $\pi_{D_{3/2}}$ and $\pi_{S_{1/2}}$ the populations of, respectively, the $P_{1/2}$, $D_{3/2}$ and $S_{1/2}$ states, σ_{DP} and σ_{PD} the coherences between the states $D_{3/2}$ and $P_{1/2}$. Finally, we add a term describing the population of the $S_{1/2}$ state through spontaneous decay from the $P_{1/2}$ state, with the partial decay rate Γ_{397}:

$$\dot{\pi}_{S_{1/2}} = \Gamma_{397}\pi_{P_{1/2}} \tag{11.15}$$

With the notations introduced above, we have $\Gamma_{P_{1/2}} = \Gamma_{866} + \Gamma_{397}$. The new set of equation therefore reads:

$$\dot{\pi}_{P_{1/2}} = i\frac{W}{2}(\sigma_{PD} - \sigma_{DP}) - \Gamma_{P_{1/2}}\pi_{P_{1/2}} \tag{11.16a}$$

$$\dot{\pi}_{D_{3/2}} = -i\frac{W}{2}(\sigma_{PD} - \sigma_{DP}) + \Gamma_{866}\pi_{P_{1/2}} \tag{11.16b}$$

$$\dot{\sigma}_{DP} = -i\Delta_T(\delta_P, kz)\sigma_{DP} - i\frac{W}{2}(\pi_{P_{1/2}} - \pi_{D_{3/2}}) - \frac{\Gamma_{P_{1/2}}}{2}\sigma_{DP} \tag{11.16c}$$

$$\dot{\pi}_{S_{1/2}} = \Gamma_{397}\pi_{P_{1/2}} \tag{11.16d}$$

We emphasize here that this set of equations describes a system where the population is only transferred from the state $D_{3/2}$ to the state $S_{1/2}$ via the state $P_{1/2}$, and is never pumped back to $D_{3/2}$. The scattering probability can thus be inferred from the value of the population in the $S_{1/2}$ state at the end and depends on the Rabi frequency for the atom-probe coupling, the decay rates from the $P_{1/2}$ state, the atom-probe detuning, the probing time and the position of the ion inside the lattice site. All parameters except the decay rates can be varied in our experiments, and the population in the state $S_{1/2}$ corresponding to a probe Rabi frequency W, probing time t_f for an ion at the position z inside the lattice is denoted $\pi_{S_{1/2}}(W, \delta_P, kz, t_f)$. $\pi_{S_{1/2}}(W, \delta_P, kz, t_f)$ can be seen as the probability that a photon was emitted from the $P_{1/2}$ state after a time t_f and can be obtained by numerically integrating the set of equations 11.16:

$$\pi_{S_{1/2}}(W, \delta_P, kz, t_f) = \int_0^{t_f} \dot{\pi}_{S_{1/2}}(W, \delta_P, kz, t)dt \tag{11.17}$$

A particularity of the three-level model considered here compared to the two-level model of the previous section is that $\lim_{t\to\infty} \pi_{S_{1/2}}(t) = 1$ irrespective of the probe Rabi frequency, and of the probe-ion detuning. Examples of the evolution of $\pi_{S_{1/2}}(W, \delta_P, kz, t_f)$ as a function of t_f for various probe Rabi frequencies W and in the case of a probe resonant with the $D_{3/2} \to P_{1/2}$ transition are given on fig. 11.6. The larger the probe Rabi frequency, the sooner the population in $S_{1/2}$ saturates. Because of this saturation effect, the choice of duration and power for the probe beam is not trivial, and requires careful thought. Long probing times can be detrimental if the broadening of the probe spectrum due to this saturation effect becomes too large. An illustration of this phenomenon is shown on fig. 11.7, where a simulated spectrum of the $D_{3/2}$ to $P_{1/2}$ transition is plotted for different probing times and a Rabi frequency $W = 1.83 \times \Gamma_{866}$ (this value corresponds to the experimental one, as explained below). An obvious solution would thus be to work with a low probe power - to the extent, of course, that an observable signal is obtained. However, during the probing time the ion is also affected by the optical lattice, which effect is to add a frequency-independent background noise in our experiments, and which must be kept much smaller than the scattering from the probe. In order to choose the right parameters for the probe, we must therefore estimate the background from the lattice. This can be done by calculating the (steady-state) lattice-induced population in the $P_{1/2}$ state which is given by $\pi_2^{st}\sin^2\theta$, where $\sin^2\theta$ represents the weight of ket $|e\rangle$ in ket $|2\rangle$ in eq. (5.35). Choosing $\theta = 0.016$ (this value corresponds to a lattice red-detuned

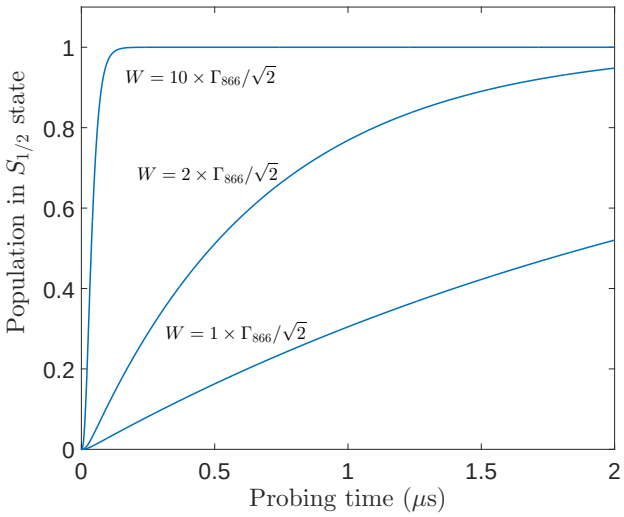

Figure 11.6: Dynamics of the population in the $S_{1/2}$ state for different probe Rabi frequencies W, in the case of a resonant probe field $\Delta_T(\delta_P, kz) = 0$.

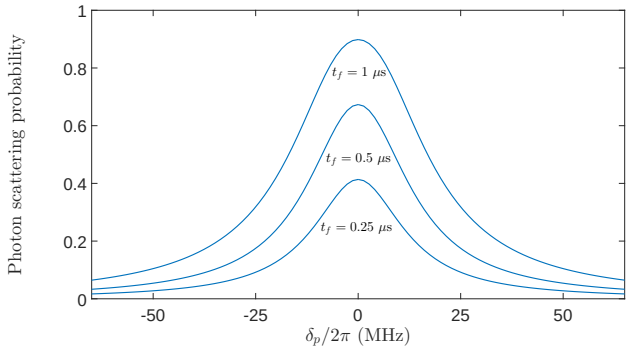

Figure 11.7: Simulated probe spectrum for an ion not placed inside the lattice, a probe Rabi frequency $W = 1.83 \times \Gamma_{866}$ and different probing times.

by 0.76 GHz and 25 mK deep, see section 11.1), one finds a steady-state population in $P_{1/2}$ approximately equal to 2.6×10^{-4}, from which we can deduce the scattering rate Γ_{latt} by multiplying it by Γ_{397}. We find $\Gamma_{latt} = 3.4 \times 10^{-2}\ \mu s^{-1}$. In a typical experimental run, the probe is applied *while* the ion is localized inside the optical lattice, and therefore the probing time t_f is at most equal to the time during which the lattice is held high. Moreover, the gating time of the imaging intensifier can be chosen to closely match the probing time, in order to reduce the noise from the lattice. It follows that an upper-bound on the lattice-induced scattering probability can be obtained by considering the time during which the lattice is applied, which we note t_l and, as we discuss below, is equal to 1 μs. The product $\Gamma_{latt} t_l$ is simply equal to $3.4 \times 10^{-2} \ll 1$ and therefore gives the sought scattering probability. Compared to the simulations showed on fig. 11.3 this is not negligible[2], and constrains the probe power which then cannot be too low - otherwise the lattice-induced background would reach a level where it becomes indistinguishable from the probe-induced scattering. In an ideal situation, one would choose a short probing time - in order to minimize the lattice-induced scattering - with a high probe power - to maximize the probe-induced scattering, and further increase the signal to noise ratio -, but as explained in the next section, technical constraints led to the choice of a probe duration of 0.5 μs. Finally, we can calculate the expected spectra taking into account the evolution of the population in the $S_{1/2}$ state by rewriting eq. (11.14) as:

$$P(\delta_P) = \frac{1}{Z} \int_{-\pi/2}^{\pi/2} \pi_{S_{1/2}}(\delta_P, kz) \exp\left(-\beta U_{latt} \sin^2(kz)\right) dkz \tag{11.18}$$

In the above expression, it is implicitly assumed that $t_f = 0.5\ \mu s$ and that the probe Rabi frequency W is held fixed at a value dictated by the constraints discussed above; they have been omitted for clarity. The difference with the expression given in eq. (11.14) is that the steady state population in the excited state is now replaced by the population in state $S_{1/2}$ at the time t_f. Accordingly, the expression 11.18 should be understood as a scattering probability after a probing time t_f and not a scattering rate as was the case for the two-level model.

11.2.2.2 Dynamics of the ion in the optical lattice during probing

For the deepest lattices, the oscillation frequency at the bottom of the well is on the order of 4 MHz, meaning that for a probing time of 0.5 μs the ion completes more than one period of the oscillation. This means that the position-dependent detuning is also time dependent during probing. To assess the effect of the motion during probing, we refine the model by taking into account this oscillatory motion of the ion inside the optical potential. This amounts to make the following change in the definition of the probe-ion detuning (11.10):

$$\Delta_T(kz) \rightarrow \Delta_T(kz(t)) = 2\frac{U_{latt}}{\hbar} \sin^2(kz(t)) \pm \delta_P \tag{11.19}$$

[2]On fig. 11.3 we have plotted the scattering *rate* as a function of the detuning, not the scattering *probability* stricto sensu. However, multiplying the scattering rates by $t_d = 1\ \mu s$ simply convert the y-axis into a scattering probability thereby allowing the comparison evoked in the text.

where $z(t)$ is the time-dependent position of the ion inside the optical trap, and is solution of the differential equation of motion of a pendulum:

$$\ddot{z}(t) + \frac{kU_{latt}}{m}\sin(2kz(t)) = 0 \tag{11.20}$$

where we have neglected the axial potential of the Paul trap[3]. In order to find $z(t)$, the above equation is numerically integrated during a time window corresponding to the probing time t_f, with initial conditions $kz(0)$ corresponding to all possible starting positions inside the lattice well for a given ion total energy E. Examples of the populations $\pi_{S_{1/2}}(kz(t))$ obtained by numerically integrating the OBE for the three-level atom with the time-varying detuning are given in fig. 11.8 for a lattice depth of 24.7 mK, a probe frequency equal to the ion's transition at the bottom of the potential well, a probe Rabi frequency $W = 1.83\Gamma_{866}$ and various ion energies. The oscillatory nature of the motion can be seen on the evolution of $\pi_{S_{1/2}}(kz(t))$, and, for an ion energy equal to $k_B \times 0.01$ mK, the dynamics of $\pi_{S_{1/2}}(kz(t))$ reduces to the one calculated in the case of a static ion. The total energy E of the ion is related to the ion's velocity $\dot{z}(t)$ and position $z(t)$ through:

$$(k\dot{z}(t))^2 + \omega_l^2 \sin^2(kz(t)) = \frac{2k^2}{m}E = \omega_l^2 \frac{E}{U_{latt}} \tag{11.21}$$

[3]This is justified since the oscillation frequency of the axial potential of the Paul trap is ~ 80 kHz, and is therefore much lower than the oscillation frequency at the bottom of the optical potential.

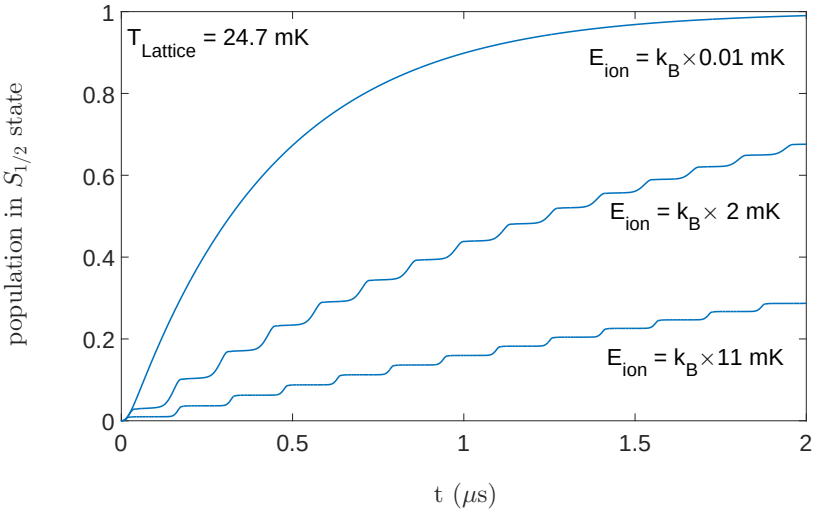

Figure 11.8: Dynamics of the population in the $S_{1/2}$ state for different probe Rabi frequencies W in the case of an oscillating ion, for a probe Rabi frequency $W = 1.83 \times \Gamma_{866}$, and $\delta_P = U_{latt}/\hbar$. For an ion whose energy is substantial compared to the lattice depth, the motion has a large amplitude and the pumping from the $D_{3/2}$ to the $S_{1/2}$ states is less efficient, than for an ion having a small energy and hence a motion of smaller amplitude.

where $\omega_l = \sqrt{\frac{2k^2 U_{latt}}{m}}$ is the oscillation frequency at the bottom of the lattice. The probability for an ion with energy E to be found at the position $kz(0)$ when the probe laser is switched on is noted $P(kz|E)$ and is not constant, but must reflect the fact that the ion spends more time close to the turning points of its motion where its velocity vanishes than in the center where its velocity is maximal. This probability is given by dt/T where T is the period of the trajectory. During a period of its motion, the ion' trajectory in phase space can be expressed by isolating $\dot{z}(t)$ in equation (11.21), and expressing it as a function of $z(t)$. It follows that the expression for the period of the trajectory reads:

$$T = 4\int_0^{kz_{max}} \frac{dkz}{k\dot{z}} \tag{11.22}$$

$$= \frac{4}{\omega_l}\int_0^{kz_{max}} \frac{dkz}{\sqrt{\frac{E}{U_{latt}} - \sin^2(kz)}} \tag{11.23}$$

where z_{max} is the position of the turning point, depends on $\frac{E}{U_{latt}}$ when $E < U_{latt}$, and is equal to $\pi/2$ otherwise. The period T can be re-expressed in terms of the complete elliptic integral of the first kind $\mathcal{K}(E/U_{latt})$ if $U_{latt} > E$ and $\mathcal{K}(U_{latt}/E)$ otherwise (see [137] and appendix B):

$$T = \frac{4}{\omega_l}\begin{cases} \mathcal{K}(\frac{E}{U_{latt}}), & E < U_{latt} \\ \sqrt{\frac{U_{latt}}{E}}\mathcal{K}(\frac{U_{latt}}{E}), & E > U_{latt} \end{cases} \tag{11.24}$$

From this we deduce the expression for $P(kz|E)dkz = dt/T$:

$$P(kz|E)dkz = \begin{cases} \frac{dkz}{2\mathcal{K}(\frac{E}{U_{latt}})\sqrt{\frac{E}{U_{latt}} - \sin^2(kz)}}, & E < U_{latt} \\ \frac{dkz}{\sqrt{\frac{U_{latt}}{E}}\mathcal{K}(\frac{U_{latt}}{E})\sqrt{\frac{E}{U_{latt}} - \sin^2(kz)}}, & E > U_{latt} \end{cases} \tag{11.25}$$

Examples of $P(kz|E)$ are shown fig. 11.9 for various values of E/U_{latt}. It is apparent on the plots shown on this figure that the probability to find the ion in the center is close to zero, while it diverges for positions close to the turning points, for energies E smaller than the lattice depth. For energies larger than the lattice depth, the probability tends to a constant value, in accordance with the fact that an ion whose energy is much greater than the lattice depth will be found anywhere with a quasi-constant probability. Since we cannot use the probability distribution in position given in eq. (11.13) in the case considered here, we calculate, in addition to the probability density $P(kz|E)$, the probability distribution for an ion to have the energy E within dE, for a given temperature. Formally, this distribution is given by:

$$P(E)dE = \frac{1}{Z}\Omega(E)\exp(-\beta E)dE \tag{11.26}$$

$$= \frac{2\omega_l}{ZU_{latt}}\left[\int_0^{kz_{max}} \frac{dkz}{\sqrt{\frac{E}{U_{latt}} - \sin^2(kz)}}\right]\exp(-\beta E)dE \tag{11.27}$$

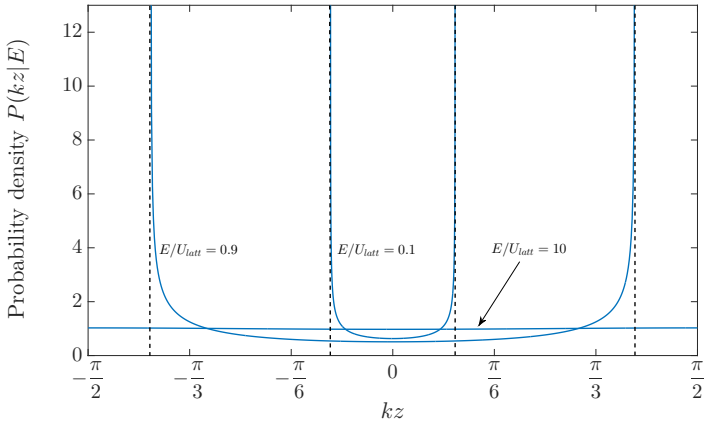

Figure 11.9: Illustration of the probability density $P(kz|E)$ for values of E/U_{latt} equal to 0.1, 0.9 and 10. For $E/U_{latt} < 1$, the probability density diverges at the turning points of the motion, reflecting that the velocity goes to zero at these positions. For $E > U_{latt}$, the probability density tends to a flat distribution.

where $\Omega(E) = 2\frac{\omega_l}{U_{latt}} \int_0^{kz_{max}} \frac{dkz}{\sqrt{\frac{E}{U_{latt}} - \sin^2(kz)}}$ is the density of states (a derivation of this expression is given in appendix C). This distribution is plotted in fig. 11.10. Finally, the scattering probability reads:

$$P(\delta_P) = \int_0^{\infty} dE P(E) \int_{-kz_{max}}^{kz_{max}} dkz_i \pi_{S_{1/2}}^{z_i} P(kz_i|E) \tag{11.28}$$

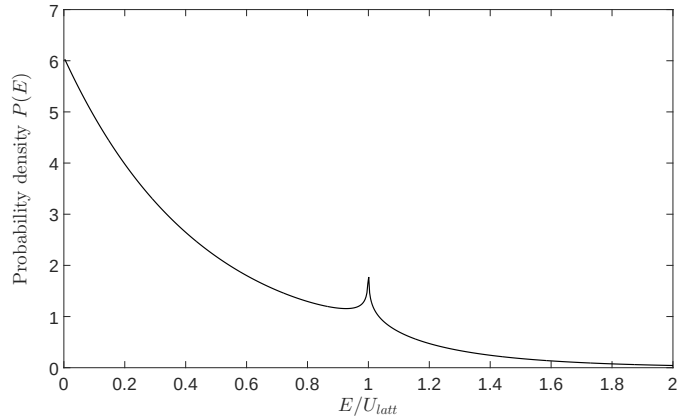

Figure 11.10: Probability density $P(E)$ versus E plotted here in the case of a lattice depth of 16.5 mK and an ion temperature of 7 mK.

where $\pi^{z_i}_{S_{1/2}}$ denotes the population in $S_{1/2}$ state at $t = t_f$ corresponding to a motion starting at $z_i \in [-z_{max}, z_{max}]$ at $t = 0$, and where we have omitted the dependence on δ_P for clarity. As an example we plot in fig. 11.11 a comparison of the results obtained with the model presented here and with the "static" model of section 11.2.1, in the case of a lattice with depth 16.5 mK and an ion temperature of 6.92 mK. Although the oscillatory motion of the ion leads to a less efficient transfer of population from the $D_{3/2}$ state to the $S_{1/2}$ state (fig. 11.8), the weighting by $P(E)$ and $P(kz_i|E)$ in eq. (11.28) effectively results in a slightly increased scattering probability. It has, however, no effect on the position of the resonance, nor does it affect the global shape of the spectrum. Due to the long computation time it requires, this model will not be used to analyze the data presented in section 11.4, where instead an "adjusted two-level atom model" is used, as explained below.

11.3 Experimental implementation

11.3.1 Experimental sequence

Due to the very large shifts the ion undergoes when trapped in the optical potential it is not possible to continuously cool the ion, or to optically pump it in the desired state when the lattice is applied. The experiment therefore follows a sequence in which an ion is first Doppler-cooled by simultaneously applying the Doppler cooling laser at 397 nm on the fast cycling $S_{1/2} \rightarrow P_{1/2}$ cooling transition, and the repumping diode laser (866-2) at 866 nm on the $D_{3/2} \rightarrow P_{1/2}$ transition in order to keep the ion cycling until it is cooled down. The ion is then optically pump into the $m_J = +3/2$ Zeeman substate of the $D_{3/2}$ state by applying the Doppler cooling laser and the optical pumping laser (866-2). The circularly σ^--polarized optical lattice (866-1) is

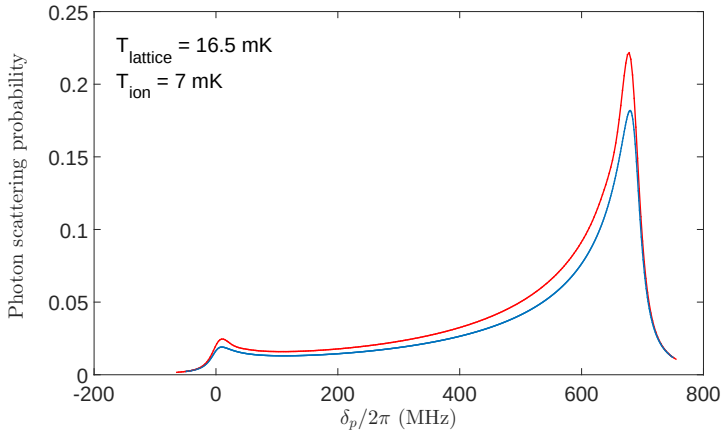

Figure 11.11: Comparison of the spectra obtained with the three-level model of section 11.2.2 in the case of a static ion (blue), and an oscillating ion (red), for $T_{latt} = 16.5$ mK, and $T_{ion} = 6.92$ mK, probing time t_f =0.5 μs and probe Rabi frequency $W = 1.83 \times \Gamma_{866}$.

then ramped up, and finally the light issued from the circularly σ-polarized 866-4 diode laser is used to probe the $D_{3/2}$ to $P_{1/2}$ transition. The choice for the durations for each of these phases depends on both theoretical and practical reasons:

1. The cooling part of the sequence cannot be too short since Doppler cooling is not instantaneous after the optical lattice is switched off. Measuring the temperature of the ions by looking at their profile on the images taken with the CCD camera for different cooling durations indicate that a 62 μs cooling time is enough to reach a steady temperature of about 2.5-3 mK, regardless of the lattice. With an axial trap frequency of 80 kHz, this corresponds to an ion initially spread over 1.5 μm, much larger than the distance between two consecutive maxima of the optical lattice, equal to 433 nm.

2. Measurements of the population in the various states Zeeman substates of $D_{3/2}$ shows that optical pumping allows to transfer nearly 99% of the population in the $m_J = +3/2$ state after ~ 50 μs [64].

3. After the optical pumping stage, the cooling and optical pumping lasers are switched off. The intensity of the lattice field is then ramped up during 2 μs. This process is controlled with an AOM and this duration ensures that this is done adiabatically, as explained in more details below.

4. The lattice is held at its maximum power for a time $t_l = 1$ μs, and probing takes place during the last 0.5 μs by applying the 866-4 probing laser and opening the imaging intensifier.

The timing sequence is summarized in fig. 11.12. One sequence is 114.5 μs. A given experimental run yields 30 images with 10 s integration time each, and thus corresponds to a total of $\sim 2.6\times10^6$ sequences. According to the simulations presented above, the scattering probability per sequence is at most on the order of 20%, and taking into account the detection efficiency of 1.67×10^{-4} this leads to the detection of typically 90 photons per 30 images. When recording a spectra, many images are taken off-resonance, thus the number of photons detected is usually much smaller.

11.3.1.1 Optical pumping

In order to have a two-level atom situation and to increase the coupling strength with the lattice it is necessary to optically pump the ion's population in the $m_J = +3/2$ substate of the $D_{3/2}$ state prior to the optical trapping and probing stages. The interaction strength with the lattice field from this state is three times larger than from the $m_J = +1/2$ substate (the corresponding Clebsch-Gordan coefficients are respectively $\sqrt{1/6}$ and $\sqrt{1/2}$, see appendix A.3). In order to optically pump the population in the $m_J = +3/2$ substate the OP beam is directed at 45° with respect to the trap axis and passes through a set of half- and quarter- wave plates with carefully adjusted angles before entering the chamber. The OP beam then possess both π and σ^+ polarized components, but no σ^- component. During optical pumping, the cooling, and optical pumping beams are switched on at the same time.

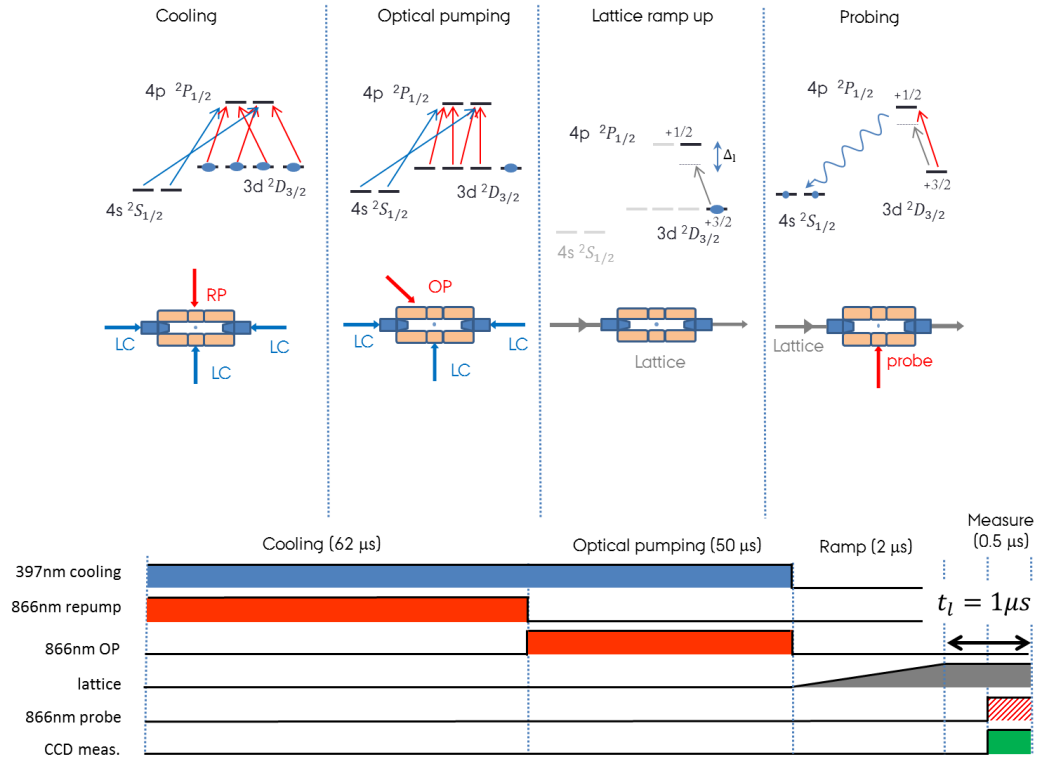

Figure 11.12: Schematic of the laser sequence.

11.3.1.2 Adiabatic ramp up of the lattice

As mentioned above, the lattice is raised slowly enough to be closely approximated as adiabatic. The reason for this is that it allows making predictions of the final energy distribution inside the optical potential. Indeed, in the case of a harmonic potential adiabatically ramped-up, the populations of the different vibrational states are unchanged before and after the lattice ramp-up, and only the energy and hence the temperature are re-scaled. Although this is only exactly true for a harmonic potential, such an assumption constitutes, as we will see in section 11.4 a reasonable starting point for our experiments. Adiabatic ramp up is in theory valid only in the limit $|\dot{\omega}_l/\omega_l^2| \to 0$. In practice the rate at which the lattice is ramped up is, again, the result of a trade-off between a desirable slow raise of the lattice depth, and the necessity to keep the time-increasing lattice-induced scattering probability as low as possible. The ramp is chosen to be linear in Rabi frequency and therefore to vary as t^2 in intensity, but due to the response time of the AOM the variation in intensity was found to go as $\sim t^{1.4}$ [64]. For the deepest lattice used, the final depth was approximately 25mK, and the ramp time was 2 μs corresponding to a mean rate of 6.25 mK/μs^2 . With these values, the ratio $|\dot{\omega}_l/\omega_l^2|$ is equal to 0.01, and molecular dynamics simulations show that the ramping is close to adiabatic, though not quite [64]. Nevertheless, the previous localization experiments described

in [64] indicated that the scattering signal in this situation still agrees with what one would expect from a model assuming adiabatic ramp-up. We therefore chose to keep the same parameters in our experiment. After ramp-up, the lattice intensity is kept constant for 1 μs. This duration is a compromise choice: it has to be long enough in order to allow for a detectable probe-induced fluorescence, but at the same time has to be shorter than the ion's lifetime in the lattice.

11.3.1.3 Probe scattering and imaging intensifier gate

In order to choose the probe power we were guided by experimental considerations: as explained above the lattice is held high during 1 μs and the probe time must therefore be shorter. Additionally, the probe power must be chosen in order to ensure that the fluorescence signal is dominated by the probe-induced scattering while at the same time avoiding significant broadening of the transition. Probing times shorter than 0.5 μs could be chosen in principle, but the AOM response time imposes a limitation on the pulse length, and in order to keep the pulse as "square" as possible, the plateau must be somewhat longer than the ramping up and ramping down times. For these reasons, we chose a probing time window of 0.5 μs. With these parameters we measured the probability to scatter a photon under resonant excitation for different probe excitations. The corresponding saturation curve is shown fig. 11.13, where it is plotted as a function of the probe power, measured with a power meter before the vacuum chamber. The above considerations concerning the expected scattering probabilities by the lattice and the probe led to the choice of a probe power of about 100 μW corresponding to an on-resonant scattering probability $\sim 67\%$. The probe laser frequency is continuously monitored and locked to a commercial wavemeter, as described in chapter 8.3. The other utility of the saturation curve shown on fig. 11.13 is to precisely calibrate the probe power seen by ion, which, in turn, is necessary in order to analyze the experimental data. To do so, the saturation signal was fitted with the solution of the OBE (11.17) with the probe power seen by the ion written as $\alpha \times P_{probe}$ where P_{probe} denotes the probe power measured before the vacuum chamber and corresponds to the x-axis on the graph shown in fig. 11.13, and α is the fitting parameter. From the fit α is found to be equal to 0.896 ± 0.002, and therefore a probe power measured before the vacuum chamber of 100 μW gives a scattering probability corresponding to an ion "seeing" a probe power of 89.6 ± 0.2 μW, which, for waists in the horizontal and vertical dimensions equal to, respectively, 2.87 mm and 110 μm corresponds to a Rabi frequency $\sim 1.83 \times \Gamma_{866}$ (see section A.5 in appendix A). Finally, the imaging intensifier gate is chosen to be slightly larger than 0.5 μs, and centered on the probe time window in order to ensure that we collect as many photons scattered by the probe as possible, but at the same time that we collect as few extra photons scattered by the lattice as possible.

11.4 Results

11.4.1 Calibration of the two-level model

For practical reasons in connection with the very long computation times in the case of the three-level atom models, all spectra were fitted using the two-level atom model with the parameter $\Gamma_{P_{1/2}}$ adjusted so as to take into account the broadening due

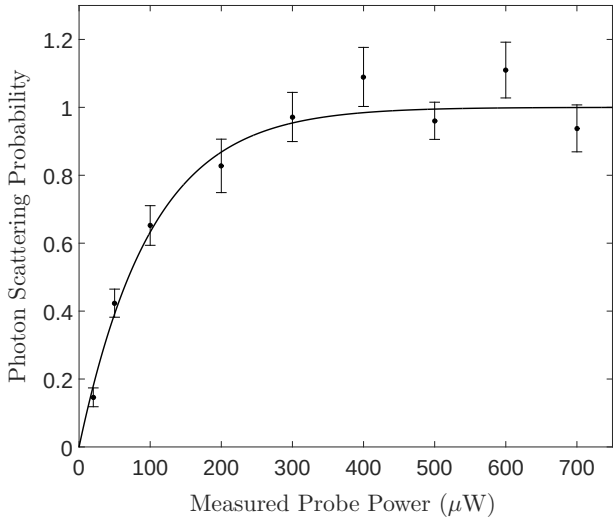

Figure 11.13: On resonance saturation curve showing the photon scattering probability versus the probe power measured before the vacuum chamber. The experimental data is fitted with the three-level atom model with the probe power seen by the ion as the fitting parameter (see text for details) and probing time $t_f = 0.5\ \mu s$.

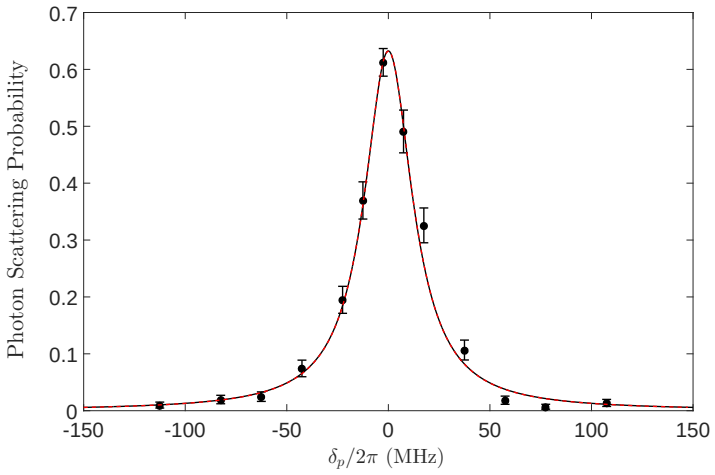

Figure 11.14: Spectrum of the $D_{3/2}$ to $P_{1/2}$ resonance of a bare ion versus the probe detuning δ_P. Solid circles: Experimental data. The probe power measured before the vacuum chamber is 100 μW. Dashed red line: Numerical simulation using the three-level "static" model, with a probe Rabi frequency corresponding to an effective power of 89.6 μW, and a probing time $t_f = 0.5\ \mu s$. Solid black line: Fit using the two-level model, with $\Gamma_{P_{1/2}}$ as fitting parameter, fixed probe power of 89.6 μW, and maximum scattering probability normalized to that of the three-level model.

to the probing time (section 11.2.2), and with the ion temperature and the lattice depth as free parameters. The adjustment of $\Gamma_{P_{1/2}}$ was done by fitting the resonance spectrum of the bare ion shown on fig. 11.14 with the two-level model, with $\Gamma_{P_{1/2}}$ in eq. (11.11) as the fitting parameter.

11.4.2 Experimental results

11.4.2.1 Presentation of the results

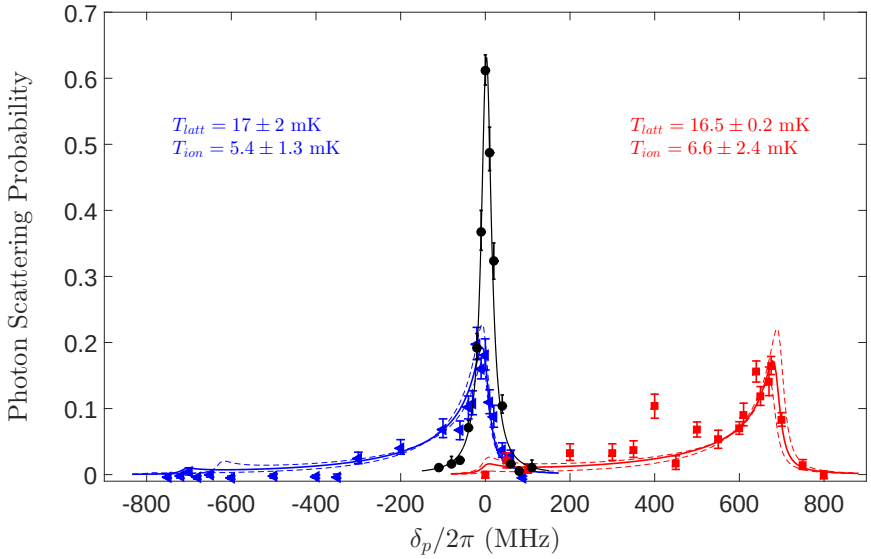

Figure 11.15: Spectra corresponding to an ion localized in a red-detuned lattice (red squares), a blue detuned lattice (blue triangles) and for an ion without an optical lattice (black circles). All the data was taken with a probe power of 100 μW (measured before the vacuum chamber). The lines indicate a fit to the two-level adjusted model described above, with as fitting parameters the ion temperature and the lattice depth. The dashed lines correspond to the numerical simulations with extreme values of T_{latt} and T_{ion} as input parameters.

Figure 11.15 shows experimental results for blue- and red-detuned lattices of identical depths of ~ 17 mK. These spectra are plotted along with the spectrum without lattice shown on fig. 11.14 for reference. As expected, the spectra corresponding to the ion localized in the red- or blue-detuned lattices show a pronounced asymmetrical broadening, and the maximum of scattering probability in the spectrum corresponding to an ion localized in a red-detuned lattice is shifted towards high frequencies compared to the bare resonance, while this is not the case for the spectrum corresponding to the ion localized in the blue-detuned lattice. Moreover, the maximum scattering probability in the cases of the ion localized in the lattice is much lower than for the bare ion. Finally, these spectra are in very good agreement with the simulations showed on fig. 11.3, which is a good indication that our simple model

captures the essentials of the physics of the localization process. In all spectra, the constant background of typically 2% due to the lattice-induced scattering is independently measured by running a sequence without probing the ion with the $866-4$ laser but keeping the same imaging gate, and by recording the fluorescence. This background has been subtracted to all the spectra shown in this section.
The spectra are fitted with the adjusted two-level model as indicated in section 11.4.1, with T_{latt} and T_{ion} as fitting parameters. In the case of a red-detuned lattice, the fit returns $T_{latt} = 16.5 \pm 0.2$ mK and $T_{ion} = 6.6 \pm 2.4$ mK, and the case of a blue-detuned lattice, $T_{latt} = 17 \pm 2$ mK and $T_{ion} = 5.4 \pm 1.3$ mK. The uncertainty on the lattice depth is much smaller in the case of the red-detuned lattice than in the blue-detuned lattice, since it is given by the position in frequency of the maximum of scattering, and, as mentioned in section 11.1, can be determined with a great accuracy owing to the large value of $k_B/\hbar$. Indeed, an uncertainty of 0.2 mK on the lattice depth in this case corresponds to an uncertainty of 0.5 MHz on the position of the peak of scattering probability. The uncertainty on T_{ion} is larger in both cases, and the values returned by the fit in both the blue- and red-detuned cases are in reasonable agreement.

On fig. 11.16, spectra measured in the case of a lattice with $T_{latt} \sim 8.5$ mK

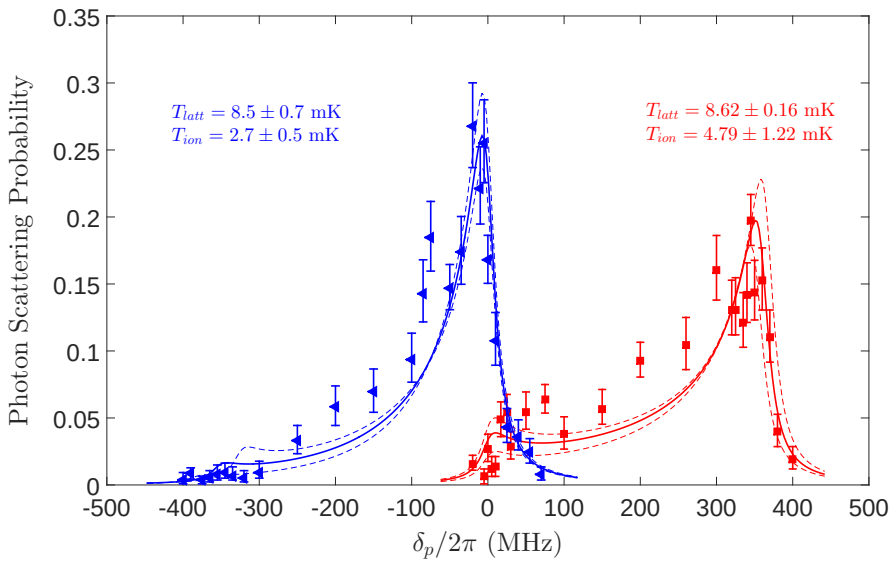

Figure 11.16: Spectra corresponding to an ion localized in a red-detuned lattice (red squares), and in a blue detuned lattice (blue triangles). All the data was taken with a probe power of 100 μW (measured before the vacuum chamber). The lines indicate a fit to the two-level adjusted model described above, with as fitting parameters the ion temperature and the lattice depth. The dashed lines correspond to the numerical simulations with extreme values of T_{latt} and T_{ion} as input parameters.

are presented. These spectra globally show the same features as the ones discussed previously, but compared to the previous spectra, the experimental data seems to deviate more from the analytical model, which predicts a systematically lower scattering

probability than what is observed. The depth of the lattice is in the red-detuned case $T_{latt} = 8.62 \pm 0.16$ mK, and in the blue-detuned case $T_{latt} = 8.5 \pm 0.7$ mK, values in good agreement with each other. However, the ion temperature in the red-detuned case $T_{ion} = 4.79 \pm 1.22$ mK strongly differs than the one in the blue-detuned case, which is $T_{ion} = 2.7 \pm 0.5$ mK. Finally, in all spectra presented here and corresponding to the ion localized in the blue-detuned lattice, the secondary peak in scattering probability predicted by the model for detuning $\delta_P = -2\frac{U_{latt}}{\hbar}$ is small, whereas its counterpart around δ_P in the red-detuned lattice is more pronounced.
On fig. 11.17(a) spectra corresponding to the ion localized in red-detuned lattices of depths
$T_{latt} = 8.5$, 12.5 and 24.7 mK are shown together. The positions in frequency of the maximum of scattering are plotted as a function of the lattice input power on fig. 11.17(b), where they are shown to be in excellent agreement with the linear relationship between lattice input power and frequency shifting of the resonance (see eq.(11.9)), and demonstrate the robustness of this method to measure the depth of the optical lattice.

11.4.3 Discussion

Overall, the data presented above is in satisfying agreement with the analytical model proposed in this work: the prediction of the scattering probabilities and global shapes of the spectra are found to match the experimental data, and the lattice depths returned by the model in the cases of blue- and red-detuned lattices of similar depths, for the two cases where this comparison is available, agree well with each other. We can thus be relatively confident that, as stated above, the model developed above allows for a good understanding of the localization process. However, a closer look at the data reveals the presence of several discrepancies, between the experimental data and the numerical predictions, but also between experimental data taken for blue and

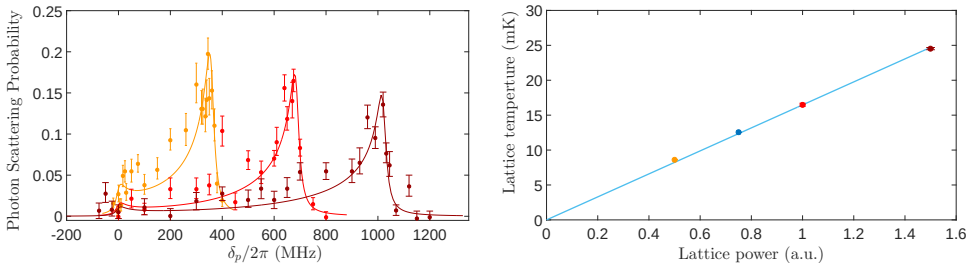

Figure 11.17: (a) Spectra corresponding to lattice depths of $\sim$ 8.6mK (yellow circles), 17 mK (red circles), and 24.5 mK (brown circles). The solid lines are the fit to the two-level adjusted model described above. The data was taken with a probe power of 100 μW (measured before the vacuum chamber) (b) The values of lattice depths retrieved from the fit of the spectra shown on the figure on the left are plotted against the measured lattice power. The solid line is a linear fit to the data and shows a $\pm 2.7\%$ agreement with the experimental data.

red detuned lattices of identical depths. Several reasons can be pointed out in order to understand these differences, and they are reviewed below.

11.4.3.1 Possible reasons explaining the imperfect match between the analytical model and the experimental data

1. As explained above in this chapter, the effeective two-level atom model used to analyze the experimental data does not take into account the oscillatory motion of the ion in the potential. Further analysis using the full three-level atom model would be necessary.

2. The assumption that the ion's position or energy can be described by a Boltzmann distribution is, strictly speaking, not true; in the case where the lattice ramp up is truly adiabatic, the analysis made in [64] shows that the energy is not thermally distributed in the lattice site, even though it is so in the loose axial Paul trap potential. Discrepancies we observe between the theoretical predictions and experimental data could therefore be an indication of the non-thermal nature of the ion's motion inside the lattice.

3. As discussed previously, for the highest lattice depths ($T_{latt} \sim 17$ mK and 25 mK), the ramp-up cannot be considered truly adiabatic. Molecular dynamics simulations shown in [64] show that the energy distribution then deviates from the one expected in the case of an adiabatic ramp-up. It is difficult to probe this effect in our simulations, since there is no analytical expression of the energy distribution in cases of non-adiabatic ramp-up, but this effect should be integrated in future and more refined numerical simulations.

4. As shown also in [64], it is of utmost importance that any residual axial micromotion be minimized, since micromotion-induced off-resonant parametric and on-resonance driven resonances can otherwise be excited and strongly alter the observed spectra. While axial micromotion was compensated as well as possible [64], some remaining excess micromotion could affect the spectra.

5. In a given sequence, the lattice is ramped up for 2 μs, held high for 1 μs and probing takes place within the last 0.5 μs of the lattice high-time. Therefore, there is a non-negligible probability for lattice-induced excitation *before* probing takes place, and this effect is expected to be more pronounced for an ion pinned at an antinode in a red-detuned lattice, than for an ion placed in a blue-detuned lattice. However, we checked that this effect alone does not alter the signals we measure - at least not in an observable extent, but it is yet to be assessed if, combined with the other possible causes listed here, this could lead to the differences we observe between data taken in blue and red-detuned lattices of identical depths.

6. Finally, the frequency-dependent finesse of the optical cavity used to generate the optical lattice could also play a role in the observed differences. In [80], measurement of the finesse at 850 nm was performed and yielded a value of $\mathcal{F} \simeq 4000$, whereas the finesse at 866 nm is equal to $\mathcal{F} = 3000 \pm 200$ [53]. In our case, the wavelength of the blue-detuned lattice is $\simeq 864$ nm, while that

of the red-detuned lattice is $\simeq$ 868 nm, which, assuming that the finesse varies linearly within the range of wavelengths from 850 nm to 868 nm, corresponds to a change of $\sim$ 250. Assuming that this variation can essentially be traced back to a change in the input coupler's transmission, this means that for an identical optical lattice power injected inside the optical cavity, the blue-detuned lattice is deeper than the red-detuned lattice, by a factor $\sim$ 10 %.

11.4.3.2 Comparison of errors given by the model presented section 9.2 or directly by the spread in recorded CCD counts

As pointed out in chapter 9, the detection and imaging system has a very low detection efficiency, and this results in the rather large error bars accompanying the experimental data. Indeed, in a typical measured spectrum, each experimental data point corresponds to a set of 30 images, and as mentioned earlier, this corresponds at most to about 90 photons. The low number of images per experimental point, and the low number of detected photons per image both naturally lead to a strong dispersion of the measured fluorescence between each image. However, analyzing the workings of the detection setup as done in section 9.2 leads to a reduction of the uncertainty on the results. This is shown on fig. 11.18, where the spectrum corresponding to a red-detuned lattice of $T_{latt} \simeq 24.5$ mK is presented with, on the left, error bars simply accounting for the aforementioned dispersion in the number of detected photons between each image, and on the right, error bars calculated by the model presented in section 9.2 by using the total number of CCD counts of the 30 images. This reduction

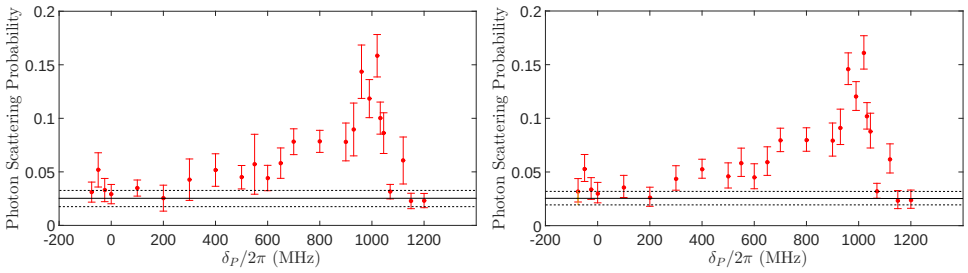

Figure 11.18: (a)Spectrum corresponding to an ion localized in a 24.5 mK lattice, analyzed without the detection analysis model presented in section 9.2. (b) Spectrum corresponding to an ion localized in a 24.5 mK lattice, analyzed with the detection analysis model presented in section 9.2. In both graphs, the black solid line indicate the background signal from the lattice and the black dashed lines the uncertainty on its value.

of the uncertainty on the results can be understood as the consequence of the knowledge used in calculating them - essentially, we measured the exact values of P_{det}, $\bar{N}_c$ and σ_c -, whereas in the case of error bars simply estimated from the dispersion of the results, we actually assume no specific knowledge on the detection setup.

Chapter 12

Outlook and conclusion

12.1 Shelving

As mentioned in section 11.4.3, due to the low detection efficiency of the detection system only a few tens of photons are typically detected per image, and this results in large error bars. A way to improve drastically the detection efficiency and hence the data acquisition time is to use a shelving technique similar to the one described in, e.g. [12]. The relevant diagram of the energy levels is shown in the fig. 12.1. The

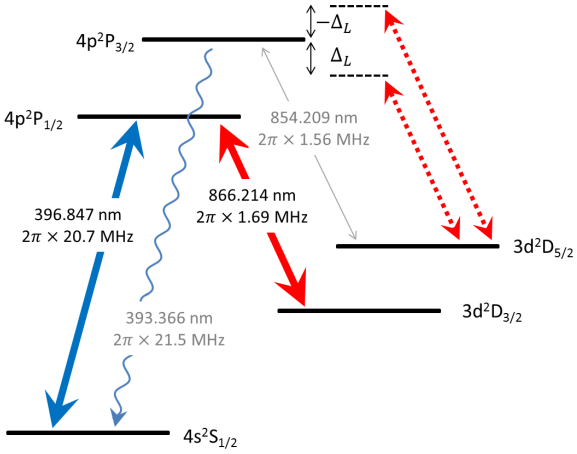

Figure 12.1: Diagram of the relevant energy levels used to perform a shelving experiment in order to detect the photon scattering probability from the lattice with a near unit efficiency.

idea of the scheme is the following: the ion is prepared in the $m_J = +5/2$ Zeeman substate of the $3d^2D_{5/2}$ state and optically trapped by applying a far-detuned standing wave on the $3d^2D_{5/2}$ to $4p^2P_{3/2}$ transition at 854 nm. The Doppler-cooling and repumper lasers presented in the previous sections are continously applied, such that the emission of a photon from the $P_{3/2}$ state to the $S_{1/2}$ state leads to the ion cycling within the three levels $S_{1/2}$, $P_{1/2}$ and $D_{3/2}$. Due to the high scattering rate on the

$P_{1/2}$ to $S_{1/2}$ cooling transition, a high number of photons could therefore be emitted following the scattering of a photon scattered by the probe, bringing the detection efficiency effectively close to unity provided one monitors the ion's fluorescence for a long enough time. As evoked in section 11.4.3, another benefit could come from the expected slightly higher value of the finesse of the optical cavity at 854 nm, and therefore the possibility to create deeper optical lattices with the same input power.

12.2 Probing non-thermal motion

The results presented in the previous chapter may already indicate that this method allows for determining if the ion position distribution inside the optical lattice well is thermal or not. One could go a bit further, and ask oneself what one would observe in the case of an ion excited in a strongly non-thermal motional state. As a simple example, we look at the spectrum produced by an ion having a given *energy* - as opposed to a given temperature, the case considered throughout the previous chapter. The result of a simulation using the model of an oscillating three-level ion is shown on fig. 12.2, for a red-detuned lattice 24.5 mK deep and for two different ion energies corresponding to half the lattice depth, and 90% of the lattice depth, respectively. The spectra are "reversed" compared to the previous ones, they reflect the probability distribution $P(kz|E)dkz$ calculated in section 11.2.2.2. For the highest values of lattice depth - i.e $\sim$ 25 mK, the oscillation frequency at the bottom of the lattice well is close to 4 MHz, and thus is nearly equal to the rf frequency of the Paul trap Ω_{rf}. In principle, the micromotion was carefully compensated for these experiments, but, as mentioned in the section 11.4.3 , any residual axial micromotion can have dramatic consequences on the localization signal [64], and could drive parametric resonances of the ion inside the lattice well. Since only the ions with the lowest energies have an oscillation frequency matching the resonance condition, such parametric resonance mechanism would only drive a small fraction of the ions, and could therefore lead to a "squeezing" of the energy distribution, which might, under ideal conditions, be reflected in spectra similar to the ones shown in fig. 12.2.

12.3 Two ions in a hybrid trap

A natural extension of the experiments presented in the previous chapter is the spectroscopy of two ions trapped in an optical lattice. In this case it could be possible to visualize the transition from the regime where the effect of the lattice potential override that of the Coulomb force - the case considered in this thesis, and in which the ions behave as independent entities -, to a regime where the Coulomb interaction between the ions dominates. This transition occurs for equal Paul trap axial frequency of and lattice oscillation frequency $\omega_z = \omega_l$. For an axial frequency of the potential of the Paul trap of $\sim$ 80 kHz (inter-ion distance $d = \left(\frac{e^2}{2\pi\epsilon_0 m\omega_z^2}\right)^{1/3} \sim 15$ μm) this corresponds to a lattice depth $T_{latt} \sim 1.2 \times 10^{-2}$ mK and would therefore be difficult to observe, since the associated frequency shift would be on the order of 3 MHz, much less than the natural width of the transition. For an axial frequency of 1 MHz (inter-ion distance ~ 9 μm), the lattice depth at which $\omega_z = \omega_l$ is 1.8 mK corresponding to a shift of $\simeq$ 75 MHz. The transition from $\omega_z > \omega_l$ to $\omega_z < \omega_l$ as we

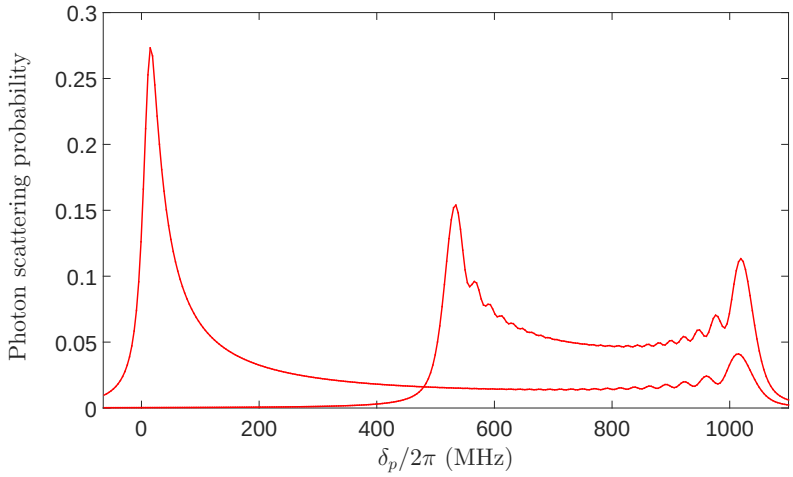

Figure 12.2: Simulated spectra using the model of an oscillating three-level ion, in the case of a red-detuned lattice with $T_{latt} = 24.5$ mK, and corresponding to an ion of a definite energy, equal to $0.9U_{latt}$ (maximum of scattering for $\delta_P \sim 0$ MHz) and to $0.5U_{latt}$.

ramp up the lattice should therefore be observable, and the two ions independently observable on our imaging system. In fig. 12.4 we look at the expected spectra for two ions placed in a red-detuned optical lattice, in two different situations:

1. shallow lattice: two ions confined via the Coulomb interaction, Doppler-cooled to 0.5 mK, and with $\omega_l < \omega_z$, and such that one ion is placed at a node of the lattice, and the other one at an antinode (fig. 12.3a).

2. deep lattice: two ions pinned at the antinodes of the lattice (fig. 12.3b).

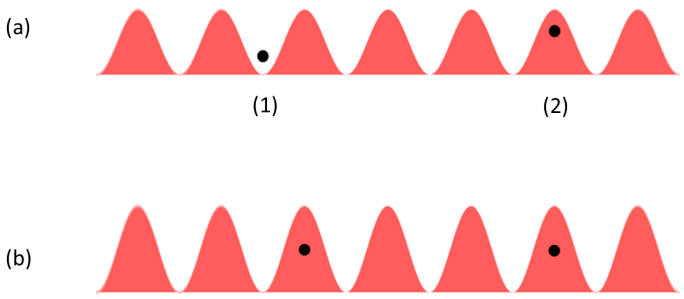

Figure 12.3: (a) Two ions pinned by the Coulomb force, and placed at a node (1) and at an antinode (2) of a red-detuned optical lattice. (b) Two ions pinned at the antinode of the red-detuned lattice.

As shown on fig. 12.4, the difference in regimes should be readily observable with the parameters chosen here. This method could therefore be used as a starting point for experiments exploring the constrained motion of ions placed in an optical lattice, and,

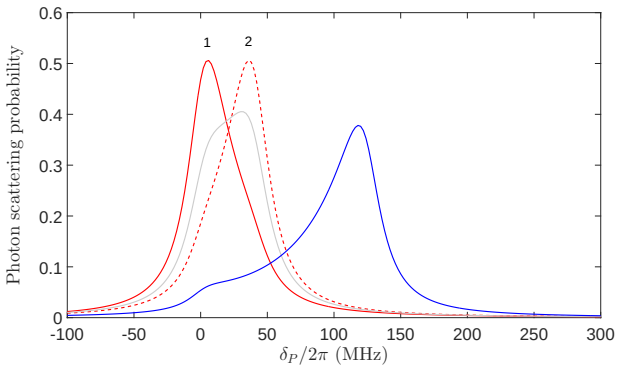

Figure 12.4: Simulated spectra using the adjusted two-level model for two ions placed in a red-detuned optical lattice of varying depths, and in a DC axial potential with secular frequency 1 MHz. The depth at which the oscillation frequency inside the optical lattice matches that of the axial trap frequency is 1.8 mK. Red, solid line: ion Doppler cooled to 0.5 mK, placed at the node of a 1 mK optical lattice. Red, dashed line: ion Doppler cooled to 0.5 mK, placed at the antinode of a 1 mK optical lattice. The numbers (1) and (2) refer to the schematic on fig. 12.3. Blue: one ion placed in a 3 mK optical lattice (in this case the ion is localized). Grey: one delocalized ion in a 1 mK optical lattice, shown here for reference.

along with experiments aiming at measuring the energy distribution of ions localized in a lattice well, provide an additional characterization of the optical lattice.

12.4 Conclusion

In conclusion, we have demonstrated a method for spectroscopically probing an ion placed in an optical lattice which complements the previous methods used in the group and gives further evidence of the pinning of a trapped ion in an optical lattice. We have built an analytical model which takes into account the level structure of the $^{40}Ca^{+}$ ion, and assumes that the ion distribution of energy and position can be described by a Boltzmann distribution. We find that this model gives both a satisfying qualitative and quantitative agreement with the experimental data, by reproducing the shape of the spectra, and by predicting scattering probabilities and lattice depths consistent with the measured ones.
Comparing the ion's temperature in optical lattices of identical depth but different sign of detuning, we find that the ion seems hotter in red-detuned lattices than in blue-detuned lattices, and in the case of the 8.5 mK deep lattice, that the measured ion temperatures are inconsistent with each other. Additionally, we find that the scattering probabilities are consistently higher than the expected values, and this effect seems to be stronger at smaller lattice depths. Further analysis is required to understand these discrepancies between the theory and the experimental data, and a few ideas for further investigations are given in section 11.4.3.
In addition, the method also provides a precise calibration of the lattice depth as a function of the lattice input power, owing to the large frequency shift of $\sim$ 42

MHz/mK of the peak of maximum scattering probability.
While the uncertainties in the measurements presented here are relatively large due to the low detection efficiency, combining this method with shelving should allow for drastically improved precision in the measurements of the spectra allowing, for example, probing of non-thermal energy distributions and the competition between the lattice-induced and Coulomb forces.

Chapter 13

Conclusion

This thesis consists of three projects which take place within the broader scope of experiments using Ion Coulomb crystals as a tool for quantum information and quantum simulations of many-body physics models.

In close connection with prospects of using two-component crystals for the realization of a quantum memory [86, 97], a new frequency-doubled source was developed for Doppler cooling of various isotopes of Ca^+. The frequency doubled source is described in chapter 7. It consists of a source of light at 794 nm generated by a tapered amplified Toptica TA Pro diode laser, subsequently frequency doubled in a non linear ppKTP crystal placed inside an optical ring cavity in a bow-tie configuration. The single-pass conversion coefficient of (0.5 - 0.7) $\%W^{-1}$ was measured with a beam with a waist of 35 μm. The non-uniformity of this coefficient over the crystal surface is attributed to defects in the poling of the crystal, and indicates the presence of good and bad spots to perform SHG. By placing the crystal in a bow-tie cavity of finesse $\sim$ 48 and corresponding enhancement factor $P_{cav}/P_{in} \sim 30$, a stable output of 60 mW of frequency-doubled light could be generated by using an input power of 190 mW at the fundamental frequency. Correcting for the imperfect mode-matching of the input field to the cavity mode, this corresponds to a doubling efficiency of $\sim$ 43 %. At higher input powers, the observation of instabilities in the frequency-doubled output are attributed to various effects, such as thermal effects due to the strong UV absorption inside the crystal, and the presence of BLIIRA.

In chapter 9, we present an analysis of the detection system which aims at quantifying as accurately as possible the scattering probability given the number of recorded CCD counts. To do so, we model the probabilistic nature of the detection of a photon onto the imaging intensifier by using a binomial law, and the distribution of counts on the CCD camera for a detected photon with a normal distribution. Applying this model to the real setup imposes to measure the distribution of CCD counts per detected photon, which we performed by measuring the histogram of CCD counts for an average of $\gtrsim 1$ detected photons. From this we were able to infer the detection efficiency of the setup which we found to be equal to $(1.67 \pm 0.01) \times 10^{-4}$. Our model allows us to rigorously calculate the probability $P(N_c^{tot}|N_p^E)$ to detect N_c^{tot} CCD counts given a number N_p^E of emitted photons, but is not directly suited to estimate the most

probable number of emitted photons given a measured number of CCD counts. To obtain this information, we build an effective probability distribution $P^{eff}(N_p^E|N_c^{tot})$ by selecting values of $P(N_c^{tot}|N_p^E)$ corresponding to a fixed N_c^{tot}. Comparing the behaviors of these distributions enables us to obtain a better understanding of the detection mechanism and to quantify our (lack of) knowledge on the number of emitted photons given a certain number of recorded CCD counts.

In the chapter 11 we present the results on the localization spectroscopy of a single ion inside an optical lattice. In a typical experiment, an ion is trapped in a linear rf Paul trap and placed inside the mode of an optical cavity whose axis coincides with that of the trap. An intracavity standing wave far-detuned from the $D_{3/2} \rightarrow P_{1/2}$ transition is adiabatically ramped-up, and the induced as Stark shift of the $D_{3/2}$ and $P_{1/2}$ levels is measured by monitoring the fluorescence on the $P_{1/2} \rightarrow S_{1/2}$ transition resulting from the interaction with a probe field applied from the side of the cavity. Measuring the spectrum provides an unambiguous signature that the ion is localized inside the optical lattice, and can in addition inform on the ion dynamics inside the lattice.
We measured the spectra corresponding to an ion placed in optical lattices ~ 8.6 mK, 12.5 mK, 17 mK and 24.5 mK deep. In order to interpret the spectra we have developed simple analytical models assuming a thermal position distribution inside the optical lattice. The spectra overall agree well with the models describing the ion as a two- and three-level system, indicating that a satisfying description of the physics can be given by assuming a thermal distribution of the ion's position inside the optical lattice. In two cases - lattice depths of 8.6 mK and 17 mK -, we were able to compare the spectra for an ion trapped in a blue- and red-detuned lattices of identical depths. In the 17 mK deep lattice, the ion temperatures estimated by fitting the experimental data with the model agree with each other, while it is not the case for the 8.6 mK deep lattice. Moreover, the model seems to predict scattering probabilities consistently lower than the measured ones. The reason for these discrepancies is not well understood at the time of writing, but several reasons which could explain them are given.
In the last chapter, we give a few suggestions in order to improve the experiment, and apply the method to address other experimental questions. First, we indicate in section 12.1how a shelving method could be used at a profit to drastically enhance the detection efficiency. By using this method, increased precision on the results could be obtained, and could allow for, e.g., testing how well the ion dynamics inside the optical lattice can be characterized. In the case of two ions localized inside the optical lattice, the method presented in this thesis could, in principle, enable to visualize the transition between a situation where the force induced by the optical lattice dominates and a situation where the Coulomb force dominates, in close connection to studies of heat transport in chains of ions [46, 48, 49], and the study of structural transitions of ion chains in optical potentials [57, 58]. In the case of an ion trapped inside a harmonic potential, raising the optical lattice adiabatically in principle only affects the distance between two consecutive energy levels, but does not change the populations in the different energy levels. It follows that, provided the ion's distribution is thermal, measuring the ion temperature inside the optical lattice directly informs on the temperature of the ion outside the optical lattice, with an improved precision set

by the stretching or the energy levels. Using the shelving method to measure more precisely the spectrum of the ion could therefore turn this method into a scheme for accurate measurement of the ion temperature inside the Paul trap.

Appendices

Appendix A

The $^{40}Ca^{+}$ ion

A.1 Abundance of Ca-isotopes

Isotope	Abundance
40	96.941%
42	0.647%
43	0.135%
44	2.086%
46	0.004%
48	0.187%

Table A.1: Abundance of the stable isotopes of calcium [138].

A.2 Transition wavelengths and decay rates

Transition	Wavelength λ	$\Gamma = 2\gamma$	I_{sat} [mW/cm^2]
$4S_{1/2}$-$4P_{1/2}$	396.847 nm	$2\pi\times$ 20.7 MHz	43.3
$4S_{1/2}$-$4P_{3/2}$	393.366 nm	$2\pi\times$ 21.5 MHz	46.2
$3D_{3/2}$-$4P_{1/2}$	866.214 nm	$2\pi\times$ 1.69 MHz	0.34
$3D_{3/2}$-$4P_{3/2}$	849.802 nm	$2\pi\times$ 0.176 MHz	0.038
$3D_{5/2}$-$4P_{3/2}$	854.209 nm	$2\pi\times$ 1.56 MHz	0.33
$4S_{1/2}$-$3D_{3/2}$	732.389 nm	$2\pi\times$ 0.16 Hz	5.3×10^{-8}
$4S_{1/2}$-$3D_{5/2}$	729.147 nm	$2\pi\times$ 0.17 Hz	5.7×10^{-8}

Table A.2: Data for transitions in $^{40}Ca^{+}$. The first five transitions are dipole-allowed while the last two are quadropole transitions. Transition wavelengths are measured in air [75, 76]. Γ is the transition rate [75, 76]. Saturation intensities are calculated according to $I_{\text{sat}} = \frac{\hbar\Gamma\omega^3}{12\pi c^2}$ [139], using the relevant transition rate Γ and transition frequency ω.

A.3 Clebsch-Gordan coefficients

The coupling strengths for dipole-allowed transitions between the various sub-levels are characterized by the values of Γ given in Table A.2 and the Clebsch-Gordan coefficients (see, e.g., Ref. [140] for a definition), which are listed in Tables A.3–A.5.

	$4S_{1/2}, -1/2$	$4S_{1/2}, +1/2$
$4P_{1/2}, -1/2$	$-\sqrt{1/3}$	$\sqrt{2/3}$
$4P_{1/2}, +1/2$	$-\sqrt{2/3}$	$\sqrt{1/3}$
$4P_{3/2}, -3/2$	1	-
$4P_{3/2}, -1/2$	$\sqrt{2/3}$	$\sqrt{1/3}$
$4P_{3/2}, +1/2$	$\sqrt{1/3}$	$\sqrt{2/3}$
$4P_{3/2}, +3/2$	-	1

Table A.3: Clebsch-Gordan coefficients for transitions between the $4S_{1/2}$ state and the $4P_{1/2}$ and $4P_{3/2}$ states.

	$3D_{3/2}, -3/2$	$3D_{3/2}, -1/2$	$3D_{3/2}, +1/2$	$3D_{3/2}, +3/2$
$4P_{1/2}, -1/2$	$\sqrt{1/2}$	$-\sqrt{1/3}$	$\sqrt{1/6}$	-
$4P_{1/2}, +1/2$	-	$\sqrt{1/6}$	$-\sqrt{1/3}$	$\sqrt{1/2}$
$4P_{3/2}, -3/2$	$-\sqrt{3/5}$	$\sqrt{2/5}$	-	-
$4P_{3/2}, -1/2$	$-\sqrt{2/5}$	$-\sqrt{1/15}$	$\sqrt{8/15}$	-
$4P_{3/2}, +1/2$	-	$-\sqrt{8/15}$	$\sqrt{1/15}$	$\sqrt{2/5}$
$4P_{3/2}, +3/2$	-	-	$-\sqrt{2/5}$	$\sqrt{3/5}$

Table A.4: Clebsch-Gordan coefficients for transitions between the $3D_{3/2}$ state and the $4P_{1/2}$ and $4P_{3/2}$ states.

	$4P_{3/2}, -3/2$	$4P_{3/2}, -1/2$	$4P_{3/2}, +1/2$	$4P_{3/2}, +3/2$
$3D_{5/2}, -5/2$	$\sqrt{2/3}$	-	-	-
$3D_{5/2}, -3/2$	$-\sqrt{4/15}$	$\sqrt{2/5}$	-	-
$3D_{5/2}, -1/2$	$\sqrt{1/15}$	$-\sqrt{2/5}$	$\sqrt{1/5}$	-
$3D_{5/2}, +1/2$	-	$\sqrt{1/5}$	$-\sqrt{2/5}$	$\sqrt{1/15}$
$3D_{5/2}, +3/2$	-	-	$\sqrt{2/5}$	$-\sqrt{4/15}$
$3D_{5/2}, +5/2$	-	-	-	$\sqrt{2/3}$

Table A.5: Clebsch-Gordan coefficients for transitions between the $3D_{5/2}$ state and the $4P_{3/2}$ state.

A.4 Zeeman-splitting

Zeeman-substates will experience an energy shift, ΔE_B, when a magnetic field, B, is present, which is in general given by [139]:

$$\Delta E_B = m_j g_J \mu_B B \tag{A.1}$$

where m_J is the magnetic quantum number, μ_B is the Bohr magneton, B is the magnetic field strength and g_J is the Landé g-factor:

$$g_J = 1 + \frac{J(J+1) + S(S+1) - L(L+1)}{2J(J+1)} \tag{A.2}$$

where L, S and J are the quantum numbers corresponding to the angular momentum, the electric spin and the total angular momentum, respectively. Values of g_J are listed below for the relevant states of the $^{40}Ca^+$ ion.

State	L	S	J	g_J
$4S_{1/2}$	0	1/2	1/2	2
$4P_{1/2}$	1	1/2	1/2	2/3
$4P_{3/2}$	1	1/2	3/2	4/3
$3D_{3/2}$	2	1/2	3/2	4/5
$3D_{5/2}$	2	1/2	5/2	6/5

Table A.6: Values of g_J for the relevant levels of the $^{40}Ca^+$ ion.

A.5 Rabi frequency

The coupling strength of a particular (dipole-allowed) transition for an intensity I of the coupling field is characterized by the Rabi frequency, which for a transition between the Zeeman-substates $|g\rangle$ and $|e\rangle$ is given by [139]:

$$\Omega_{ge} = a_{ge} \sqrt{\frac{3\pi c^2 \Gamma}{2\hbar\omega^3}} \sqrt{I} \tag{A.3}$$

where Γ and ω are the transition rate and resonance frequency of the electronic transition (see table A.2), and a_{ge} is the Clebsch-Gordan coefficient for the considered Zeeman-substates.

Appendix B

Complete elliptic integral of the first kind

In section 11.2.2, we used the complete elliptic integral of the first kind. With our notations, this integral is defined as:

$$\mathcal{K}(k^2) = \int_0^{\phi} \frac{d\theta}{\sqrt{1 - k^2 \sin^2 \theta}} = \int_0^1 \frac{dx}{\sqrt{(1 - x^2)(1 - k^2 x^2}} \tag{B.1}$$

where $\phi \in [0, \frac{\pi}{2}]$, $|k| < 1$ and $x = \sin \phi$. Note that this convention differs from the one used, e.g. in [141] or in [137], where the argument of the integral is the elliptic modulus k, not its square (as is the case here).

Appendix C

Calculation of the density of states for the ion oscillating inside the sinusoidal potential

We consider the situation depicted in section 11.2.2: a particle of energy E, mass m and position z oscillating inside a sinusoidal potential of depth U_{latt}, and wave-vector k such that the oscillation frequency of the particle at the bottom of the potential reads $\omega_l = \sqrt{\frac{2k^2 U_{latt}}{m}}$. The expression relating the energy of the particle to its position and velocity inside the potential well was given in eq. ((11.21)), and we recall it here for clarity:

$$(k\dot{z}(t))^2 + \omega_l^2 \sin^2(kz(t)) = \frac{2k^2}{m} E = \omega_l^2 \frac{E}{U_{latt}} \tag{C.1}$$

By isolating $k\dot{z}(t)$ in the above expression, we obtain:

$$k\dot{z}(t) = \omega_l \sqrt{\frac{E}{U_{latt}} - \sin^2(kz)} \tag{C.2}$$

This constitutes the equation for the trajectory of the ion in the upper quadrant in the phase space $\{kz, k\dot{z}\}$. In the lower quadrant, we have:

$$k\dot{z}(t) = -\omega_l \sqrt{\frac{E}{U_{latt}} - \sin^2(kz)} \tag{C.3}$$

Such trajectories are shown on fig. C.1(a). Each trajectory corresponds to a constant energy E. We want to calculate the density of states $\Omega(E)dE$, i.e. the number of cells $dkzdk\dot{z}$ contained between the trajectories corresponding to E and $E+dE$. This corresponds to the infinitesimal surface delimited by two such trajectories (see fig. C.1(b)) and is formally equal to:

$$\Omega(E)dE = \int_{E < \frac{m(k\dot{z}(t))^2}{2k^2} + U_{latt}\sin^2(k\dot{z}) < E+dE} dkzdk\dot{z} \tag{C.4}$$

Using eq. (C.2), we can rewrite $dk\dot{z}$ as:

$$dk\dot{z} = \frac{d}{dE}\left[\omega_l \sqrt{\frac{E}{U_{latt}} - \sin^2(kz)}\right] dE \tag{C.5}$$

$$= \frac{\omega_l}{2U_{latt}} \frac{1}{\sqrt{\frac{E}{U_{latt}} - \sin^2(kz)}} dE \tag{C.6}$$

and use it in eq. (C.4), which gives:

$$\Omega(E)dE = 2\frac{\omega_l}{U_{latt}} \left[\int_0^{kz_{max}} dkz \frac{1}{\sqrt{\frac{E}{U_{latt}} - \sin^2(kz)}}\right] dE \tag{C.7}$$

where the factor of 2 comes from the fact that we calculate the surface in the upper-right quadrant and multiply it by four to get the total surface, since the trajectory is symmetric about the x and y axis. kz_{max} is the upper bound for the motion inside the potential, and is $\leq \pi/2$ for $E/U_{latt} \leq 1$, and is equal to $\pi/2$ otherwise.

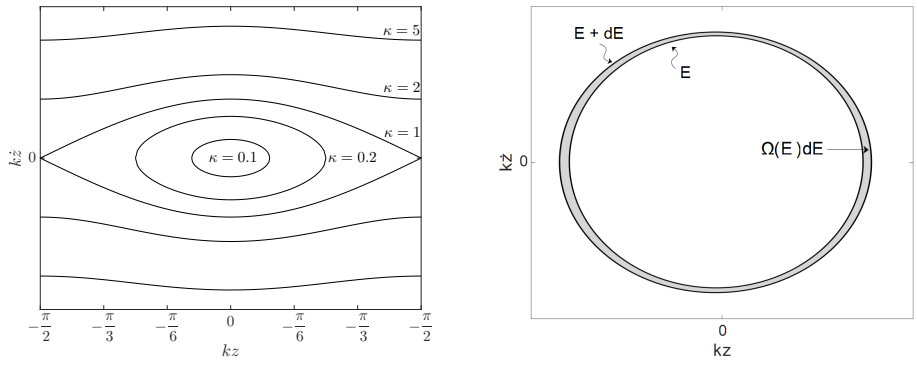

(a) (b)

Figure C.1: (a) Trajectories of constant energies in phase-space, for different values of $\kappa = E/U_{latt}$. (b) Two trajectories corresponding to energies E and $E + dE$. The grey area corresponds to the density of states $\Omega(E)dE$.

Bibliography

[1] P. K. Ghosh, *Ion Traps* (Oxford University Press, New York, 1995).

[2] E. N. Fortson, F. G. Major and H. G. Dehmelt, *Ultrahigh Resolution* $\Delta F = 0, \pm 1$ $(\mathrm{He}^3)^+$ *Hfs Spectra by an Ion-Storage Collision Technique*, Phys. Rev. Lett. **16**, 221 (1966),
URL link.

[3] H. A. Schuessler, E. N. Fortson and H. G. Dehmelt, *Hyperfine Structure of the Ground State of* $^3\mathrm{He}^+$ *by the Ion-Storage Exchange-Collision Technique*, Phys. Rev. **187**, 5 (1969),
URL link.

[4] D. Wineland, P. Ekstrom and H. Dehmelt, *Monoelectron Oscillator*, Phys. Rev. Lett. **31**, 1279 (1973),
URL link.

[5] R. S. Van Dyck, P. B. Schwinberg and H. G. Dehmelt, *New high-precision comparison of electron and positron g factors*, Phys. Rev. Lett. **59**, 26 (1987),
URL link.

[6] T. Hänsch and A. Schawlow, *Cooling of gases by laser radiation*, Optics Communications **13**, 68 (1975),
URL link.

[7] D. Wineland and H. Dehmelt, *Proposed* $10^{14}\delta\nu < \nu$ *frequency resolution laser spectroscopy on* Tl^+ *mono-ion oscillator*, Bull. Am. Phys. Soc. **20**, 637 (1975).

[8] W. Neuhauser, M. Hohenstatt, P. E. Toschek and H. Dehmelt, *Localized visible* Ba^+ *mono-ion oscillator*, Phys. Rev. A **22**, 1137 (1980),
URL link.

[9] J. C. Bergquist, R. G. Hulet, W. M. Itano and D. J. Wineland, *Observation of Quantum Jumps in a Single Atom*, Phys. Rev. Lett. **57**, 1699 (1986),
URL link.

[10] W. Nagourney, J. Sandberg and H. Dehmelt, *Shelved optical electron amplifier: Observation of quantum jumps*, Phys. Rev. Lett. **56**, 2797 (1986),
URL link.

[11] T. Sauter, W. Neuhauser, R. Blatt and P. E. Toschek, *Observation of Quantum Jumps*, Phys. Rev. Lett. **57**, 1696 (1986),
URL link.

[12] R. Blatt and P. Zoller, *Quantum jumps in atomic systems*, European Journal of Physics **9**, 250 (1988),
URL link.

[13] F. Diedrich, J. C. Bergquist, W. M. Itano and D. J. Wineland, *Laser Cooling to the Zero-Point Energy of Motion*, Phys. Rev. Lett. **62**, 403 (1989),
URL link.

[14] C. Monroe, D. M. Meekhof, B. E. King, S. R. Jefferts, W. M. Itano, D. J. Wineland and P. Gould, *Resolved-Sideband Raman Cooling of a Bound Atom to the 3D Zero-Point Energy*, Phys. Rev. Lett. **75**, 4011 (1995),
URL link.

[15] D. Leibfried, R. Blatt, C. Monroe and D. Wineland, *Quantum dynamics of single trapped ions*, Rev. Mod. Phys. **75**, 281 (2003),
URL link.

[16] D. J. Wineland, J. C. Bergquist, W. M. Itano, J. J. Bollinger and C. H. Manney, *Atomic-Ion Coulomb Clusters in an Ion Trap*, Physical Review Letters **59**, 2935 (1987).

[17] F. Diedrich, E. Peik, J. M. Chen, W. Quint and H. Walther, *Observation of a Phase Transition of Stored Laser-Cooled Ions*, Phys. Rev. Lett. **59**, 2931 (1987),
URL link.

[18] J. I. Cirac and P. Zoller, *Quantum Computations with Cold Trapped Ions*, Phys. Rev. Lett. **74**, 4091 (1995),
URL link.

[19] C. Monroe, D. M. Meekhof, B. E. King, W. M. Itano and D. J. Wineland, *Demonstration of a Fundamental Quantum Logic Gate*, Phys. Rev. Lett. **75**, 4714 (1995),
URL link.

[20] D. Leibfried, B. DeMarco, V. Meyer, D. Lucas, M. Barrett, J. Britton, W. M. Itano, B. Jelenkovic, C. Langer, T. Rosenband and D. J. Wineland, *Experimental demonstration of a robust, high-fidelity geometric two ion-qubit phase gate*, Nature **422**, 412 (2003),
URL link.

[21] C. Monroe, D. M. Meekhof, B. E. King and D. J. Wineland, *A "Schrödinger Cat" Superposition State of an Atom*, Science **272**, 1131 (1996),
URL link, `http://www.sciencemag.org/content/272/5265/1131.full.pdf`.

[22] D. Leibfried, E. Knill, S. Seidelin, J. Britton, R. B. Blakestad, J. Chiaverini, D. B. Hume, W. M. Itano, J. D. Jost, C. Langer, R. Ozeri, R. Reichle and D. J. Wineland, *Creation of a six-atom "Schrodinger cat" state*, Nature **438**,

639 (2005),
URL link.

[23] M. Riebe, H. Haffner, C. F. Roos, W. Hansel, J. Benhelm, G. P. T. Lancaster, T. W. Korber, C. Becher, F. Schmidt-Kaler, D. F. V. James and R. Blatt, *Deterministic quantum teleportation with atoms*, Nature **429**, 734 (2004),
URL link.

[24] P. O. Schmidt, T. Rosenband, C. Langer, W. M. Itano, J. C. Bergquist and D. J. Wineland, *Spectroscopy Using Quantum Logic*, Science **309**, 749 (2005),
URL link, `http://www.sciencemag.org/content/309/5735/749.full.pdf`.

[25] J. Benhelm, G. Kirchmair, C. F. Roos and R. Blatt, *Towards fault-tolerant quantum computing with trapped ions*, Nat Phys **4**, 463 (2008),
URL link.

[26] P. Schindler, J. T. Barreiro, T. Monz, V. Nebendahl, D. Nigg, M. Chwalla, M. Hennrich and R. Blatt, *Experimental Repetitive Quantum Error Correction*, Science **332**, 1059 (2011),
URL link, `http://www.sciencemag.org/content/332/6033/1059.full.pdf`.

[27] T. Monz, P. Schindler, J. T. Barreiro, M. Chwalla, D. Nigg, W. A. Coish, M. Harlander, W. Hänsel, M. Hennrich and R. Blatt, *14-Qubit Entanglement: Creation and Coherence*, Phys. Rev. Lett. **106**, 130506 (2011),
URL link.

[28] R. Blatt and C. F. Roos, *Quantum simulations with trapped ions*, Nat Phys **8**, 277 (2012),
URL link.

[29] T. W. B. Kibble, *Topology of cosmic domains and strings*, Journal of Physics A: Mathematical and General **9**, 1387 (1976),
URL link.

[30] W. H. Zurek, *Cosmological experiments in superfluid helium?*, Nature **317**, 505 (1985),
URL link.

[31] S. Ulm, J. Roß nagel, G. Jacob, C. Degünther, S. T. Dawkins, U. G. Poschinger, R. Nigmatullin, A. Retzker, M. B. Plenio, F. Schmidt-Kaler and K. Singer, *Observation of the Kibble-Zurek scaling law for defect formation in ion crystals*, Nat Commun **4**, (2013),
URL link.

[32] K. Pyka, J. Keller, H. L. Partner, R. Nigmatullin, T. Burgermeister, D. M. Meier, K. Kuhlmann, A. Retzker, M. B. Plenio, W. H. Zurek, A. del Campo and T. E. Mehlstäubler, *Topological defect formation and spontaneous symmetry breaking in ion Coulomb crystals*, Nat Commun **4**, (2013),
URL link.

[33] H. L. Partner, R. Nigmatullin, T. Burgermeister, K. Pyka, J. Keller, A. Retzker, M. B. Plenio and T. E. Mehlstäubler, *Dynamics of topological defects in ion Coulomb crystals*, New Journal of Physics **15**, 103013 (2013),
URL link.

[34] H. L. Partner, R. Nigmatullin, T. Burgermeister, J. Keller, K. Pyka, M. B. Plenio, A. Retzker, W. H. Zurek, A. del Campo and T. E. Mehlstäubler, *Structural phase transitions and topological defects in ion Coulomb crystals*, Physica B: Condensed Matter **460**, 114 (2015),
URL link, special Issue on Electronic Crystals (ECRYS-2014).

[35] D. Porras and J. I. Cirac, *Bose-Einstein Condensation and Strong-Correlation Behavior of Phonons in Ion Traps*, Phys. Rev. Lett. **93**, 263602 (2004),
URL link.

[36] D. Porras and J. I. Cirac, *Quantum Manipulation of Trapped Ions in Two Dimensional Coulomb Crystals*, Phys. Rev. Lett. **96**, 250501 (2006),
URL link.

[37] A. Friedenauer, H. Schmitz, J. T. Glueckert, D. Porras and T. Schaetz, *Simulating a quantum magnet with trapped ions*, Nat Phys **4**, 757 (2008),
URL link.

[38] K. Kim, M.-S. Chang, S. Korenblit, R. Islam, E. E. Edwards, J. K. Freericks, G.-D. Lin, L.-M. Duan and C. Monroe, *Quantum simulation of frustrated Ising spins with trapped ions*, Nature **465**, 590 (2010),
URL link.

[39] J. W. Britton, B. C. Sawyer, A. C. Keith, C.-C. J. Wang, J. K. Freericks, H. Uys, M. J. Biercuk and J. J. Bollinger, *Engineered two-dimensional Ising interactions in a trapped-ion quantum simulator with hundreds of spins*, Nature **484**, 489 (2012),
URL link.

[40] C. Schneider, D. Porras and T. Schaetz, *Experimental quantum simulations of many-body physics with trapped ions*, Reports on Progress in Physics **75**, 024401 (2012),
URL link.

[41] P. Richerme, Z.-X. Gong, A. Lee, C. Senko, J. Smith, M. Foss-Feig, S. Michalakis, A. V. Gorshkov and C. Monroe, *Non-local propagation of correlations in quantum systems with long-range interactions*, Nature **511**, 198 (2014),
URL link.

[42] P. Jurcevic, B. P. Lanyon, P. Hauke, C. Hempel, P. Zoller, R. Blatt and C. F. Roos, *Quasiparticle engineering and entanglement propagation in a quantum many-body system*, Nature **511**, 202 (2014),
URL link.

[43] Y. I. Frenkel and T. Kontorova, *The model of dislocation in solid body*, Zh. Eksp. Teor. Fiz **8** (1938).

[44] I. Garcìa-Mata, O. V. Zhirov and D. L. Shepelyansky, *Frenkel-Kontorova model with cold trapped ions*, The European Physical Journal D **41**, 325 (2007), URL link.

[45] A. Benassi, A. Vanossi and E. Tosatti, *Nanofriction in cold ion traps*, Nat Commun **2**, 236 (2011), URL link.

[46] T. Pruttivarasin, M. Ramm, I. Talukdar, A. Kreuter and H. Häffner, *Trapped ions in optical lattices for probing oscillator chain models*, New Journal of Physics **13**, 075012 (2011), URL link.

[47] A. Bylinskii, D. Gangloff and V. Vuletić, *Tuning friction atom-by-atom in an ion-crystal simulator*, Science **348**, 1115 (2015), URL link, `http://www.sciencemag.org/content/348/6239/1115.full.pdf`.

[48] A. Bermudez, M. Bruderer and M. B. Plenio, *Controlling and Measuring Quantum Transport of Heat in Trapped-Ion Crystals*, Phys. Rev. Lett. **111**, 040601 (2013), URL link.

[49] M. Ramm, T. Pruttivarasin and H. Häffner, *Energy transport in trapped ion chains*, New Journal of Physics **16**, 063062 (2014), URL link.

[50] S. Genway, W. Li, C. Ates, B. P. Lanyon and I. Lesanovsky, *Generalized Dicke Nonequilibrium Dynamics in Trapped Ions*, Phys. Rev. Lett. **112**, 023603 (2014), URL link.

[51] M. El Ghafar, P. Törmä, V. Savichev, E. Mayr, A. Zeiler and W. P. Schleich, *Dynamical Localization in the Paul Trap*, Phys. Rev. Lett. **78**, 4181 (1997), URL link.

[52] P. Horak, A. Dantan and M. Drewsen, *Optically induced structural phase transitions in ion Coulomb crystals*, Phys. Rev. A **86**, 043435 (2012), URL link.

[53] P. Herskind, *Cavity Quantum Electrodynamics with Ion Coulomb Crystals*, Ph.D. thesis, Danish National Research Foundation Center for Quantum Optics - Quantop Department of Physics and Astronomy, The University of Aarhus (2008).

[54] P. F. Herskind, A. Dantan, J. P. Marler, M. Albert and M. Drewsen, *Realization of collective strong coupling with ion Coulomb crystals in an optical cavity*, Nature Physics **5**, 494 (2009).

[55] R. B. Linnet, I. D. Leroux, M. Marciante, A. Dantan and M. Drewsen, *Pinning an Ion with an Intracavity Optical Lattice*, Phys. Rev. Lett. **109**, 233005 (2012), URL link.

[56] P. Bushev, A. Wilson, J. Eschner, C. Raab, F. Schmidt-Kaler, C. Becher and R. Blatt, *Forces between a Single Atom and Its Distant Mirror Image*, Phys. Rev. Lett. **92**, 223602 (2004),
URL link.

[57] C. Cormick and G. Morigi, *Structural Transitions of Ion Strings in Quantum Potentials*, Phys. Rev. Lett. **109**, 053003 (2012),
URL link.

[58] C. Cormick and G. Morigi, *Ion chains in high-finesse cavities*, Phys. Rev. A **87**, 013829 (2013),
URL link.

[59] T. Fogarty, C. Cormick, H. Landa, V. M. Stojanovic, E. Demler and G. Morigi, *Nano-friction in cavity quantum electrodynamics*, arXiv:1504.00275v1 .

[60] A. T. Grier, M. Cetina, F. Oručević and V. Vuletić, *Observation of Cold Collisions between Trapped Ions and Trapped Atoms*, Phys. Rev. Lett. **102**, 223201 (2009),
URL link.

[61] C. Zipkes, S. Palzer, C. Sias and M. Kohl, *A trapped single ion inside a Bose-Einstein condensate*, Nature **464**, 388 (2010),
URL link.

[62] S. Schmid, A. Härter and J. H. Denschlag, *Dynamics of a Cold Trapped Ion in a Bose-Einstein Condensate*, Phys. Rev. Lett. **105**, 133202 (2010),
URL link.

[63] M. Cetina, A. T. Grier and V. Vuletić, *Micromotion-Induced Limit to Atom-Ion Sympathetic Cooling in Paul Traps*, Phys. Rev. Lett. **109**, 253201 (2012),
URL link.

[64] R. B. Linnet, *Probing and controlling ion Coulomb crystals by optical cavity fields*, Ph.D. thesis, Danish National Research Foundation Center for Quantum Optics - Quantop Department of Physics and Astronomy, Aarhus University (2014).

[65] W. Paul, H. Reinhard and U. Von Zahn, *Das elektrische massenfilter als massenspektrometer und isotopentrenner*, Zeitschrift für Physik **152**, 143 (1958).

[66] W. Paul, *Electromagnetic traps for charged and neutral particles*, Rev. Mod. Phys. **62**, 531 (1990),
URL link.

[67] J. Prestage, G. J. Dick and L. Maleki, *New ion trap for frequency standard applications*, Journal of Applied Physics **66**, 1013 (1989).

[68] R. Grimm, M. Weidemüller and Y. B. Ovchinnikov, *Optical dipole traps for neutral atoms*, Advances in atomic, molecular, and optical physics **42**, 95 (2000).

[69] C. Cohen-Tannoudji, J. Dupont-Roc, G. Grynberg and P. Thickstun, *Atom-photon interactions: basic processes and applications* (Wiley Online Library, 1992).

[70] S. Stenholm, *The semiclassical theory of laser cooling*, Rev. Mod. Phys. **58**, 699 (1986),
URL link.

[71] C. Cohen-Tannoudji, *Atomic motion in laser light*, J. Dalibard, J.-M. Raimond and J. Zinn-Justin, editors, *Fundamental Systems in Quantum Optics, Proceedings of the Les Houches Summer School, Session LIII*, chapter 1 (Elsevier Science Publishers B.V., North-Holland, 1992).

[72] J. Eschner, G. Morigi, F. Schmidt-Kaler and R. Blatt, *Laser cooling of trapped ions*, J. Opt. Soc. Am. B **20**, 1003 (2003),
URL link.

[73] W. D. Phillips, *Nobel Lecture: Laser cooling and trapping of neutral atoms*, Rev. Mod. Phys. **70**, 721 (1998),
URL link.

[74] P. A. Barton, C. J. S. Donald, D. M. Lucas, D. A. Stevens, A. M. Steane and D. N. Stacey, *Measurement of the lifetime of the* $3d^2D_{5/2}$ *state in* $^{40}Ca^+$, Phys. Rev. A **62**, 032503 (2000),
URL link.

[75] D. James, *Quantum dynamics of cold trapped ions with application to quantum computation*, Applied Physics B **66**, 181 (1998),
URL link.

[76] A. Kramida, Yu. Ralchenko, J. Reader and and NIST ASD Team, NIST Atomic Spectra Database (ver. 5.2), [Online]. Available: http://physics.nist.gov/asd [2015, May 28]. National Institute of Standards and Technology, Gaithersburg, MD. (2014).

[77] W. M. Itano and D. J. Wineland, *Laser cooling of ions stored in harmonic and Penning traps*, Phys. Rev. A **25**, 35 (1982),
URL link.

[78] J. I. Cirac, L. J. Garay, R. Blatt, A. S. Parkins and P. Zoller, *Laser cooling of trapped ions: The influence of micromotion*, Phys. Rev. A **49**, 421 (1994),
URL link.

[79] D. J. Berkeland, J. D. Miller, J. C. Bergquist, W. M. Itano and D. J. Wineland, *Minimization of ion micromotion in a Paul trap*, Journal of Applied Physics **83**, 5025 (1998),
URL link.

[80] M. Albert, *A light-matter interface based on ion Coulomb crystals in an opticalcavity*, Ph.D. thesis, Danish National Research Foundation Center for Quantum Optics - Quantop Department of Physics and Astronomy, The University of Aarhus (2010).

[81] J. Dalibard and C. Cohen-Tannoudji, *Dressed-Atom Approach to Atomic Motion in Laser-Light - the Dipole Force Revisited*, Journal of the Optical Society of America B-Optical Physics **2**, 1707 (1985).

[82] S. Haroche and J. M. Raimond, *Exploring the quantum : atoms, cavities, and photons* (Oxford University Press, 2006).

[83] M. O. Scully and M. Zubairy, *Quantum optics* (Cambridge university press, 1997).

[84] V. Vuletić and S. Chu, *Laser Cooling of Atoms, Ions, or Molecules by Coherent Scattering*, Phys. Rev. Lett. **84**, 3787 (2000),
URL link.

[85] H. Ritsch, P. Domokos, F. Brennecke and T. Esslinger, *Cold atoms in cavity-generated dynamical optical potentials*, Rev. Mod. Phys. **85**, 553 (2013),
URL link.

[86] A. Mortensen, *Aspects of Ion Coulomb Crystal based Quantum Memory for Light*, Ph.D. thesis, Danish National Research Foundation Center for Quantum Optics - Quantop Department of Physics and Astronomy, The University of Aarhus (2005).

[87] G. R. Guthohrlein, M. Keller, K. Hayasaka, W. Lange and H. Walther, *A single ion as a nanoscopic probe of an optical field*, Nature **414**, 49 (2001),
URL link.

[88] M. Keller, B. Lange, K. Hayasaka, W. Lange and H. Walther, *Deterministic coupling of single ions to an optical cavity*, Applied Physics B **76**, 125 (2003),
URL link.

[89] A. B. Mundt, A. Kreuter, C. Becher, D. Leibfried, J. Eschner, F. Schmidt-Kaler and R. Blatt, *Coupling a Single Atomic Quantum Bit to a High Finesse Optical Cavity*, Phys. Rev. Lett. **89**, 103001 (2002),
URL link.

[90] A. Stute, B. Casabone, P. Schindler, T. Monz, P. O. Schmidt, B. Brandstatter, T. E. Northup and R. Blatt, *Tunable ion-photon entanglement in an optical cavity*, Nature **485**, 482 (2012),
URL link.

[91] M. Steiner, H. M. Meyer, C. Deutsch, J. Reichel and M. Köhl, *Single Ion Coupled to an Optical Fiber Cavity*, Phys. Rev. Lett. **110**, 043003 (2013),
URL link.

[92] B. Brandstätter, A. McClung, K. SchÃijppert, B. Casabone, K. Friebe, A. Stute, P. O. Schmidt, C. Deutsch, J. Reichel, R. Blatt and T. E. Northup, *Integrated fiber-mirror ion trap for strong ion-cavity coupling*, Review of Scientific Instruments **84**, 123104 (2013),
URL link.

[93] A. Dantan, M. Albert, J. P. Marler, P. F. Herskind and M. Drewsen, *Large ion Coulomb crystals: A near-ideal medium for coupling optical cavity modes to matter*, Physical Review A **80** (2009).

[94] M. Fleischhauer, S. F. Yelin and M. D. Lukin, *How to trap photons? Storing single-photon quantum states in collective atomic excitations*, Optics Communications **179**, 395 (2000).

[95] M. D. Lukin, S. F. Yelin and M. Fleischhauer, *Entanglement of atomic ensembles by trapping correlated photon states*, Physical Review Letters **84**, 4232 (2000).

[96] M. Albert, A. Dantan and M. Drewsen, *Cavity electromagnetically induced transparency and all-optical switching using ion Coulomb crystals*, Nature Photonics **5**, 633 (2011).

[97] K. R. Zangenberg, A. Dantan and M. Drewsen, *Spatial mode effects in a cavity EIT-based quantum memory with ion Coulomb crystals*, Journal of Physics B-Atomic Molecular and Optical Physics **45** (2012).

[98] P. W. Milonni and J. H. Eberly, *Lasers* (Wiley, New York, 1988).

[99] G. D. Boyd and D. A. Kleinman, *Parametric Interaction of Focused Gaussian Light Beams*, Journal of Applied Physics **39**, 3597 (1968).

[100] www.raicol.com
URL link.

[101] A. Arie, G. Rosenman, V. Mahal, A. Skliar, M. Oron, M. Katz and D. Eger, *Green and ultraviolet quasi-phase-matched second harmonic generation in bulk periodically-poled KTiOPO4*, Optics Communications **142**, 265 (1997).

[102] R. Le Targat, J. J. Zondy and P. Lemonde, *75%-efficiency blue generation from an intracavity PPKTP frequency doubler*, Optics Communications **247**, 471 (2005).

[103] F. Torabi-Goudarzi and E. Riis, *Efficient cw high-power frequency doubling in periodically poled KTP*, Optics Communications **227**, 389 (2003).

[104] T. W. Hansch and B. Couillaud, *Laser Frequency Stabilization by Polarization Spectroscopy of a Reflecting Reference Cavity*, Optics Communications **35**, 441 (1980).

[105] H. Kogelnik and T. Li, *Laser Beams and Resonators*, Applied Optics **5**, 1550 (1966).

[106] H. Mabuchi, E. S. Polzik and H. J. Kimble, *Blue-Light-Induced Infrared-Absorption in Knbo3*, Journal of the Optical Society of America B-Optical Physics **11**, 2023 (1994).

[107] T. Tanimura, D. Akamatsu, Y. Yokoi, A. Furusawa and M. Kozuma, *Generation of a squeezed vacuum resonant on a rubidium D-1 line with periodically poled KTiOPO4*, Optics Letters **31**, 2344 (2006).

[108] G. Hetet, O. Glockl, K. A. Pilypas, C. C. Harb, B. C. Buchler, H. A. Bachor and P. K. Lam, *Squeezed light for bandwidth-limited atom optics experiments at the rubidium D1 line*, Journal of Physics B-Atomic Molecular and Optical Physics **40**, 221 (2007).

[109] F. Jensen, *Laser Frequency Stabilization for use in STIRAP Experiments*, Master's thesis, Department of Physics and Astronomy, The University of Aarhus (2004).

[110] R. W. P. Drever, J. L. Hall, F. V. Kowalski, J. Hough, G. M. Ford, A. J. Munley and H. Ward, *Laser Phase and Frequency Stabilization Using an Optical-Resonator*, Applied Physics B-Photophysics and Laser Chemistry **31**, 97 (1983).

[111] E. D. Black, *An introduction to Pound-Drever-Hall laser frequency stabilization*, American Journal of Physics **69**, 79 (2001).

[112] P. F. Herskind, A. Dantan, M. Albert, J. P. Marler and M. Drewsen, *Positioning of the rf potential minimum line of a linear Paul trap with micrometer precision*, Journal of Physics B: Atomic, Molecular and Optical Physics **42**, 154008 (2009), URL link.

[113] P. Herskind, A. Dantan, M. Langkilde-Lauesen, A. Mortensen, J. SÃÿrensen and M. Drewsen, *Loading of large ion Coulomb crystals into a linear Paul trap incorporating an optical cavity*, Applied Physics B **93**, 373 (2008), URL link.

[114] L. Hornekær, N. Kjærgaard, A. M. Thommesen and M. Drewsen, *Structural Properties of Two-Component Coulomb Crystals in Linear Paul Traps*, Phys. Rev. Lett. **86**, 1994 (2001), URL link.

[115] A. Mortensen, E. Nielsen, T. Matthey and M. Drewsen, *Radio frequency field-induced persistent long-range ordered structures in two-species ion Coulomb crystals*, Journal of Physics B: Atomic, Molecular and Optical Physics **40**, F223 (2007), URL link.

[116] N. Kjærgaard, L. Hornekær, A. M. Thommesen, Z. Videsen and M. Drewse, *Isotope selective loading of an ion using resonance-enhanced two-photon ionization*, Applied Physics B: Lasers and Optics **71**, 207 (2000), URL link.

[117] A. Mortensen, J. J. T. Lindballe, I. S. Jensen, P. Staanum, D. Voigt and M. Drewsen, *Isotope shifts of the* $4s^2\ ^1S_0 \rightarrow 4s5p\ ^1P_1$ *transition and hyperfine splitting of the* $4s5p\ ^1P_1$ *state in calcium*, Phys. Rev. A **69**, 042502 (2004), URL link.

[118] T. Hof, D. Fick and H. Jänsch, *Application of diode lasers as a spectroscopic tool at 670 nm*, Optics Communications **124**, 283 (1996), URL link.

[119] A. S. Arnold, J. S. Wilson and M. G. Boshier, *A simple extended-cavity diode laser*, Review of Scientific Instruments **69**, 1236 (1998),
URL link.

[120] L. Ricci, M. Weidemüller, T. Esslinger, A. Hemmerich, C. Zimmermann, V. Vuletic, W. König and T. Hänsch, *A compact grating-stabilized diode laser system for atomic physics*, Optics Communications **117**, 541 (1995),
URL link.

[121] P. G. Hoel, S. C. Port and C. J. Stone, *Introduction to probability theory*, volume 12 (Houghton Mifflin Boston, 1971).

[122] V. S. Letokhov, *Narrowing of the Doppler Width in a Standing Wave*, ZhETF Pisma Redaktsiiu **7**, 348 (1968).

[123] A. Ashkin, *Acceleration and Trapping of Particles by Radiation Pressure*, Phys. Rev. Lett. **24**, 156 (1970),
URL link.

[124] J. E. Bjorkholm, R. R. Freeman, A. Ashkin and D. B. Pearson, *Observation of Focusing of Neutral Atoms by the Dipole Forces of Resonance-Radiation Pressure*, Phys. Rev. Lett. **41**, 1361 (1978),
URL link.

[125] S. Chu, J. E. Bjorkholm, A. Ashkin and A. Cable, *Experimental Observation of Optically Trapped Atoms*, Phys. Rev. Lett. **57**, 314 (1986),
URL link.

[126] C. Adams and E. Riis, *Laser cooling and trapping of neutral atoms*, Progress in Quantum Electronics **21**, 1 (1997),
URL link.

[127] C. E. Wieman, D. E. Pritchard and D. J. Wineland, *Atom cooling, trapping, and quantum manipulation*, Rev. Mod. Phys. **71**, S253 (1999),
URL link.

[128] I. Bloch, J. Dalibard and S. Nascimbene, *Quantum simulations with ultracold quantum gases*, Nat Phys **8**, 267 (2012),
URL link.

[129] C. Zipkes, S. Palzer, L. Ratschbacher, C. Sias and M. Köhl, *Cold Heteronuclear Atom-Ion Collisions*, Phys. Rev. Lett. **105**, 133201 (2010),
URL link.

[130] H. Katori, S. Schlipf and H. Walther, *Anomalous Dynamics of a Single Ion in an Optical Lattice*, Phys. Rev. Lett. **79**, 2221 (1997),
URL link.

[131] C. Schneider, M. Enderlein, T. Huber and T. Schätz, *Optical trapping of an ion*, Nature Photonics **4**, 772 (2010).

[132] M. Enderlein, T. Huber, C. Schneider and T. Schaetz, *Single Ions Trapped in a One-Dimensional Optical Lattice*, Phys. Rev. Lett. **109**, 233004 (2012), URL link.

[133] L. Karpa, A. Bylinskii, D. Gangloff, M. Cetina and V. Vuletić, *Suppression of Ion Transport due to Long-Lived Subwavelength Localization by an Optical Lattice*, Phys. Rev. Lett. **111**, 163002 (2013), URL link.

[134] W. Alt, D. Schrader, S. Kuhr, M. Müller, V. Gomer and D. Meschede, *Single atoms in a standing-wave dipole trap*, Phys. Rev. A **67**, 033403 (2003), URL link.

[135] C. Tuchendler, A. M. Lance, A. Browaeys, Y. R. P. Sortais and P. Grangier, *Energy distribution and cooling of a single atom in an optical tweezer*, Phys. Rev. A **78**, 033425 (2008), URL link.

[136] C. Salomon, J. Dalibard, A. Aspect, H. Metcalf and C. Cohen-Tannoudji, *Channeling atoms in a laser standing wave*, Phys. Rev. Lett. **59**, 1659 (1987), URL link.

[137] J. B. Marion, *Classical dynamics of particles and systems* (Academic Press, 2013).

[138] J. Emsley, *The Elements* (Oxford University Press, New York, 1995).

[139] C. J. Foot, *Atomic physics* (Oxford University Press, 2004).

[140] B. H. Brandsen and C. J. Joachain, *Physics of Atoms and Molecules* (Prentice Hall, 2003), 2nd edition.

[141] P. F. Byrd and M. D. Friedman, *Handbook of elliptic integrals for engineers and scientists*, volume 67 (Springer Science & Business Media, 2012).